CZECH TECHNICAL UNIVERSITY IN PRAGUIE

FACULTY OF MECHANICAL ENGINEERING

Department of Process Engineering

Dissertation

Investigation of Flow and Agitation of non-Newtonian Fluids

Ing. Mehmet Ayas

Supervisor

Prof. Ing. Tomas Jirout Ph.D.

Co-Supervisor

Doc. Ing. Jan Skocilas Ph.D.

Study Program: Mechanical Engineering

Field of Study :Design and Process Engineering

2020 Prague

Type of publication	Ph.D. Dissertation
Title	Investigation of flow and agitation of non-Newtonian fluids
Author	Ing. Mehmet Ayas
Supervisor	Prof. Ing. Tomas Jirout Ph.D. Department of process engineering, Faculty of Mechanical Engineering, Czech Technical University in Prague, Czech Republic
Co-supervisor:	Doc. Ing. Jan Skocilas Ph.D. Department of process engineering, Faculty of Mechanical Engineering, Czech Technical University in Prague, Czech Republic
University	Czech Technical University in Prague
Faculty	Faculty of Mechanical Engineering
Department	Department of Process Engineering
Address	Technická 4, 166 07 Prague 6, Czech Republic
Number of page	140
Number of figures	53
Number of table	7

Declaration

I declared that thesis is entirely my own work and that where material could be construed as the work of others, it is fully cited and referenced, and/or with appropriate acknowledgement given.

…….

Ing. Mehmet Ayas

Prague 2020

Acknowledgment

Foremost, I would like to thank my supervisors, Prof. Ing. Tomas Jirout Ph.D. and Doc. Ing. Jan Skocilas Ph.D. for their great support and my Ph.D. study. Also, I am very glad and thankful to the members of the Process Engineering Department for valuable advice and suggestions.

Thanks to my father Dr. Ali Ayas and mother Elif Ayas for their love and their support for pursuing my study.

And my dear wife Natalia Bezuglova Ayas; I was not able to keep on my Ph.D. study without your great support and love.

Annotation

The present study is aimed to investigate the flow and agitation of purely viscous non-Newtonian fluids in the laminar flow regime. Firstly, rheological parameters of the investigated fluid (bovine collagen) are determined through the rectangular channel and concentric annulus for power-law and Herschel–Bulkley models.

A new method is proposed for the determination of the shear viscosity of the power-law fluids for those geometries. The provided method is then validated by experimental and numerical methods. It is found that the proposed method is successful for the determination of the shear viscosity. Then, the provided method is utilized for the prediction of friction factor of the flow of power-law fluids in non-circular channels using the Reynolds number suggested by Metzner and Reed and a simple method is suggested for the rapid calculation of the friction factor of power-law fluids in laminar regime particularly for the engineering calculations.

Finally, the power and flow characteristics of a newly designed in-line rotor-stator mixer are investigated experimentally and numerically for the Herschel–Bulkley model. The power draw of the mixer is measured experimentally and then obtained power draw values are validated by numerical simulations. The power draw and Metzner-Otto coefficients are determined from the experimentally and numerically obtained power draw results and a new slope method is suggested based on the Rieger-Novak method for mixing of viscoplastic fluids in the laminar regime. The shear and velocity profile in the mixer analyzed via numerical methods and the effect of geometrical configuration on velocity, shear, and power consumption are discussed.

Keywords: Non-Newtonian fluids, power-law model, laminar flow, in-line rotor-stator mixer, numerical computation.

Table of Contents

Introduction

Non-Newtonian fluids such as emulsions, dough, polymer melts, food products, slurries can be encountered in various fields of the industry. The flow behavior of non-Newtonian fluids is considerably complicated than Newtonian fluids since the viscosity of those fluids is not constant and it is the function of the rate of deformation. Due to their high viscosities, the flow of non-Newtonian fluids is in the laminar flow regime mostly, so the flow of those fluids is dominated by viscous forces. Therefore, the design and process parameters of apparatus and systems involving non-Newtonian fluids flow such as friction factor, heat transfer coefficient are related to the rheological model of the processed fluid in the system.

For designing a mixer, the most important design parameter is power consumption. It is required for the selection and designing of various components like gear and electric motor. Especially, in laminar mixing, the power requirement of a mixer is strongly dependent on the viscosity of the processed fluid. Therefore, the rheological parameters of the processed fluid must be known for proper design and a desirable mixing process.

In this work, the power characteristics of a newly designed rotor-stator mixer will be analyzed which has been designed with the aim of mixing the collagen matter and this study requires the knowledge of rheological parameters of the agitated fluid. Hence, firstly rheological properties of the utilized fluid will be analyzed using capillary annulus and rectangular channels which are rarely used geometries for the investigation of the rheological properties of the non-Newtonian fluids. In this section, we will deal with alternative methods for the determination of the shear viscosity and this method will be extended to provide an alternative approach for the prediction of the friction factor of the power-law fluids in non-circular ducts. Then, the power characteristics of a rotor-stator mixer will be investigated based on determined rheological parameters by experimental and numerical methods in order to determine dimensionless parameters such as power draw and Metzner-Otto coefficients. Moreover, velocity and shear profile within the mixing region will be studied from the numerically obtained results for the investigated fluid and the power-law model. The power number and Reynolds number relationship will be considered particularly for viscoplastic fluids and the efficiency of the mixer will be discussed.

Chapter 1 -Literature Survey

1- Basics of non-Newtonian fluids

Rheology is defined as the science of the deformation and flow of materials (Barners et al., 1989). Any material undergoes deformation under the effect of external forces and the relationship between the applied external force and the resulting deformation is unique for each material (Darby, 1976). The knowledge of rheology is essential for engineering applications, especially systems involving polymeric fluids, pastes, and slurries (Vicente, 2012).

In terms of fluids, the applied external force is characterized by stress which can be defined as internal reaction force per unit area, and deformation is specified by strain rate or velocity gradients (Darby R., 1976). The stress and strain rate are second-order tensors that have nine components (Steffe, 1996). The stress tensor ($\vec{\sigma}$) is expressed by index notation as follows.

$$\sigma_{ij} = \begin{bmatrix} \sigma_{11} & \sigma_{12} & \sigma_{13} \\ \sigma_{21} & \sigma_{22} & \sigma_{23} \\ \sigma_{31} & \sigma_{32} & \sigma_{33} \end{bmatrix} \quad (1\text{-}1)$$

Due to symmetry ($\sigma_{ij} = \sigma_{ji}$), there are only six components of the stress tensors that are independent.

Alternatively,

$$\sigma_{ij} = -p\delta_{ij} + \tau_{ij} \quad (1\text{-}2)$$

Stress tensor (Chhabra and Richardson, 2008) is composed of pressure (isotropic component) and shear stress (anisotropic component). In Eq. 1-2 the term δ_{ij} is unit tensor (Kronecker delta) which is defined as

$$\delta_{ij} = \begin{bmatrix} 1 & 0 & 0 \\ 0 & 1 & 0 \\ 0 & 0 & 1 \end{bmatrix} \qquad \text{If} \quad i=j,\ \delta = 1 \qquad i \neq j,\ \delta = 0 \quad (1\text{-}3)$$

Pressure causes a change in volume of fluid and shear stress induces a change in shape (Darby, 1976) so that the sheared flow of fluid is driven by the action of shear stresses. Namely, only shear stresses are the contribution of flow. In the case of incompressible fluids, the trace of the shear stress tensor is (Sestak and Rieger, 2005)

$$\mathrm{tr}(\tau_{ij}) = \tau_{11} + \tau_{22} + \tau_{33} = 0 \quad (1\text{-}4)$$

The strain rate tensor is composed of symmetric and antisymmetric parts, such that

$$\nabla\vec{u} = \frac{1}{2}(\nabla\vec{u} + \nabla\vec{u}^{T}) + \frac{1}{2}(\nabla\vec{u} - \nabla\vec{u}^{T}) = \vec{\vec{\Delta}} + \vec{\vec{\Omega}} \quad (1\text{-}5)$$

On the right-hand side of Eq. 1-5, the first term is the symmetric part of the strain rate tensor, which indicates pure deformation and it is called the rate of deformation tensor ($\vec{\vec{\Delta}}$). The second term states pure rotation, which is termed as vorticity tensor ($\vec{\vec{\Omega}}$). In the case of pure deformation, Eq. 1-5 is given by index notations as follows.

$$\Delta_{ij} = \frac{1}{2}\left(\frac{\partial u_i}{\partial x_j} + \frac{\partial u_j}{\partial x_i}\right) \quad (1\text{-}6)$$

The relationship between τ_{ij} and Δ_{ij} are given by constitutive equations and (Darby, 1976) the fluids can be categorized according to the constitutive equations which are described in the following section.

1-1 Purely viscous fluids

The shear stress is the only function of the rate of deformation tensor at a given temperature and pressure for purely viscous fluids. The relationship between stress and the rate of deformation tensors is given by

$$\tau_{ij} = 2\eta\Delta_{ij} \quad (1\text{-}7)$$

The ratio between shear stress and the rate of deformation is a material property which is called viscosity. Viscosity is a measure of the intensity of energy dissipation which is required to maintain the flow of fluid (Ferguson and Kemblowski, 1991). Purely viscous fluids are also called as time-independent fluids (Chhabra, R.P and Richardson, 2008).

Simple Shear Flow

Constitutive equations and material function of fluid are mostly investigated based on simple shear flow since this type of flow enable one-dimensional flow and only one term of the rate of deformation tensor (hence stress tensor) is non-zero and that provides great convenience for the determination of the material function of the investigated fluid (Darby, 1976; Ferguson and Kemblowski, 1991).

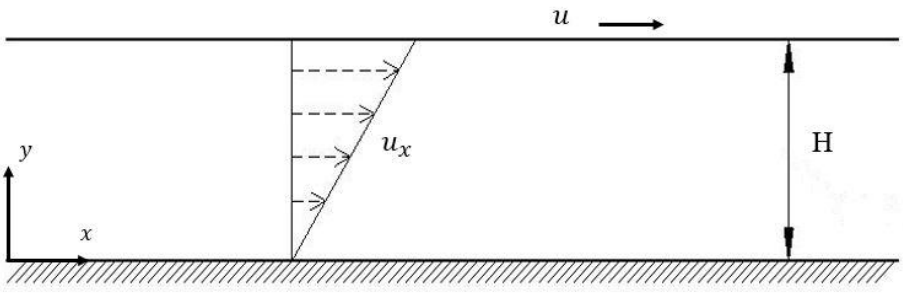

Figure 1-1 Description of simple shear flow

Considering laminar-steady flow between two infinite parallel plates, one is stationary, and the other plate is moving with a constant velocity u at a distance H as shown in figure 1-1. Assuming $u_x = u_x(y)$, $u_y = u_z = 0$, the continuity equation (see appendix A) reduces to

$$\frac{\partial u_x}{\partial x} = 0 \tag{1-8}$$

and the rate of deformation tensor (Appendix. A) is

$$\Delta_{xy} = \Delta_{yx} = \frac{\partial u_x}{\partial y} \tag{1-9}$$

According to the Cauchy equation, the stress tensor for the simple shear flow on the $x - y$ plane is given by

$$\frac{\partial \tau_{xy}}{\partial y} = 0 \tag{1-10}$$

Eq. 1-10 implies that the stress distribution within the flow medium is uniform so, according to Eq. 1-7 the rate of deformation is constant as well. Hence the rate of deformation tensor can be stated as follows

$$\frac{\partial u_x}{\partial y} = C \tag{1-11}$$

From Eq. 1-9 and Eq. 1-11, it can be seen that the rate of deformation is constant and independent of geometry. Solving Eq. 1-11 for the given boundary conditions, the velocity profile is given as follows

$$u_x = \frac{u}{H} y \tag{1-12}$$

Eq. 1-12 indicates that the velocity profile varies linearly on the y-direction and is independent of the rheological model. In the following section, the description of the rheological models will be explained based on the simple shear model.

1-2 Newtonian fluids

Newtonian fluids indicate a constant ratio between shear stress and rate of deformation tensors i.e. viscosity has a constant value at a given temperature and pressure. In nature, most of the fluids exhibit Newtonian behavior. Especially all gases and liquids with a simple molecular structure show Newtonian characteristics. The shear stress-rate of deformation relationship is given by

$$\tau_{ij} = 2\mu\Delta_{ij} \tag{1-13}$$

Equation 1-13 is known as Newton's law of viscosity (Ferguson and Kemblowski, 1991). In Eq. 1-13, μ is Newtonian viscosity which depends on the structure of fluid, pressure, and temperature. In general, temperature has a strong effect on the viscosity of liquids and gases. The viscosity of Newtonian fluids decreases with increasing temperature and the relationship between temperature and viscosity according to Arrhenius's expressed by (Mezger, 2014)

$$\mu = Ae^{B/T} \tag{1-14}$$

Where μ is the viscosity of a Newtonian fluid, T is the temperature (K) and A, B are constants of fluids. In terms of gases, the viscosity increases with increasing temperature. According to the power-law (White, 1999)

$$\mu = \mu'(\frac{T}{T_0})^y \tag{1-15}$$

where μ' is the viscosity at absolute temperature, T_0 (273 K) and y is the exponent which varies as regards the type of gas.

1-3 Purely viscous non-Newtonian fluids

There are some certain fluids such as pastes, slurries, and polymeric fluids, the relationship between shear stress and shear rate for those fluids cannot be expressed with respect to Eq. 1-13, and such fluids are known as non-Newtonian fluids (Ferguson and Kemblowski, 1991). For incompressible, purely viscous fluids, the viscosity is not a constant parameter and varies with respect to the rate of deformation at a given temperature and pressure. Hence the shear stress and rate of deformation relationship of non-Newtonian fluids can be expressed using the analogy of Newton's law of such that

$$\tau_{ij} = 2\eta(\Delta_{ij})\Delta_{ij} \tag{1-16}$$

Where $\eta(\Delta_{ij})$ is the material function called apparent viscosity, which is the function of three scalar invariants of the rate of deformation tensor (Sestak and Rieger, 2005), hence

$$\eta(\Delta_{ij}) = \eta(I, II, III) \tag{1-17}$$

The first invariant (I) is the trace of the rate of deformation tensor (the sum of diagonal components) which is zero for incompressible fluids. The third invariant (III) is determinant of the rate of deformation tensor which is also zero. Hence, only the second invariant (II) is non-zero which is equal to double scalar products of the rate of deformation tensors (Osswald and Rudolph, 2015).

$$II = \vec{\vec{\Delta}} : \vec{\vec{\Delta}} \tag{1-18}$$

As a result, the stress-rate of deformation relationship for non-Newtonian fluids is given by

$$\tau_{ij} = 2\eta(II)\Delta_{ij} \tag{1-19}$$

In the case of simple shear flow, the shear rate can be described as,

$$\dot{\gamma} = \left|\sqrt{2II}\right| = \sqrt{2\Delta_{ij}\Delta_{ji}} \tag{1-20}$$

Where $\dot{\gamma}$ is the shear rate, which is the magnitude of the rate of deformation tensor (Morrinson, 2001). Purely viscous non-Newtonian fluids can be classified based on the relationship between shear rate and shear stress or the existence of yield stress (Chhabra and Richardson, 2008). which is demonstrated in figure 1-2.

-shear-thinning fluids (pseudoplastic)

-shear thickening fluids (Dilatant)

-Viscoplastic fluids

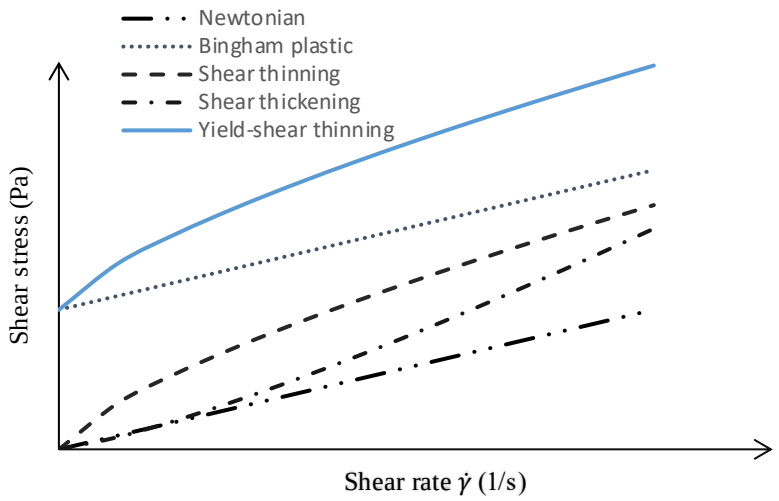

Figure 1-1-2 Flow curves of purely viscous fluids (Ferguson and Kemblowski, 1991)

a- Shear-thinning fluids:

Shear-thinning fluids are the most encountered type of non-Newtonian fluids (Chhabra and Richardson, 2008). The apparent viscosity of the shear-thinning fluids decreases with increasing shear rate and the flow curve passes through the origin (Ferguson and Kemblowski, 1991). Indeed, at low and high shear rates, shear-thinning fluids show Newtonian characteristics i.e. constant viscosity. At low shear rates, apparent viscosity is considered as zero shear viscosity (μ_0) and at a very high shear rate is considered as infinite shear viscosity (μ_∞) given in figure 1-3. At the intermediate shear rates, viscosity exhibits shear-dependent characteristics (Osswald and Rudolph, 2015).

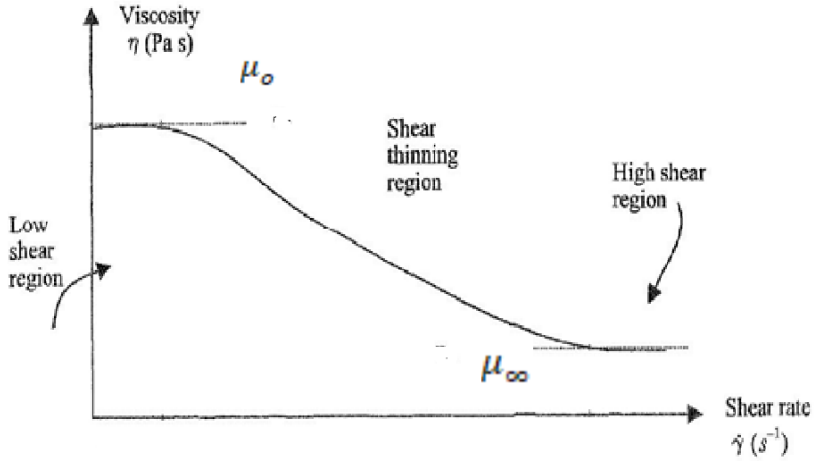

Figure 1-1-3 Viscosity versus shear rate relation of shear-thinning behavior (Nassehi, 2002)

b- Shear thickening fluids (Dilatant)

The apparent viscosity of dilatant fluids increases with increasing shear rate and the flow curve passes through origin the same as shear thinning and Newtonian fluids. (Ferguson and Kemblowski, 1991). Concentrated suspensions exhibit shear thickening behavior but it is rarely encountered non-Newtonian behavior.

c- Viscoplastic fluids

Viscoplastic fluids possess yield stress and such fluids flow when the material is subjected to shear stresses greater than the yield stress (Chhabra and Richardson, 2008). When applied shear stresses smaller than the yield stress, such materials show solid characteristics and deform elastically. The flow curve does not pass through the origin. Some viscoplastic fluids can be characterized by a linear flow curve which is known as Bingham fluid and the viscosity of Bingham fluids is called plastic viscosity. On the other hand, some viscoplastic fluids exhibit shear-thinning characteristics when applied shear stress is greater than yield stress and those fluids are called yield shear-thinning fluids.

1-4 Empirical models for purely viscous non-Newtonian fluids

Power-law model (Oswald-de Waele)

The power-law model is the simplest and most frequently used two parameters empirical model (Delplace and Leuliet, 1995) to describe the relationship between shear rate and shear stress of shear-thinning and dilatant fluids. The model is given by

$$\eta = K(\left|\sqrt{2II}\right|)^{n-1} \tag{1-21}$$

Where K is consistency, and n is the flow index. For $0 < n < 1$ indicates shear thinning behavior and $n > 1$ shows shear thickening behavior. For $n = 1$, the model reduces to the Newtonian fluid. However, it should be noted that the power-law model is unable to predict zero and infinite shear viscosities. Hence the model is successful only in a certain range of shear rates.

Ellis model

Ellis model is a three parameters model and is suitable at low shear rates since the model involves zero shear viscosity. Ellis model is given as follows

$$\eta = \left(\frac{\mu_o}{1 + \left[\tau/\tau_{1/2}\right]^{\alpha-1}}\right) \tag{1-22}$$

Where $\tau_{1/2}$ indicates the value of shear stress at which $\eta = 0.5\ \mu_o$ (Darby R., 1976). At very low shear rates (i.e. τ approaches to zero) the model reduces to the Newtonian fluid.

Cross model

The Cross model is a four-parameter model that involves zero and infinite shear viscosities and enables the prediction of shear rate-shear stress relationship over a wide range of shear rates. The cross model is

$$\frac{\eta - \mu_\infty}{\mu_o - \mu_\infty} = \frac{1}{1 + (\theta|\sqrt{2II}|)^p} \quad (1\text{-}23)$$

Where θ is time constant and has the unit of second.

Carreu model

The Carreu model is another four-parameter model same as the Cross model which can be used also describe non-Newtonian characteristics over a wide range of shear rates.

$$\frac{\eta - \mu_\infty}{\mu_o - \mu_\infty} = (1 + (\theta|\sqrt{2II}|)^2)^{(n-1)/2} \quad (1\text{-}24)$$

Bingham model

Bingham model is the simplest model in order to characterize viscoplastic fluids having constant viscosity (Bingham fluids). The model has two parameters

$$\eta = \tau_o/(|\sqrt{2II}|) + \mu_p \quad \text{for} \quad \tau > \tau_o \quad (1\text{-}25)$$

$$\dot{\gamma} = 0 \quad \tau < \tau_o \quad (1\text{-}26)$$

Where τ_o is yield stress and μ_p is plastic viscosity which is independent of shear rate.

Besides, fine-grained, highly concentrated suspensions exhibit viscoplastic characteristics and usually, the Bingham model is used to describe rheological behavior of such fluids in a certain range of the shear rate and a wide range of shear rate, two equations of Bingham model (at low and high shear rate ranges) are required. Rieger and Moravec (Moravec et al., 2009) suggested a model for describing the rheological model of such fluids within the wide range of shear rate only by one equation which is given as follows

$$\tau = \frac{\tau_{01} + \mu_{p1}\left|\sqrt{2II}\right|}{\left[1 + \left(\frac{\tau_{01} + \mu_{p1}\left|\sqrt{2II}\right|}{\tau_{02} + \mu_{p2}\left|\sqrt{2II}\right|}\right)^{b}\right]^{1/b}} \quad (1\text{-}27)$$

In Eq. 1-27, index 1 corresponds to rheological parameters of low shear rate and 2 high values of shear rate. The parameter b indicates the transition range.

Herschel-Bulkley model

The model is frequently used to describe yield shear-thinning (pseudoplastic) fluids and has 3 parameters.

$$\eta = \tau_o/\left|\sqrt{2II}\right| + K\left(\left|\sqrt{2II}\right|\right)^{n-1} \quad \text{for} \quad \tau > \tau_o \quad (1\text{-}28)$$

$$\dot{\gamma} = 0 \quad \tau < \tau_o \quad (1\text{-}29)$$

K and n are parameters of the power-law model and τ_o is yield stress.

Casson model

Another two parameters viscoplastic model exhibits shear-thinning characteristics and mainly used modeling for blood and bio-fluids which is given as follows

$$\sqrt{\tau} = \sqrt{\tau_o} + \sqrt{m\left|\sqrt{2II}\right|} \quad \text{for} \quad \tau > \tau_o \quad (1\text{-}30)$$

1-5 Thixotropy

The apparent viscosity of certain fluids is the function of shear rate and the processing time of shear and those fluids are called time-dependent fluids (Chhabra and Richardson, 2008). Thixotropic fluids exhibit a reversible decrease in apparent viscosity in time at a constant shear rate which is resulting from the structure of thixotropic fluids. The structure of thixotropic fluids is breaking down due to shear stress and building up at the rest (Steffe, 1996). Those breaking down and building down processes are reversible and occur isothermal (Ferguson and Kemblowski, 1991). Contrarily, rheopexy (negative thixotropy) indicates a reversible increment in apparent viscosity in time at a constant shear rate and the process is reversible-isothermal same as thixotropic fluids.

1-6 Viscoelastic fluids

Numerous non-Newtonian fluids exhibit both viscous and elastic characteristics which are known as viscoelastic fluids. As indicated previously, in purely viscous fluids, created shear stress is the only function of the instantaneous shear rate and normal stress differences are zero. There are such fluids that show memory effect and elasticity, namely rheological characteristics of the fluid strongly affected by

the history of the flow, and those fluids are known as viscoelastic fluids. Moreover, viscoelastic fluids show some remarkable phenomena such as the Weissenberg effect, jet swell, reverse circulation which can be explained by the existence of non-zero normal shear stress differences such that (Darby, 1976)

$$N_1 = \tau_{xx} - \tau_{yy} \tag{1-31}$$

$$N_2 = \tau_{yy} - \tau_{zz} \tag{1-32}$$

Where N_1 and N_2 are first and second normal stress differences which are the quadratic function of shear rate. Hence, the relationship between normal stress difference and shear rate can be expressed as (Ferguson and Kemblowski, 1991)

$$\psi_1 = \frac{N_1}{(|\sqrt{2II}|)^2} \tag{1-33}$$

$$\psi_2 = \frac{N_2}{(|\sqrt{2II}|)^2} \tag{1-34}$$

Where ψ_1 and ψ_2 are normal stress coefficients. It should be noted that the normal stress difference occurs only in fluids that exhibit viscoelasticity. For highly elastic fluids the first normal stress difference may become even larger than the shear stress.

The simplest model of a viscoelastic fluid is described by the Maxwell model (Barners et al., 1989) which is composed of a spring and a dashpot. Spring denotes purely elastic solid and dashpot indicates purely viscous fluid.

The Maxwell model is given by

$$\vec{\vec{\tau}} + \lambda \frac{\partial \vec{\vec{\tau}}}{\partial t} = 2\mu \vec{\vec{\Delta}} \tag{1-35}$$

where λ is relaxation time and it is a material property which is given by

$$\lambda = \frac{\mu}{G} \tag{1-36}$$

Alternatively, Eq. 1-35 can be described by apparent viscosity η and upper convective time derivative (Oldroyd co-deformation tensor) instead of the partial time derivative of stress as follows

$$\vec{\vec{\tau}} + \frac{\eta}{G}\frac{\delta\vec{\vec{\tau}}}{\delta t} = 2\eta\vec{\vec{\Delta}} \tag{1-37}$$

The upper convective term derivation in terms of index notation

$$\frac{\delta\tau_{ij}}{\delta t} = \frac{\partial\tau_{ij}}{\partial t} + u_k\frac{\partial\tau_{ij}}{\partial x_k} - \frac{\partial u_i}{\partial x_k}\tau_{kj} - \frac{\partial u_j}{\partial x_k}\tau_{ik} \tag{1-38}$$

The viscoelasticity of a fluid can be indicated by the ratio of the characteristic material relaxation time to the characteristic time of observation. This ratio is known as the Deborah number (De)

$$De = \frac{\lambda}{t_e} \tag{1-39}$$

where t_e is the characteristic time of deformation. The value of $De \cong 1$ stands for viscoelastic behavior. If De is much smaller than one, the fluid exhibits viscous character and if De is greater than one represents elastic (solid-like) behavior. The degree of elasticity of a fluid can be determined by the ratio of N_1 to τ. If the ratio of first normal stress to shear stress exceeds 1 the fluid is regarded as highly elastic (Darby, 1976).

2- Rheometers and flow in channels

Rheometry is the subdivision of rheology which deals with rheological measurements. The rheometer is a device that is used to determine the material function of the sample (Morrinson, 2001; Malkin and Isayev, 2017). Rheometers can be categorized as drag flow rheometers and pressure-driven rheometers (Macosko, 1994). In drag flow rheometers, the shear is created by drag flow (Couette flow) i.e. generating flow between the moving and fixed planes. The shear rate-stress relationship is determined from the measurement of rotational speed and corresponding torque of the rotating plane (Ferguson and Kemblowski, 1991). In terms of pressure-driven rheometers, shear is generated by pressure gradients (Poiseuille flow), and the shear rate-stress relationship is obtained from the measurement of mean velocity (flow rate) of the sample and corresponding pressure drop values within the fully developed region of the closed channel.

In this section, we will mention about most frequently used rheometers and basic equations related to flow in channels in the laminar flow case.

2-1 Drag flow rheometers

Various drag flow rheometers are available in practice using different geometrical configurations such as concentric cylinders, parallel disks, cone, and plate, sliding plates, and falling ball which can measure various material functions (Macosko, 1994). There are two methods to create shear in drag flow rheometers which are controlled shear and controlled stress. In controlled shear, the shear rate is applied, and the resulting stress is measured. In controlled stress, shear stress is imposed, and the resulting shear rate is measured (Schramm 1998). In this section, we will mention the most frequently used three rheometers briefly.

Rotational co-axial cylinder rheometer (Couette rheometer)

The rotational co-axial cylinder rheometer (Couette rheometer) is a commonly utilized apparatus for determining the shear viscosity of the fluids which is suitable for the measurement of fluids at average shear rates (Steffe, 1996). The Couette rheometer consists of two concentric cylinders, and the gap between cylinders is filled with test fluid. While one is kept stationary, another cylinder is rotating on the z-axis (Morry, 2011) shown in figures 1-4 below.

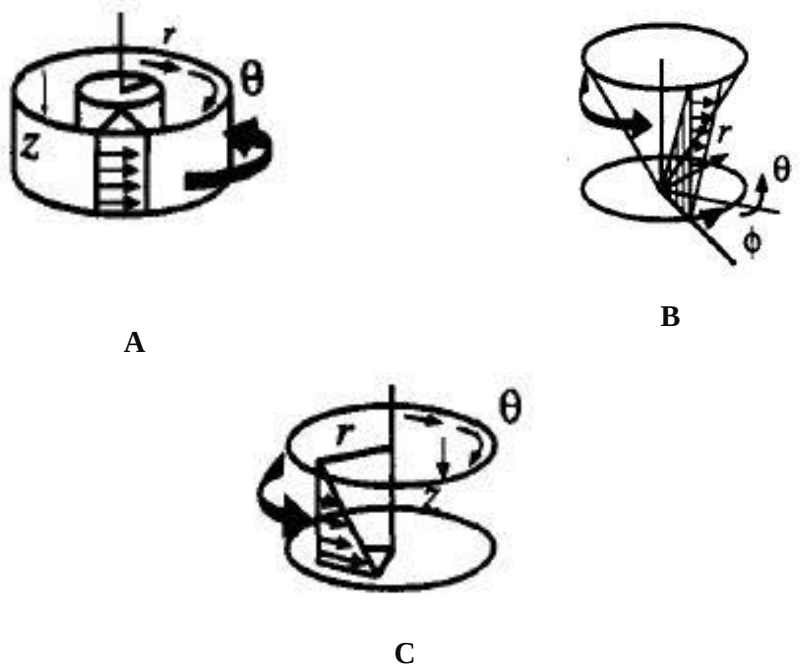

Figure 1-4 Description of drag flow rheometers A- Rotational co-axial cylinder rheometer, B- Cone, and plate rheometer, C- Parallel Disk rheometers (Macosko, 1994)

The flow of fluid within the Couette rheometer is assumed as one dimensional i.e. in cylindrical coordinates, velocity in θ direction, varies only in r direction ($u_\theta(r) \neq 0, u_r = u_z = 0$), and flow is

assumed in the laminar flow regime. Moreover, the effect of edges at the top and bottom of the rheometer is neglected. This can be achieved in practice using adequately long cylinders and keeping a small clearance between the cylinders (Morry, 2011). The determination of wall shear stress is independent of rheological models of the fluid. Shear stress is the only function of measured torque and geometry of the rheometer.

If it is assumed that the inner cylinder is rotating with a speed of ω, the shear stress on the inner cylinder (τ_i) is (Macosko, 1994)

$$\tau_i = \frac{T_i}{2\pi {R_i}^2 L} \tag{1-40}$$

where T_i is the torque generated by the inner cylinder, L is the length and R_i is the radius of the inner cylinder. In the case of Newtonian fluids, the shear rate is

$$\dot{\gamma} = \frac{2\omega}{(1-\kappa^2)}\left(\frac{R_i}{r}\right)^2 \tag{1-41}$$

Where κ is the ratio of the inner radius to the outer radius (R_i/R_o) and shear rate on the inner radius is

$$\dot{\gamma}_i = \frac{2\omega}{(1-\kappa^2)} \tag{1-42}$$

And using Eq.1-40 and Eq.1-42, using stress-strain relationship, in terms of rotational speed and measured torque can be expressed as follows

$$T_i = \frac{4\pi\mu L\omega {R_i}^2}{(1-\kappa^2)} \tag{1-43}$$

The shear rate for the power-law fluids is given by (Rieger, 2006; Macosko, 1994)

$$\dot{\gamma} = \frac{2\omega}{n(1-\kappa^{2/n})}\left(\frac{R_i}{r}\right)^{2/n} \tag{1-44}$$

and shear rate on the inner radius

$$\dot{\gamma}_i = \frac{2\omega}{n(1-\kappa^{2/n})} \tag{1-45}$$

The shear rate measurement of the power-law fluids by the Couette rheometer is performed based on the Newtonian shear rate. The stress-strain relationship of the power law-fluids can be stated concerning Newtonian shear rate such that (Rieger 2006)

$$\tau_i = K\left(\frac{\dot{\gamma}_i}{\dot{\gamma}_{iN}}\right)^n \dot{\gamma}_{iN}{}^n = K\left(\frac{1-\kappa^2}{1-\kappa^{\frac{2}{n}}}\right)^n \dot{\gamma}_{iN}{}^n \quad (1\text{-}46)$$

Where $\dot{\gamma}_{iN}$ is the Newtonian shear rate for the inner radius given in Eq. 1-42. and flow index n is (Macosko, 1994)

$$n = \frac{d\ln(T_i)}{d\ln(\omega)} \quad (1\text{-}47)$$

In general, a decrease in $R_o - R_i$ (a gap between the cylinders) enhance the accuracy of the measurement since higher values of κ enable to obtain uniform shear rate-shear stress profile within the shearing zone (Barners et al., 1989). Therefore, the co-axial cylinder rheometers with a κ greater than 0.9 are used in practical applications (Macosko, 1994). For very narrow gaps between the cylinders ($\kappa > 0.99$), shear rate and shear stress are determined as follows,

$$\tau_M = \frac{T_i}{2\pi R_M{}^2 L} \quad (1\text{-}48)$$

where R_m is the mean of the radius $((R_i + R_o)/2)$ and shear rate is,

$$\dot{\gamma}_M = \frac{\omega R_m}{(R_o - R_i)} \quad (1\text{-}49)$$

There is some source of errors that can be encountered during the rheological measurements such as edge effects, viscous heating, and secondary flow (Darby, 1976), and those can mislead determination of rheological properties. In this study, the source of errors for rotational rheometers are not given however, detailed information can be found in the following books (Macosko 1994; Ferguson and Kemblowski 1991)

Parallel disk rheometers

A parallel disk rheometer consists of a rotational disk and a cylindrical cavity. The shear is generated by the rotation of the disk on the z-axis. The gap (H) between the disk and bottom plane is adjustable depending on the test fluid. For instance, the higher value of H is preferred in the case of measuring suspensions of coarse particles, whereas a narrow gap is desired for the measurement of homogeneous fluids (Macosko 1994; Ferguson and Kemblowski, 1991).

In cylindrical coordinates, velocity exist only in the θ direction ($u_r = u_z = 0$) and u_θ varies both in r and z directions. The non-homogeneous shear profile is created in the sheared zone and the shear rate

profile varies on the r axis. In the case of Newtonian fluids, the shear rate at the perimeter is given by (Steffe 1996; Macosko 1994)

$$\dot{\gamma} = \frac{\omega R}{H} \tag{1-50}$$

and shear stress is

$$\tau = \frac{2T}{\pi R^3} \tag{1-51}$$

In the case of power-law fluids, shear stress is

$$\tau = \frac{T}{2\pi R^3}\left(3 + \frac{d\ln T}{d\ln \dot{\gamma}}\right) \tag{1-52}$$

and flow index (n) is,

$$n = \frac{d\ln T}{d\ln \dot{\gamma}} \tag{1-53}$$

For the Newtonian flow case, Eq. 1-52 reduces to Eq. 1-51. It should be noted that parallel disk rheometers are desirable for the measurement of rheological properties in oscillatory flow (Ferguson and Kemblowski 1991).

Cone and plate rheometers

A cone and plate rheometer is composed of a plate and inverted cone with an angle (θ) and the apex of the cone is located at the center of the plane. In spherical coordinates, the velocity is in φ direction and changes in r and θ directions in spherical coordinate systems. Cone and plate configuration ensure homogeneous shear rate profile within the sheared region, namely shear rate is independent of directions (Macosko 1994)

The shear rate of the rheometer is determined by (Steffe 1996)

$$\dot{\gamma} = \frac{\omega}{R} \tag{1-54}$$

and shear stress is

$$\tau = \frac{3T}{2\pi R^3} \tag{1-55}$$

Due to providing a homogeneous shear rate profile and direct measurement of the first normal stress, cone and plate configuration is desirable for the measurement of the wide range of fluids, particularly for non-Newtonian fluids. A small amount of sample is required for the measurements. Also, a lower value

of θ is preferred ($\theta < 4°$), to avoid secondary flow arising from centrifugal forces (Ferguson and Kemblowski 1991, Darby R., 1976).

2-2 Pressure Driven rheometers and flow in a circular channel

Capillary rheometer

The capillary rheometer is the oldest and the most frequently utilized instrument for the measurement of viscosity due to its simple design and its high accuracy in measurements (Macosko 1994, Chhabra and Richardson, 2008). The capillary rheometer is a straight circular channel which is shown in figure 1-5 and the determination of viscosity is based upon the measurement of pressure drop and volume flow rate along the axial direction within the fully developed region in the channel (Ferguson and Kemblowski, 1991, Malkin and Isayev 2017).

The capillary rheometers can be classified as speed controlled and pressure controlled. In speed-controlled capillary rheometers, the flow rate is applied, and pressure is measured. In pressure controlled capillary rheometer, the pressure is imposed, and the shear rate is measured (Syrjala and Aho 2012).

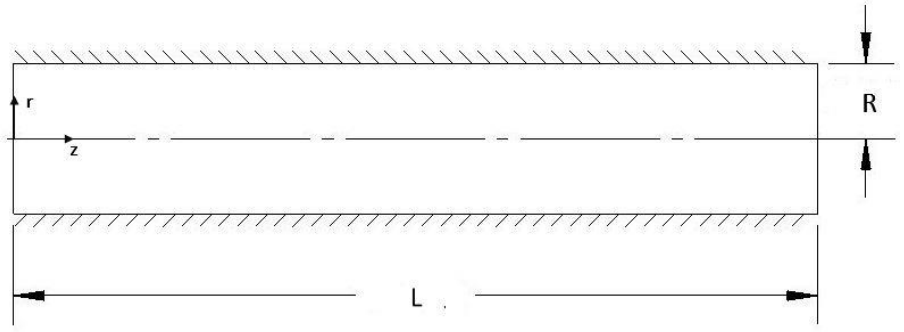

Figure 1-5 Geometrical description of the circular pipe

The flow field in the tube can be described by the continuity and Cauchy equation for purely viscous fluids. Assuming that a fully developed, laminar, incompressible, steady flow of fluid through a tube of length L and radius R under the laminar flow condition for $u_z = u_z(r)$, $u_r = u_\theta = 0$ in the cylindrical coordinate system, the continuity equation (See appendix-A) reduces to

$$\frac{\partial(u_z)}{\partial z} = 0 \qquad (1\text{-}56)$$

and the Cauchy equation (Appendix A) based on the same assumption can be expressed as follows

$$\frac{\partial p}{\partial z} = \frac{1}{r}\frac{\partial (r\tau_{rz})}{\partial r} \tag{1-57}$$

The left-hand side of the Eq. 1-57 is the function of z and the right-hand side varies with respect to r only. That is possible if Eq. 1-57 is equal to a constant. Hence, the left-hand side of the equation (pressure gradient) can be described as

$$\frac{\partial p}{\partial z} = \frac{\Delta p}{L} = \text{constant} \tag{1-58}$$

The Eq. 1-58 indicates that the pressure gradient in a fully developed region of the flow should be constant. Substituting Eq. 1-58 into Eq. 1-57 and taking derivative with respect to r

$$\tau_{rz} = \frac{\Delta p}{L}\frac{r}{2} + \frac{C_1}{r} \tag{1-59}$$

For the values of integration constant different than zero $(C_1 \neq 0)$, τ_{rz} has an infinite value at $r = 0$, thus C_1 must equal to zero. Hence, τ_{rz} is

$$\tau_{rz} = \tau_{zr} = \frac{\Delta p}{L}\frac{r}{2} \tag{1-60}$$

The Eq. 1-60 is independent of the rheological properties of fluid within the fully developed region of the flow and valid for all rheological models.

For the $r - z$ plane, the rate of strain tensor (See Appendix A) system for $u_z = u_z(r)$, $u_r = u_\theta = 0$ is

$$\Delta_{rz} = \Delta_{zr} = \frac{1}{2}\left(\frac{\partial u_z}{\partial r}\right) \tag{1-61}$$

Substituting, Eq. 1-60 and Eq. 1-61 into Eq.1-13, and integrating with respect to r for $u_z = 0$ at $r = R$, the expression of the velocity, u_z is for the Newtonian flow case is given by

$$u_z = \frac{(-\Delta p)R^2}{4\mu L}\left(1 - \frac{r^2}{R^2}\right) \tag{1-62}$$

The volume flow rate concerning the velocity field in a circular channel is given by

$$\dot{V} = \int_0^R 2\pi u_z(r) r dr \tag{1-63}$$

Substituting, Eq. 1-62 into Eq. 1-63

$$\dot{V} = \int_0^R 2\pi \frac{(-\Delta p)R^2}{4\mu L}\left(1 - \frac{r^2}{R^2}\right)dr \tag{1-64}$$

Integrating Eq. 1-64 with respect to r, the volume flow rate is found as

$$\dot{V} = \frac{(-\Delta p)\pi D^4}{128\mu L} \tag{1-65}$$

and mean velocity $\bar{u}$ is

$$\bar{u} = \frac{\dot{V}}{S} = \frac{(-\Delta p)D^2}{32\mu L} \tag{1-66}$$

From Eq. 1-66, Eq. 1-62 can be written in terms of mean velocity is

$$u_z = 2\bar{u}\left(1 - \frac{r^2}{R^2}\right) \tag{1-67}$$

Taking the derivative of Eq. 1-67 with respect to r, the shear rate in terms of mean velocity is

$$\dot{\gamma} = \left(-\frac{du_z}{dr}\right) = \frac{4\bar{u}r}{R^2} \tag{1-68}$$

Eq. 1-68 indicates the relationship between the shear rate and mean velocity, and it is obvious from Eq. 1-60 and Eq. 1-68 that shear rate and shear stress are non-homogeneous i.e. varies with position. Therefore, it is convenient to determine shear stress and shear rate for the wall (Ferguson and Kemblowski, 1991). Hence, the shear stress at the wall for $r = R$ (from Eq. 1-60) is

$$\tau_w = \frac{(-\Delta p)}{L}\frac{R}{2} = \frac{(-\Delta p)}{L}\frac{D}{4} \tag{1-69}$$

and the shear rate at the wall in case of Newtonian fluids is

$$\dot{\gamma}_{Nw} = \frac{8\bar{u}}{D} = \frac{4\dot{V}}{\pi R^3} \tag{1-70}$$

Consequently, for Newtonian fluids, the viscosity can be found from the Eq. 1-69 and Eq. 1-70 as follows

$$\mu = \frac{\tau_w}{\dot{\gamma}_{Nw}} \tag{1-71}$$

For the purely viscous non-Newtonian fluids, the Rabinowitsch-Mooney equation is a very convenient and simple method in order to find out a relationship between pressure drop and flow rate (mean velocity) regardless of the rheological model of the fluid.

The volume flow rate in a tube is given in Eq. 1-63 above and integrating Eq. 1-63 by parts,

$$\dot{V} = 2\pi\left\{\left[\frac{r^2}{2}u_z\right]_0^R + \int_0^R \frac{r^2}{2}\left(-\frac{du_z}{dr}\right)dr\right\} \tag{1-72}$$

On the right-hand side of Eq. 1-72, the first term is zero for $r = 0$ and $r = R$ (no-slip condition), hence Eq. 1-72 can reduce to

$$\dot{V} = 2\pi\left\{\int_0^R \frac{r^2}{2}\left(-\frac{du_z}{dr}\right)dr\right\} \tag{1-73}$$

The ratio of Eq. 1-60 to Eq. 1-69 is

$$\frac{\tau_{rz}}{\tau_w} = \frac{r}{R} \tag{1-74}$$

Taking the derivative of Eq. 1-74 and substituting to Eq. 1-73

$$\frac{\dot{V}{\tau_w}^3}{\pi R^3} = \int_0^{\tau_w} {\tau_{rz}}^2\left(-\frac{du_z}{dr}\right)d\tau_{rz} \tag{1-75}$$

Eq. 1-75 is a suitable tool to describe the relationship between wall shear rate and wall shear stress for rheological models of purely viscous fluids. In the case of the flow of a power-law fluid in a circular channel, substituting Eq. 1-21 together with Eq. 1-61 into Eq. 1-75 and solving for τ_w, following expression is obtained

$$\frac{\dot{V}{\tau_w}^3}{\pi R^3} = \frac{n{\tau_w}^{\frac{3n+1}{n}}}{3n+1}\left(\frac{1}{K}\right)^{1/n} \tag{1-76}$$

After rearranging, the following correlation is obtained,

$$\frac{4\dot{V}}{\pi R^3} = \frac{4n}{3n+1}\left(\frac{\tau_w}{K}\right)^{1/n} \tag{1-77}$$

Consequently, the volume flow rate through the circular channel is

$$\dot{V} = \frac{n\pi R^3}{3n+1}\left(\frac{(-\Delta P)R}{2KL}\right)^{1/n} \tag{1-78}$$

The left-hand side of the Eq. 1-77 is the wall shear rate for the Newtonian flow case ($\dot{\gamma}_{Nw}$) given in Eq. 1-70 and τ_w is the wall shear stress described in Eq. 1-69. For the power-law fluids, the determination of K and n values requires representing the relationship between wall shear rate-wall shear stress as such

in the Newtonian flow case. So, the expression of wall shear rate ($\dot{\gamma}_w$) can be obtained using $\dot{\gamma}_{Nw}$ as follows.

Eq. 1-77 can be written in terms of τ_w and $\dot{\gamma}_{Nw}$ as follows

$$\tau_w = K'(\dot{\gamma}_{Nw})^n \tag{1-79}$$

Where K' is

$$K' = K\left(\frac{3n+1}{4n}\right)^n \tag{1-80}$$

Taking the logarithm of Eq. 1-79,

$$\ln(\tau_w) = \ln(K') + n\ln(\dot{\gamma}_{Nw}) \tag{1-81}$$

From the derivative of Eq. 1-81, the flow index n can be found as

$$n = \frac{d\ln(\tau_w)}{d\ln(\dot{\gamma}_{Nw})} \tag{1-82}$$

The wall shear rate is in terms of $\dot{\gamma}_{Nw}$ is

$$\dot{\gamma}_w = \left(\frac{3n+1}{4n}\right)\dot{\gamma}_{Nw} \tag{1-83}$$

and wall shear stress-wall shear rate relation is

$$\tau_w = K\dot{\gamma}_w{}^n = K\left[\left(0.75 + \frac{0.25}{n}\right)\dot{\gamma}_{Nw}\right]^n \tag{1-84}$$

and if this procedure repeated for the Herschel- Bulkley model by integrating Eq. 1-75 from τ_0 to τ_w, the volume flow rate is given by

$$\dot{V} = n\pi R^3\left(\frac{(-\Delta P)R}{2KL}\right)^{1/n}\left(1-\frac{\tau_0}{\tau_w}\right)^{\frac{1}{n}}\left[\frac{\left(1-\frac{\tau_0}{\tau_w}\right)^3}{3n+1} + \frac{\left(1-\frac{\tau_0}{\tau_w}\right)\left(\frac{\tau_0}{\tau_w}\right)^2}{n+1} + \frac{2\left(1-\frac{\tau_0}{\tau_w}\right)^2\left(\frac{\tau_0}{\tau_w}\right)}{2n+1}\right] \tag{1-85}$$

In conclusion, the viscosity of Newtonian fluids can be determined from the measured volume flow rate and corresponding pressure drop within the fully developed flow region of the channel. The measured flow rate is converted to a wall shear rate using Eq. 1-70 and wall shear stress is determined from the measured pressure drop using the Eq. 1-69. The ratio of wall shear stress to wall shear rate gives us the viscosity of investigated fluids.

Determination of shear viscosity of power-law fluids requires the measurement of volume flow rate and corresponding pressure drop values which must be taken for different values of the volume flow rate. The methodology of determination of K and n parameters can be described briefly as follows. Firstly, from the several measurements of volume flow rate Newtonian wall shear rate is determined using Eq. 1-70 and from the corresponding pressure drop, wall shear stress is calculated by Eq. 1-69. Then, the flow index is determined according to Eq. 1-82 and finally using Eq. 1-84 consistency K is determined.

The source of errors

During the measurement of viscosity, some measurement errors can be encountered. The most frequently faced errors and the way of correction methods are given as follows.

a- End effect

It was stated in the previous section that viscosity calculation in the capillary rheometer relies on the measurement of volume flow rate and corresponding pressure gradient within the fully developed region of the capillary. However, in practice at the entrance and exit regions of the tube, the flow is not fully developed, especially near the entrance region, the pressure gradient is higher than that in the fully developed region (Chhabra and Richardson, 2008). Therefore, the effect of the entrance region on pressure gradient calculations must be corrected to obtain reliable rheological data from the measurements. The length of the entrance region for a Newtonian fluid is (White 1999)

$$L_e = 0.06ReD \tag{1-86}$$

The value of L_e can be higher especially for the flow of viscoelastic fluids. For purely viscous fluids, in order to minimize the effect of entrance effect on pressure gradient, it is recommended to use capillaries of L/D greater than 100 (Darby R., 1976). For $L/D < 100$, due to the effect of the entrance, calculated wall shear rate values must be corrected, and Bagley correction is frequently performed to determine actual wall shear rate data.

The method requires a minimum of three different geometries of the capillary of the same diameter and different lengths (Chhabra and Richardson, 2008). The method involves sketching curves of measured pressure drop (Δp^*) versus L for the constant apparent wall shear rates and extrapolating the curve to L=0, additional pressure drop ($\Delta p'$) can be found easily. Corrected pressure drop is

$$\Delta p = \Delta p^* - \Delta p' \tag{1-87}$$

From Eq. 1-87 above, the wall shear stress is calculated using corrected pressure drop Δp.

In the case of two capillaries (Darby 1976; Ferguson and Kemblowski, 1991), Coutte method can be used to correct measured pressure drop values. This method required two capillaries of the same diameter and flowing the sample at a constant flow rate.

The lengths of capillaries are L_1' and L_2' ($L_2' > L_1'$). The measured pressure can be written as the sum of pressure drop in a fully developed region and an additional pressure drop due to the entrance effect.

$$\Delta p^*_1 = \Delta p_1 + \Delta p'_1 \quad (1\text{-}88)$$

$$\Delta p^*_2 = \Delta p_2 + \Delta p'_2 \quad (1\text{-}89)$$

Since the flow rate of the samples and diameters of the capillaries are the same, additional pressure drops should be the same for both capillaries.

$$\Delta p'_1 = \Delta p'_2 = \Delta p' \quad (1\text{-}90)$$

The length of capillaries can be expressed as the sum of the length of a fully developed region and the length of the entrance region.

$$L_1' = L_1 + L_{1e}$$

$$L_2' = L_2 + L_{2e} \quad (1\text{-}91)$$

Since additional pressure drops due to the entrance effect are the same for both capillaries, the lengths of entrance regions should be equal ($L_{1e} = L_{2e} = L_e$) and pressure gradients in fully developed regions for both capillaries

$$\frac{\Delta p_1}{L_1} = \frac{\Delta p_2}{L_2} = \frac{\Delta p}{L} = x \quad (1\text{-}92)$$

Substituting Eq. 1-92 into Eq. 1-91, L_1' and L_2' can be written as follows

$$L_1' = L_e + \frac{\Delta p_1}{x} = L_e + \frac{\Delta p^*_1 - \Delta p'}{x} \quad (1\text{-}93)$$

$$L_2' = L_e + \frac{\Delta p_2}{x} = L_e + \frac{\Delta p^*_2 - \Delta p'}{x} \quad (1\text{-}94)$$

Finally, L_2'-L_1' is

$$\frac{\Delta p}{L} = \frac{\Delta p^*_2 - \Delta p^*_1}{L_2' - L_1'} \quad (1\text{-}95)$$

The Eq. 1-95 implies that the corrected pressure gradient can be determined from the ratio of difference of measured pressure values to the difference of the lengths of both capillaries.

b- Wall slip effect

The wall slip effect is frequently encountered in the case of the flow of heterogeneous mixtures such as dispersions, foams, solid-liquid mixtures of high concentration, polymeric fluids, emulsions. The particles within the fluid tend to migrate toward the center of the capillary (Ferguson and Kemblowski, 1991; Macosko, 1994), thereby concentration of particles at the wall should be smaller than average concentration of the fluid and that effect result in lower viscosity near the wall of the capillary. The existence of the slip layer gives rise to obtain a higher apparent shear rate than its actual value for given shear stress (Macosko 1994) and that phenomena can be more significant for capillaries of small diameters. During the measurement of non-homogeneous mixtures such as concentrated slurries, dispersions, etc. by capillary of different diameters, the wall slip effect may lead to obtaining district flow curves instead of one single curve within the same range of shear rates. The wall slip effect is represented by the presence of wall slip velocity (u_s) at the wall of the capillary.

If Eq. 1-64 is solved for the case of wall slip velocity u_s, the total volume flow rate is

$$\dot{V} = \pi u_s R^2 + \frac{\pi R^3}{{\tau_w}^3}\int_0^{\tau_w} \tau^2(-\dot{\gamma})d\tau \qquad (1\text{-}96)$$

On the right-hand side of Eq. 1-96, the first term is the contribution of wall slip velocity to total volume flow rate and the second term is the volume flow rate due to shear flow ($\dot{V}_s$).

If Eq. 1-96 is divided by $\pi R^3 \tau_w$, it can be expressed in terms of the apparent shear rate as follows based on Eq. 1-75.

$$\frac{8\bar{u}}{D\tau_w} = \frac{8u_s}{D\tau_w} + \frac{32\dot{V}_s}{\pi D^3 \tau_w} \qquad (1\text{-}97)$$

On the right-hand side of the Eq. 1-96, the second term is constant for a given wall shear stress and the slope of $8u/D$ to $1/D$ is equal to the wall-slip velocity u_s. From the Eq. 1-97 corrected wall shear rate can be expressed as follows

$$\dot{\gamma}_c = \frac{8(\bar{u} - u_s)}{D} \qquad (1\text{-}98)$$

Where $\dot{\gamma}_c$ is corrected apparent shear rate. Since wall slip velocity is the only function of wall shear stress, the correction method necessitates obtaining an empirical correlation between wall slip velocity and wall shear stress (Ferguson and Kemblowski, 1991).

$$u_s = u_s(\tau_w) \qquad (1\text{-}99)$$

The most frequently used correction method suggested by Mooney (Mooney, 1931) is described simply as follows (Chhabra and Richardson, 2008). The method involves the flow curves from capillaries of different diameters which are obtained from the experimentally measured volume flow rate and pressure drop values. From the district flow curves, apparent shear rate values and corresponding diameter are created for constant values of wall shear stress by interpolation. Then, the apparent shear rate versus $1/D$ is plotted for constant shear stress values. According to Eq. 1-97, the slope of the apparent shear rate versus $1/D$ gives the wall slip velocity for each corresponding wall shear stress, and the empirical relationship between wall slip velocity and wall shear stress can be obtained in this way.

The method described above requires a minimum of three capillaries of different diameters. There is an alternative method that involves the use of two capillaries of different diameters. The method is expressed as follows (Ferguson and Kemblowski, 1991).

For capillaries of diameters D_1 and D_2 Eq. 1-98 can be written as follows

$$\frac{8\bar{u}'_1}{D_1} = \frac{8u_1}{D_1} - \frac{8u_{s1}}{D_1} \tag{1-100}$$

$$\frac{8\bar{u}'_2}{D_2} = \frac{8u_2}{D_2} - \frac{8u_{s1}}{D_1} \tag{1-101}$$

Where $\bar{u}'$ is corrected (non-slip case) mean velocity. It has been stated in the previous section that wall slip velocity is a function of wall shear stress. Hence, for a given constant wall shear stress value wall slip velocities ($u_{s1} = u_{s1} = u_s$) and apparent shear rates of both capillaries should be the same

$$\frac{8\bar{u}'_1}{D_1} = \frac{8\bar{u}'_2}{D_2} \tag{1-102}$$

Hence using Eq. 1-100 and Eq. 1-101, Eq. 1-102 can be expressed as

$$\frac{8u_1}{D_1} - \frac{8u_s}{D_1} = \frac{8u_2}{D_2} - \frac{8u_s}{D_2} \tag{1-103}$$

Finally, wall-slip velocity u_s is

$$u_s = \frac{1}{8}\frac{\frac{8u_1}{D_1} - \frac{8u_2}{D_2}}{\frac{1}{D_1} - \frac{1}{D_2}} \tag{1-104}$$

Eq. 1-104 provides to determine wall slip velocity values for a given wall shear stress values. By performing the interpolation method, the same as in the previous method, empirical correlation is created between wall slip velocity and wall shear stress. Then, utilizing that correlation wall slip velocity is

determined by wall shear stress values from the measurement, and using Eq. 1-98, the corrected wall slip velocity is calculated.

Slit rheometer and flow between parallel plates

A slit rheometer is a thin rectangular channel (Macosko, 1994) and the flow in the slit rheometer is regarded as flow between parallel plates. This assumption can be achieved in practice using a rectangular channel with an aspect ratio (H/W) less than 0.1 (Han, 1971). Thereby, flow is regarded as a one-dimensional and analytical expression between stress and shear rate is available, particularly for non-Newtonian fluids for this geometrical configuration. A slit rheometer provides a direct measurement of the pressure gradient and does not require end correction (Moon and Lee, 2013). Besides, the slit rheometer enables one to determine first normal stress differences (Padmanabhan and Bhattacharya 1984; Aho and Syrjala, 2011).

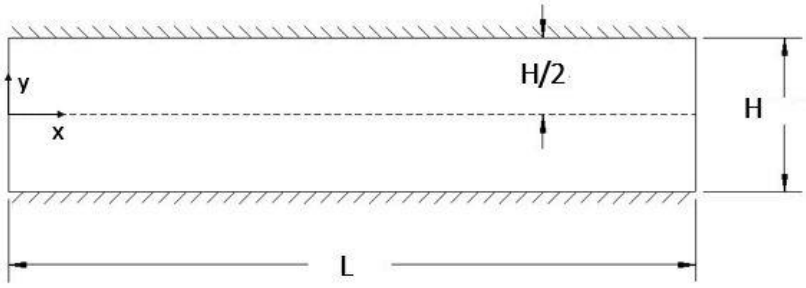

Figure 1-6 Geometrical description of parallel plates

The laminar, steady, fully developed fluid is flowing between parallel plates with a length of L, a width of W, and the gap of H which is depicted in figure 1-6. The velocity of the fluid is assumed on x-direction and varies on the y plane ($u_x = u_x(y) \neq 0, u_y = u_z = 0$) and the velocity of the fluid is zero at the wall ($u_x = 0$ at $y = H/2$)

Due to $u_x = u_x(y), u_y = u_z = 0$, the continuity equation (Appendix A) in the cartesian coordinate system is reduced to

$$\frac{\partial u_x}{\partial x} = 0 \tag{1-105}$$

and from the Cauchy equation (Appendix A), the following expression is obtained

$$\frac{\partial p}{\partial x} = \frac{\partial(\tau_{xy})}{\partial y} \tag{1-106}$$

As shown in the previous section, the left-hand side of the Eq. 1-106 can be stated as follows.

$$\frac{\partial p}{\partial x} = \frac{\Delta p}{L} = \text{constant} \tag{1-107}$$

Substituting Eq. 1-107 into Eq. 1-106

$$\frac{\Delta p}{L} = \frac{\partial(\tau_{xy})}{\partial y} \tag{1-108}$$

The shear stress can be determined by taking the derivative of Eq. 1-108

$$\tau_{xy} = \frac{\Delta p}{L} y + C_1 \tag{1-109}$$

Since velocity exists only in the x-direction ($u_x = u_x(y)$) on the $x - y$ plane, the rate of deformation (Appendix A) is equal to

$$\Delta_{xy} = \Delta_{yx} = \frac{1}{2}\left(\frac{\partial u_x}{\partial y}\right) \tag{1-110}$$

Substituting Eq. 1-109 and Eq. 1-110, into Eq. 1-13,

$$\frac{\Delta p}{L} y + C = 2\mu \frac{1}{2}\left(\frac{\partial u_x}{\partial y}\right) \tag{1-111}$$

The expression of velocity can be obtained by integrating Eq. 1-111. Hence, u_x is given by

$$u_x = \frac{1}{\mu}\left(\frac{\Delta p}{L}\frac{y^2}{2} + C_1 y + C_2\right) \tag{1-112}$$

Since, it has been assumed that the velocity of the fluid at the wall is zero (at $y = -H/2$ and $y = H/2$, $u_x = 0$) the integration constant C_1 is equal to zero and C_2 is

$$0 = \frac{1}{\mu}\left(\frac{\Delta p}{L}\frac{H^2}{8} + C_2\right) \tag{1-113}$$

From Eq. 1-113, integration constant C_2 is

$$C_2 = -\frac{\Delta p}{L}\frac{H^2}{8} \tag{1-114}$$

Since $C_1 = 0$, shear stress is given in Eq. 1-109 equals to

$$\tau_{xy} = \frac{\Delta p}{L} y \tag{1-115}$$

and velocity profile as a function of y and Δp is

$$u_x = \frac{1}{2\mu}\frac{\Delta p}{L}\left(y^2 - \left(\frac{H}{2}\right)^2\right) \tag{1-116}$$

The volume flow rate between the parallel plates is

$$\dot{V} = 2\int_0^{H/2} u_x(y)Wdy \tag{1-117}$$

Substituting Eq. 1-116 into Eq. 1-117

$$\dot{V} = 2\int_0^{H/2} \frac{1}{2\mu}\frac{\Delta p}{L}\left(y^2 - (\frac{H}{2})^2\right)Wdy \tag{1-118}$$

Integrating Eq. 1-118 with respect to y, volume flow rate- pressure drop relationship is obtained as

$$\dot{V} = \frac{(-\Delta p)WH^3}{12\mu L} \tag{1-119}$$

and mean velocity is

$$\bar{u} = \frac{\dot{V}}{S} = \frac{(-\Delta p)H^2}{12\mu L} \tag{1-120}$$

where S is the cross-section area of the channel. Substituting Eq. 1-120 into 1-116, the velocity profile as a function of mean velocity and y is

$$u_x = \frac{6\bar{u}}{H^2}\left(y^2 - (\frac{H}{2})^2\right) \tag{1-121}$$

The shear rate is obtained by taking a derivative of 1-121 with respect to y and the shear rate is

$$\dot{\gamma} = \left(-\frac{du_x}{dy}\right) = \frac{12\bar{u}y}{H^2} \tag{1-122}$$

The viscosity of the Newtonian fluids can be determined by taking the ratio of wall shear stress to the wall shear rate as such in capillary rheometers (at $y = \pm H/2$). Hence, the Newtonian wall shear rate for slit rheometer from Eq. 1-122 is

$$\dot{\gamma}_{Nw} = \frac{6\bar{u}}{H} \tag{1-123}$$

and from the Eq. 1-122, wall shear stress τ_w is

$$\tau_w = \frac{(-\Delta P)}{L}\frac{H}{2} \tag{1-124}$$

Finally, viscosity is determined as follows

$$\mu = \frac{\tau_w}{\dot{\gamma}_{Nw}} \tag{1-125}$$

The Rabinowitsch-Mooney equation for parallel plates can be obtained in the same way like in the circular duct as shown in the previous section. Integrating Eq 1-117 by parts,

$$\dot{V} = 2W\left\{(u_x y)_0^{H/2} + \int_0^{H/2} y\left(-\frac{du_x}{dy}\right)dy\right\} \tag{1-126}$$

Due to boundary conditions, the first term in the bracket is equal to zero.

$$\dot{V} = 2W\left\{\int_0^{H/2} y\left(-\frac{du_x}{dy}\right)dy\right\} \tag{1-127}$$

In order to obtain an explicit expression, the variable y can be replaced with τ_{xy} as follows. The ratio of Eq. 1-115 to Eq. 1-124 is

$$\frac{\tau_{xy}}{\tau_w} = \frac{2y}{H} \tag{1-128}$$

Differentiating Eq. 1-128 and substituting into Eq 1-127, we can obtain the following expression.

$$\frac{2\dot{V}{\tau_w}^2}{WH^2} = \int_0^{\tau_w} \tau_{xy}\left(-\frac{du_x}{dy}\right)d\tau_{xy} \tag{1-129}$$

The stress-shear rate correlation for power-law fluids is obtained by expressing the term of shear rate in Eq 1-129 as τ_{xy}.

$$\frac{2\dot{V}{\tau_w}^2}{WH^2} = \int_0^{\tau_w} \tau_{xy}\left(\frac{\tau_{xy}}{K}\right)^{1/n} d\tau_{xy} \tag{1-130}$$

By integrating Eq. 1-130, the final expression of wall shear rate and shear stress of flow of power-law fluids between the parallel plates in terms of Newtonian wall shear rate is given as follows

$$\tau_w = K(\dot{\gamma}_w)^n = K\left(\left(\frac{2}{3} + \frac{1}{3n}\right)\dot{\gamma}_{Nw}\right)^n \tag{1-131}$$

The method of determining K and n values is the same as in the case of a capillary rheometer. The flow index can be calculated from Eq. 1-82.

Integrating Eq. 1-129 from τ_0 to τ_w with respect to the Herschel-Bulkley model, the relationship $\dot{\gamma}_{Nw}$ and τ_w is given as

$$\dot{\gamma}_{Nw} = \frac{6\dot{V}}{WH^2} = \frac{3}{{\tau_w}^2 K^{1/n}}\left(\tau_0 \frac{n}{n+1}(\tau_w - \tau_0)^{\frac{n+1}{n}} + \frac{n}{2n+1}(\tau_w - \tau_0)^{\frac{2n+1}{n}}\right) \quad (1\text{-}132)$$

Some sources of errors can be encountered during the measurements of rheological properties by slit rheometer. As stated before, slit rheometers provide a direct measurement of pressure, so the end correction is not necessary for slit rheometers. The most frequently encountered source of error is the wall-slip effect. For the slit rheometers of two different H of slits, it is possible to obtain a correlation from Eq 1-104 as follows

$$u_s = \frac{1}{6}\frac{\frac{6\bar{u}_1}{H_1} - \frac{6\bar{u}_2}{H_2}}{\frac{1}{H_1} - \frac{1}{H_2}} \quad (1\text{-}133)$$

The correction method of wall-slip velocity for the slit rheometer is similar to the capillary rheometers. For several values of τ_w, (Ferguson and Kemblowski, 1991) wall slip velocity u_s is determined and a correlation between wall slip velocity and wall shear rate is obtained. From the experimentally determined τ_w values, u_s can be calculated and correction is achieved by subtracting u_s from the experimentally obtained mean velocity. The wall slip correction can be carried by the Mooney method the same as in capillary rheometers. Only the terms D should replace with H and that method requires the measurements from three slits of different H (Mazzanti and Mollica, 2015).

The capillary annulus and rectangular channel rheometer

A slit rheometer is one of the most frequently used pressure-driven rheometers which is a rectangular channel of aspect ratio (H/W) less than 0.1. However, for some cases, the measurement of rheological properties by rectangular channels of any aspect ratio may be required since the rectangular channel is utilized frequently in the industry. There are so few studies related to the measurement of rheological properties of non-Newtonian fluids employing rectangular channels and capillary annulus since there is no straightforward analytical correlation to describe stress-strain relationships for non-Newtonian fluids same as a slit or capillary rheometers (Chhabra and Richardson, 2008).

It has been pointed out that, the rectangular channels of aspect ratios (H/W) less than 0.1, the flow can be assumed as one dimensional. For the aspect ratios greater than 0.1, a one-dimensional flow assumption is not possible (Han, 1971). Especially, it is not possible to express the relationship between shear stress and shear rate analytically for the laminar flow of power-law fluids in rectangular channels of H/W > 0.1 due to the nonlinear partial differential equations (Mitsuishi and Aoyagi, 1969). Therefore, the shear stress-shear rate relationship is expressed by approximate-numerical methods (Crespi-Llorens and

Vicente, 2015). The most frequently used method to imply the wall shear stress-shear rate of the power-law fluids in non-circular channels is a two-parameter model suggested by Kozicki (Kozicki et al. 1966)

$$\tau_w = K\left[(b + \frac{a}{n})\frac{8\bar{u}}{D_h}\right]^n \tag{1-134}$$

From Eq. 1-134, the wall shear rate is

$$\dot{\gamma}_w = (b + \frac{a}{n})\frac{8\bar{u}}{D_h} \tag{1-135}$$

where D_h is the hydraulic diameter for a rectangular channel

$$D_h = \frac{2HW}{(H + W)} \tag{1-136}$$

For a rectangular channel τ_w is the wall shear stress which is given by

$$\tau_w = \frac{(-\Delta p)}{L}\frac{D_h}{4} \tag{1-137}$$

In Eq. 1-134, a and b are geometric parameters that are the function of the cross-section of the channel and geometric ratios. Those parameters are obtained from the Rabinowitsch-Mooney equation for the Newtonian case (see Eqs. 1-84 and 1-131) and the values of a and b are given in table 1 (Kozicki et al. 1966).

It is obvious from Eqs. 1-84 and 1-131 that, $a = 0.25$ and $b = 0.75$ stand for circular cross-sections and $a = 0.5$, and $b = 1$ corresponds to parallel plates and for the Newtonian flow case $(n = 1)$, Eq. 1-134 is

$$\tau_w = \mu(b + a)\frac{8\bar{u}}{D_h} \tag{1-138}$$

In Eq. 1-138, the sum of a and b is

$$(a + b) = \frac{C}{16} \tag{1-139}$$

Where C is equal to the product of friction factor and Reynolds number which is frequently used to predict the friction factor of the laminar flow of a Newtonian fluid in non-circular ducts. The Newtonian shear rate for rectangular channels can be described in terms of C as

$$\dot{\gamma}_{Nw} = \frac{8\bar{u}}{D_h}\frac{C}{16} \tag{1-140}$$

For parallel plates ($D_h = 2H$ and $C = 24$), Eq. 1-140 reduces to Eq. 1-123, and for the circular channel ($D_h = D$ and $C = 16$) to Eq. 1-70.

Son (Son, 2006) was pointed out that measurement of shear viscosity of power-law fluids can be carried out employing rectangular ducts of any aspect ratios relying on Eq. 1-134 and measurement techniques are described briefly as follows.

First, wall shear stress and Newtonian shear rate are determined from the experimentally obtained pressure drop and flow rate values using Eq. 1-137 and Eq. 1-140 respectively. Then flow index is evaluated from Eq. 1-82 by the same way in capillary and slit rheometers. Finally, the consistency K is evaluated from Eq. 1-135.

In addition, the concentric annulus is one of the frequently utilized cross-sectional geometry in the industry just like a circular channel, and is used in applications such as polymer molding, food, and heat transfer processes. Hence, laminar flow in the concentric annulus is studied by many researchers (Ilicali and Engez, 1996) especially for this geometry and the geometry of the concentric annulus is shown in figure 1-7

Table 1-1 a and b values (Kozicki et al., 1966 ; Sestak et al., 1999; Sestak et al., 2001)

Concentric Annuli				Elliptical Duct			
Ri/Ro	a	b	C	Y/X	a	b	C
0	0.25	0.75	16	0	0.3084	0.9253	19.74
0.01	0.3768	0.8751	20.03	0.1	0.3018	0.9053	19.31
0.03	0.4056	0.9085	21.03	0.2	0.2907	0.872	18.60
0.1	0.4455	0.951	22.34	0.3	0.2796	0.8389	17.90
0.2	0.4693	0.9737	23.09	0.4	0.2702	0.8107	17.29
0.4	0.489	0.9911	23.68	0.5	0.2629	0.7886	16.82
0.5	0.4935	0.9946	23.81	0.6	0.2575	0.7725	16.48
0.6	0.4965	0.9972	23.90	0.7	0.2538	0.7614	16.24
0.7	0.4983	0.9987	23.95	0.8	0.2515	0.7546	16.10
0.8	0.4992	0.9994	23.98	0.9	0.2504	0.751	16.02
1	0.5	1	24	1	0.25	0.75	16
Rectangular Duct				Isosceles Triangle			
H/W	a	b	C	θ	a	b	C
0	0.5	1	24	10	0.1547	0.6278	12.52
0.25	0.3212	0.8182	18.23	20	0.1693	0.6332	12.84
0.5	0.244	0.7276	15.55	40	0.184	0.6422	13.22
0.75	0.2178	0.6866	14.47	60	0.1875	0.6462	13.34
1	0.2121	0.6776	14.24	90	0.183	0.6395	13.16
L -shape				Square duct with a centered cylindrical core			
A/B	a	b	C	D/H	a	b	C
0.1	0.3713	1.0101	22.10	0.1	0.378	0.8701	19.97
0.2	0.3299	0.9434	20.37	0.2	0.3987	0.9107	20.95
0.4	0.2628	0.811	17.18	0.4	0.3996	0.9743	21.98
0.6	0.2168	0.7024	14.71	0.6	0.3524	1.0163	21.90
0.8	0.2049	0.6576	13.8	0.8	0.2511	0.9482	19.19
Eccentric Duct							

a	e*	0.1	0.3	0.5	0.7	0.9	0.999
κ							
0.1		0.391	0.316	0.268	0.236	0.216	2.09
0.3		0.408	0.309	0.246	0.204	0.176	0.165
0.5		0.412	0.302	0.233	0.187	0.155	0.142
0.7		0.413	0.298	0.225	0.177	0.144	0.131
0.9		0.413	0.296	0.223	0.173	0.139	0.126
b	e*	0.1	0.3	0.5	0.7	0.9	0.999
κ							
0.1		0.992	0.976	0.884	0.772	0.677	0.641
0.3		1.04	1.009	0.977	0.726	0.595	0.541
0.5		1.056	1.02	0.872	0.704	0.559	0.499
0.7		1.062	1.024	0.869	0.695	0.544	0.482
0.9		1.064	1.026	0.869	0.692	0.539	0.476
C	e*	0.1	0.3	0.5	0.7	0.9	0.999
κ							
0.1		22.13	20.67	18.43	16.13	14.29	43.70
0.3		23.17	21.09	19.57	14.88	12.34	11.30
0.5		8.28	21.15	17.68	14.26	11.42	10.26
0.7		23.60	21.15	17.50	13.95	11.01	9.81

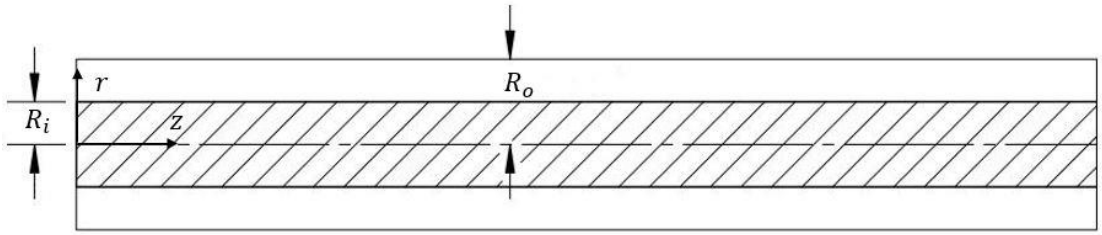

Figure 1-7 Geometrical description of the concentric annulus

In the case of the laminar flow of Newtonian fluids, the velocity profile is given by (Chhabra and Richardson,1999)

$$u_z = \frac{(-\Delta P)R_o^2}{4\mu L}\left(1 - (\frac{r}{R_o})^2 + \frac{1-\kappa^2}{\ln\frac{1}{\kappa}}\ln\frac{r}{R_o}\right) \quad (1\text{-}141)$$

and the volume flow rate is

$$\dot{V} = \frac{(-\Delta P)\pi R_o^4}{8\mu L}\left(1 - \kappa^4 - \frac{(1-\kappa^2)^2}{\ln\frac{1}{\kappa}}\right) \quad (1\text{-}142)$$

Where κ is the aspect ratio defined as

$$\kappa = \frac{R_i}{R_o} \tag{1-143}$$

In the case of non-Newtonian fluids, the laminar flow in the concentric annulus with a high value of κ is regarded as the same in laminar flow in parallel plates (Macosko, 1994). The flow rate in the annulus according to the power-law model can be determined by writing Eq. 1-131 in terms of R_o and κ is given by (Skocilas et al., 2016)

$$\dot{V} = \frac{\pi n R_o^3 \, (1-\kappa)^2 (1+\kappa)}{2(2n+1)} \left(\frac{(-\Delta P) R_o (1-\kappa)}{2KL} \right)^{1/n} \tag{1-144}$$

In the case of the Hershel-Bulkley model, the equation is

$$\dot{V} = \dot{V}_{PL} \left(1 - \frac{2\tau_0}{\frac{(-\Delta P) R_o (1-\kappa)}{L}} \right)^{1/n} \left(1 + \frac{2n\tau_0}{\frac{(n+1)(-\Delta P) R_o (1-\kappa)}{L}} \right) \tag{1-145}$$

where $\dot{V}_{PL}$ is the volume flow rate given in Eq. 1-144 for a power-law fluid. Acquiring a straightforward expression for the velocity profile is difficult since the constant C in the Eq. 1-59 is not zero for concentric annulus so that various methods for the prediction of pressure drop exist in the literature (Ilicali and Engez, 1996). One of the most frequently used methods is suggested by Hanks and Larsen (Hanks and Larsen, 1979) which is based on determining the position of the zero-shear stress (λ_0) and it is given as follows

$$\dot{V} = \frac{\pi n R_o^3}{3n+1} \left(\frac{(-\Delta P) R_o}{2KL} \right)^{1/n} \left[\left((1-\kappa^2)^{\frac{n+1}{n}} - \kappa^{\frac{n-1}{n}} \left({\lambda_0}^2 - \kappa^2 \right)^{\frac{n+1}{n}} \right) \right] \tag{1-146}$$

The values of λ_0 are tabulated in the work of Hanks and Larsen (Hanks and Larsen, 1979).

2-3 The friction factor of power-law fluids in non-circular channels

The friction factor is one of the most frequently utilized design parameters in the industry. It is required to design systems and processes involving fluid flow, particularly for the flow of non-Newtonian fluids since non-Newtonian fluids possess high shear viscosity and the flow of such fluids leads to high-pressure gradients. Therefore, the flow of non-Newtonian fluids mostly takes place laminar flow regime. (Delplace and Leuliet, 1995; Capobianchi, 2008)

The friction factor is a dimensionless parameter that is characterized by the Reynolds number. In the case of Newtonian fluids, an explicit relationship between the friction factor and Reynolds number is available since the exact analytical solution of the flow equations for non-circular ducts is studied by many

researchers (Muzychka and Edge, 2008; Šesták, 1999). For the fully developed flow of a non-Newtonian fluid in non-circular ducts, there is no explicit, generalized friction factor - Reynolds number relationship, due to the existence of non-linear momentum equations which has been mentioned in the previous section (Mitsuishi and Aoyagi, 1969). Explicit correlations for the expression of friction factor-Reynolds number relationship are available only for circular cross-section and parallel plates (Chhabra and Richardson,1999). Friction factor - Reynolds number analysis for the purely viscous, fully-developed flow of power-law fluids in circular ducts under the laminar flow regime was studied by Metzner and Reed (Metzner and Reed, 1955), and they suggested a Reynolds number ($\mathrm{Re_M}$) for determining the friction factor based on Eq. 1-84. The friction factor is defined as the ratio of wall shear stress to the flux of inertial forces

$$\lambda = \frac{\tau_w}{\frac{\rho \bar{u}^2}{2}} \tag{1-147}$$

Where λ is the Fanning factor and 4λ is defined as Darcy–Weisbach friction factor. Introducing Eq. 1-71, for a fully developed laminar flow of Newtonian fluid through circular duct λ, is

$$\lambda \mathrm{Re} = 16 \tag{1-148}$$

Where Re is Reynolds number defined for Newtonian fluids given by

$$\mathrm{Re} = \frac{\rho \bar{u} D}{\mu} \tag{1-149}$$

Similarly, the λRe relationship for laminar flow of Newtonian fluids in non-circular ducts is

$$\lambda \mathrm{Re} = C \tag{1-150}$$

For the fully developed, laminar flow of power-law fluids in circular ducts, substituting Eq. 1-84 into Eq. 1-148, friction factor-Reynolds number relationship is

$$\lambda \mathrm{Re_M} = 16 \tag{1-151}$$

Where $\mathrm{Re_M}$ is the Reynolds number suggested by Metzner and Reed (Metzner and Reed, 1955)

$$\mathrm{Re_M} = \frac{\rho \bar{u}^{2-n} D^n}{8^{n-1} K (0.75 + 0.25/n)^n} \tag{1-152}$$

Concerning fully developed, laminar flow of power-law fluids in non-circular ducts, Kozicki (Kozicki et al. 1966) put forward the following expression for the determination of friction factor based on Eq. 1-134 factor as follows

$$\lambda \mathrm{Re}_G = 16 \tag{1-153}$$

Re_G is the generalized Reynolds number for ducts of non-circular cross-sections

$$\mathrm{Re}_G = \frac{\rho \bar{u}^{2-n} {D_h}^n}{8^{n-1} K (b + a/n)^n} \tag{1-154}$$

As stated before, the geometrical parameters a and b depend on the cross-section of the channel, and geometric ratios (κ) are given in table 1-1. The relationship between parameters a, b, and the coefficient C is given in Eq. 1-139. Also, Sestak (Sestak, 1974) put forward the following relationship related to a and b

$$v = \frac{b}{a} = \frac{2u_{max}}{\bar{u}} - 1 \tag{1-155}$$

Using Eq. 1-139 and Eq. 1-154 the parameters a and b can be written in terms of v and C as

$$a = \frac{C}{16(v+1)} \tag{1-156}$$

$$b = \frac{Cv}{16(v+1)} \tag{1-157}$$

Substituting Eq. 1-156 and Eq.1-157 into Eq.1-153, the expression suggested by Kozicki can be written in terms of v and C such as follows (Delplace and Leuliet, 1995)

$$\lambda \frac{\rho \bar{u}^{2-n} {D_h}^n}{(\frac{C}{2})^{n-1} K \left(\frac{vn+1}{(v+1)n}\right)^n} = C \tag{1-158}$$

The relationship between C and v is

$$v = \frac{48}{C} \tag{1-159}$$

According to the expression given in Eq. 1-158, the generalized Reynolds number is defined as

$$\mathrm{Re}_{DL} = \frac{\rho \bar{u}^{2-n} {D_h}^n}{(\frac{C}{2})^{n-1} K \left(\frac{vn+1}{(v+1)n}\right)^n} \tag{1-160}$$

The proposed method by Delplace and Leuliet (Delplace and Leuliet, 1995) enables the prediction of friction factor by one parameter C and they showed that the maximum deviation between their method

and Kozicki's method is less than 3% for rectangular, elliptical, isosceles triangles, concentric annuli cross-section. Miller (Miller, 1971) has suggested that the friction factor can be predicted readily from Eq. 1-84 by expressing wall shear stress and wall-shear rate using Eqs. 1-137 and 1-140, independently of geometric parameters. However, Delplace and Leuliet (Delplace and Leuliet, 1995) showed that Miller's method induces significant errors for flow index greater than 0.7.

3- Mixing of non-Newtonian fluids

Mixing is a unit operation that is carried out to reduce non-uniformities and obtaining specified property of the final products by the intensification of transport processes. The mixing process can be used for applications such as preparation of suspensions, blending miscible fluids, creating liquid-liquid, liquid-gas dispersions, etc. Liquid mixing operations can be performed by various methods such as mechanical mixing using agitators, pipeline mixing by static mixers, hydraulic and pneumatic mixing by using jets and pressurized gas. In each method, the aim is to create induced fluid flow within the mixing plane (Doran, 2013; McCabe et al., 1993; Paul et al. 2004). In this work, we will mention about mechanical mixing of the fluids only under the laminar flow regime.

The mixing mechanism of the fluids is dependent on the generated flow regime within the mixing medium. In the turbulent flow regime, mixing is characterized by turbulent eddies and specific power consumption generated by impellers. On the other hand, mixing of non-Newtonian fluids takes place in the laminar regime usually due to their high viscosity, thus the flow of fluid is dominated by viscous forces, and providing bulk flow within the vessel is a challenging task. Laminar mixing of liquids is carried out by decreasing the size of the fluid elements by shear and elongational flow and distributing them through the medium.

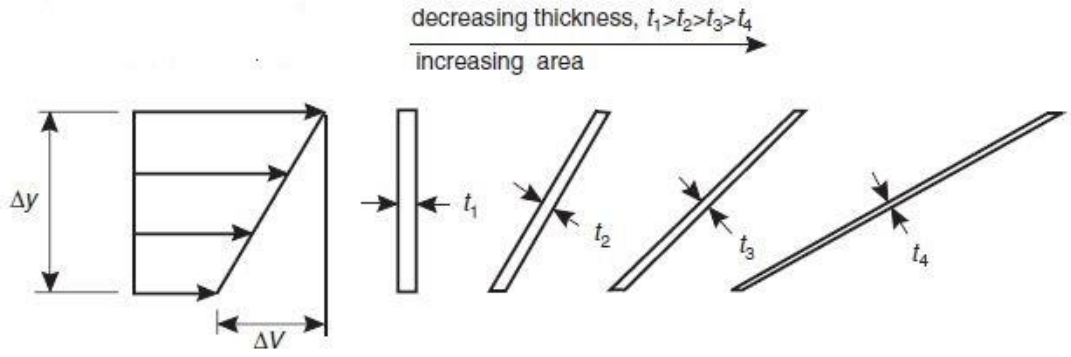

a- Shear flow

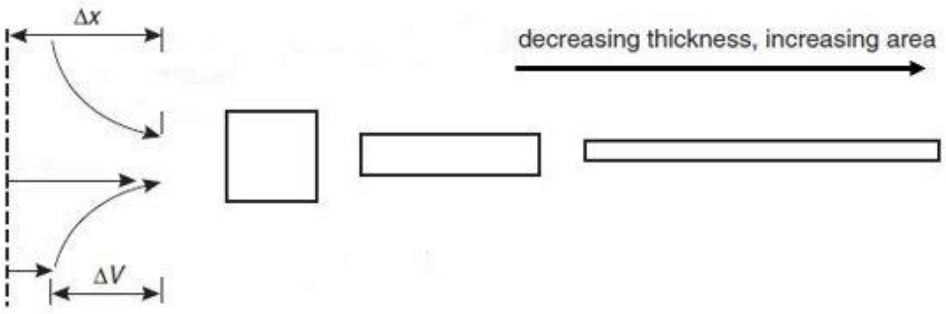

b- Elongational flow

Figure 1-8 Deformation of the fluid element (Chhabra et al., 2008)

In shear flow (see figure 1-7), the relative motion between the streamlines gives rise to deformation of the fluid element, so that the interfacial area of the fluid element increases and gets thinner. The elongational flow causes deformation the same as in the shear flow which is developed due to variation in flow geometry. In elongational flow, converging streamlines accelerate fluid flow and that leads to a decrease in the size of the fluid element which is shown in figure 1-8. Besides, if the fluid element is sufficiently small, the molecular diffusion contributes to the mixing process. However, due to small values of the diffusion coefficient of the viscous fluids, molecular diffusion does not have a remarkable effect on mixing in laminar regime (Harnby et al., 1992; Paul et al. 2004; Chhabra et al., 2008).

The mixing process of the liquid-liquid systems can be classified as distributive and dispersive mixing. In distributive mixing, the aim is spreading all components of mixture uniformly through the entire volume and dispersive mixing is defined as breaking up of the droplet of the dispersed phase by shear and elongational flow, which is carried out by stirred vessels, rotor-stator mixers, static mixers, homogenizers, kneaders, etc. For an efficient mixing of immiscible systems, both dispersive and distributive components should be provided together (Paul et al., 2004).

Mixing operations are frequently carried out in the agitated vessel and flow and required shear in the vessel are provided by impellers, so in this section, we will mention the most frequently used impellers. In the industry, various types of impellers can be used depending on the flow regime and requirements of the mixing process.

As stated before, the flow of fluid in the mixer is provided by impellers which can be classified broadly as turbine and close clearance impellers. Turbine impellers (Paul et al., 2004) are mainly used in the turbulent flow regime and operate at high rotational velocities. On the other hand, close clearance

impellers are used for the agitation of the viscous fluids in the laminar flow regime at low and moderate rotational speeds. Turbine impellers further can be categorized as axial flow and radial flow impellers. In axial flow impellers, (figure 1-9) such as propeller, pitched blade turbine, and hydrofoil impellers are used for blending and preparation of the suspensions. The pumped fluid leaves the impeller in the axial direction. In radial flow impellers, such as Rushton turbine or flat blade impellers, discharged fluid leaves the impeller in the radial direction. They are frequently used for gas-liquid and liquid-liquid dispersion processes.

Axial flow pattern Radial flow pattern

Figure 1-9 Generated flow patterns by turbine impellers (Holland and Bragg, 1995)

Due to their high viscosities, agitation of non-Newtonian fluids is mainly carried out by close clearance impellers such as anchor, paddles, screw impeller, helical ribbon and they operate relatively at a lower speed than turbine impellers and without the requirement of baffles. The most frequently used close clearance impellers are shown in figure 1-10.

Anchor impellers are used for blending and heat transfer applications of the fluids of viscosity in the range of 5 -50 Pa.s. In general, tangential flow is generated by anchor impeller, hence fluid is pumped along its radial arms and sometimes to increase the pumping capacity of the system. On the other hand, this impeller is very efficient if the tank wall is equipped with a jacket and provides a better heat transfer. (Paul et al., 2004; Kuncewicz and Stelmach, 2017).

Helical ribbon impeller is frequently used for the mixing of viscous fluids in the laminar regime. This impeller provides flow (or shear) in a big portion of the vessel and creates axial and radial flow (top-bottom fluid circulation, see figure 1-8) which enhances mixing efficiency.

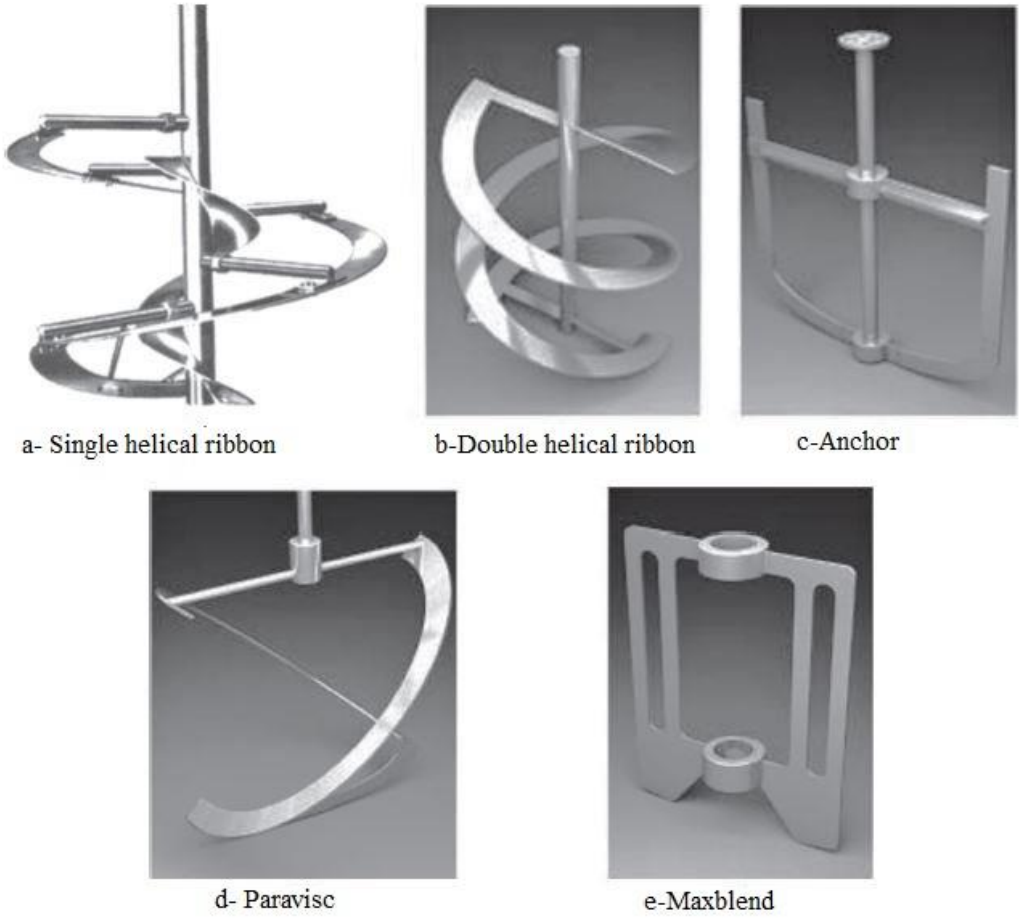

Figure 1-10 Close-clearance impellers (Kresta et al., 2016)

The screw agitator provides agitation of viscous fluids in laminar, transition, and turbulent flow as well. Screw agitator is located off-centered in the vessel or used with a draught tube and this impeller provides excellent axial-radial flow and pumping capacity in the vessel, so gives rise to efficient mixing characteristic.

The materials such as doughs, pastes, polymer melts, and the mixture of fine solids in a viscous liquid possess very high viscosity and mixing of such materials are carried out by kneaders, Baundary mixer, single or twin extruder, and roll-mill.

The kneaders are used for mixing rubbers, dough, and pastes. Kneaders consist of horizontally located vessels and blades. Mainly two types of blades are used which are Z-type or sigma blade is shown in figure 1-11. Those blades provide shear, elongational, and squeezing flow which enhances mixing characteristics at low rotational speed since, during the mixing of very viscous fluids or pastes,

elongational flow is more effective than simple shear flow. Mainly one blade is rotating 1.5 times higher than the other blade and that leads to additional deformations in the mixing medium. The kneaders are mostly used for batch systems. (Chhabra et al., 2008).

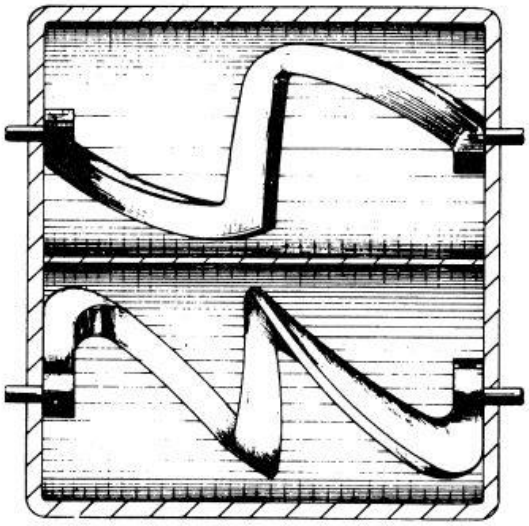

Figure 1-11 Sigma blade kneader (Chhabra et al., 2008).

Single and twin-screw extruders are in-line mixing devices and they are commonly used in the plastic industry for melting and mixing polymers. Those mixers can deliver the processed material at high pressure at a controlled rate from the extruder. Especially twin-screw extruders provide high shear rates in the mixing plane but can lead to excessive heating due to viscous energy dissipation and they are suitable for polymer mixing. Single screw extruders can be used for the mixing of heat-sensitive materials such as food products and mixing should take place at low rotational speed but that may lead to non-uniform mixing due to low shear rates generated by screw (Sonbati, 2012).

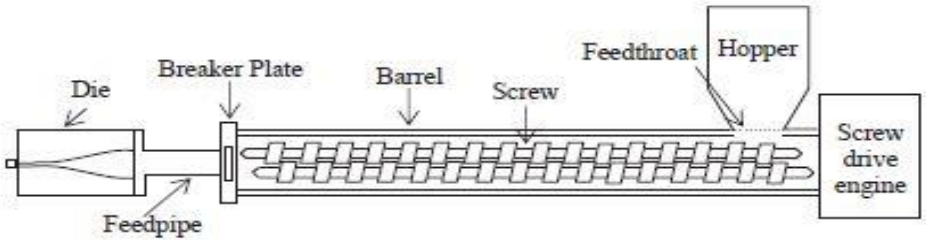

Figure 1-12 Twin screw extruder (Peker and Helvaci, 2008)

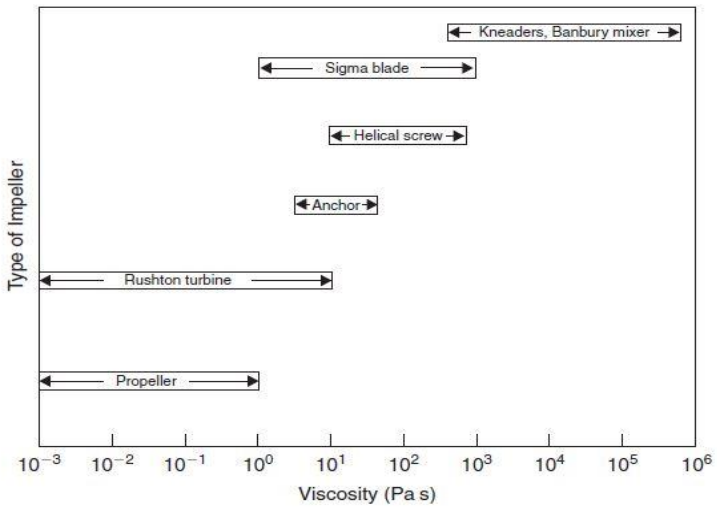

Figure 1-13 Range of viscosity for various impellers (Chhabra et al., 2008).

The mixture of liquid and fine solid at high concentrations exhibits non-Newtonian characteristics. Therefore, blending or dispersion of the fine solids into viscous liquids in a mixer takes place in the laminar flow regime as well and this process is performed in roll-mills. For a proper dispersive mixing of fine solids into viscous liquids, it is necessary to the break-up of the particles which are held together by inter-particle forces, and those processes are carried out by roll-mills which is shown in figure 1-14. The breaking-up of the clusters and dispersion of them into a liquid are carried out in the nip region. The value of stresses in the nip region must be exceeded to separate clusters to provide the desired mixing process (Harnby et al., 1992; Paul et al. 2004; Chhabra et al., 2008).

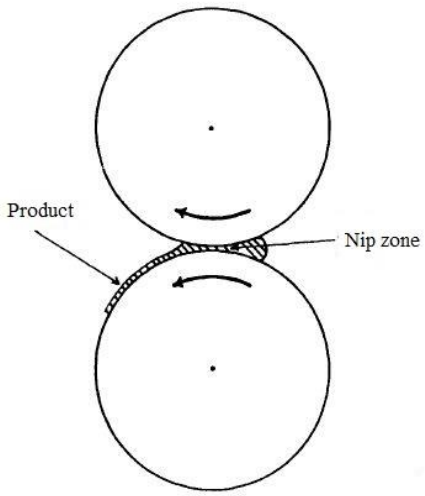

Figure 1-14 Roll mill (Harnby et al., 1992)

On the other hand, rotor-stator mixers can be used for the continuous and batch mixing processes. They are suitable for the processing of fluids of low and high viscosity in laminar and turbulent flow regimes. A rotor-stator mixer is composed of a rotating part, rotor and stationary wall called the stator. There is a narrow gap between rotor and stator which enables the creation of a high shear region. The rotor-stator assembly is called the head or generator. The rotor tip speed can be up to 50 m/s. Rotor-stator mixers provide higher shear and higher power consumption than agitated vessels (Utomo 2009; Paul et al., 2004).

3-1 Dispersion in liquid-liquid systems

In agitated vessels, the dispersion process is achieved by shear stresses generated by the impeller. In general, for an efficient dispersion process, the impeller should provide sufficient shear to break -up drops and pumping capacity in order to obtain homogeneity in the vessel.

In turbulent flow regime, shear stress is characterized by turbulent eddies and if generated mechanical forces by the stirrer are greater than surface forces, a drop can deform to smaller pieces (Paul et al., 2004; Ditl and Sulc, 2016). The size of the created drop (d_p) depends on Kolmogorov length microscale (λ') which is given by

$$\lambda' = \left(\frac{\nu}{\varepsilon^*}\right)^{-1/4} \tag{1-161}$$

Where ν is kinematic viscosity and ε^* is the rate of energy dissipation. If $\lambda' < d_p$, drop size is given for diluted systems by the following expression

$$d_p = C_1 \left(\frac{\sigma}{\rho_c}\right)^{3/5} \varepsilon^{*-2/5} \tag{1-162}$$

Where C_1 is constant and σ is interfacial tension. Alternatively, Eq. 1-162 can be stated in a dimensionless form such that

$$\frac{d_{32}}{D} = C_2 We^{-3/5} \tag{1-163}$$

In Eq. 1-163, d_{32} is Sauter diameter and We is the Weber number which indicates the ratio of inertial forces to surface forces defined as follows

$$We = \frac{\rho_c N^2 D^3}{\sigma} \tag{1-164}$$

As seen from the equations, drop size is directly related to the structure of the fluid and the rate of energy created by the impeller. Hence for a given mixing system, a proper mixing process and impellers should be selected depending on the required size of the droplet since each agitation system has a different characteristic of power consumption, given in figure 1-15.

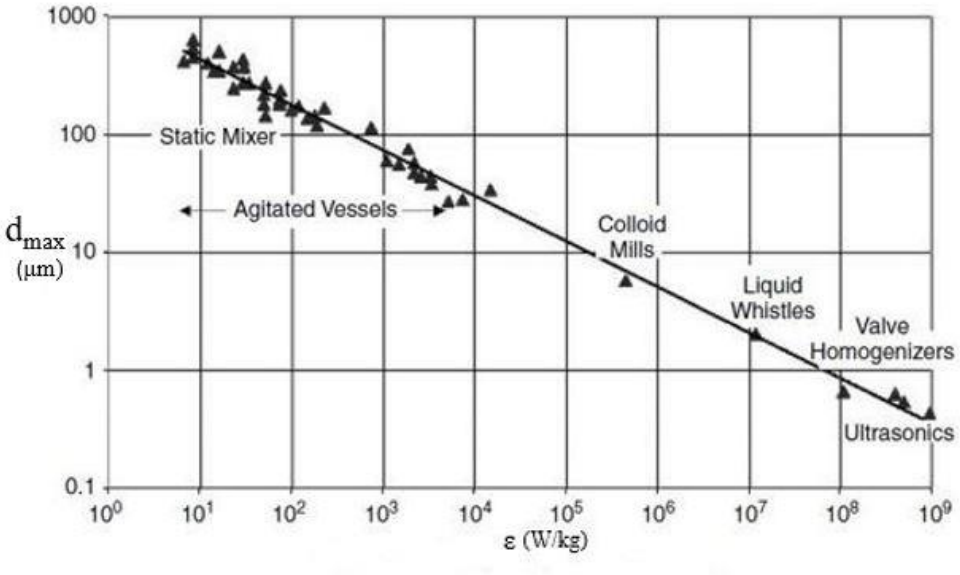

Figure 1-15 Power draw and drop size variation for various dispersion devices (Paul et al., 2004)

In the laminar flow regime, viscous forces dominate the flow of fluid, so that providing bulk flow through the entire vessel is difficult and deformation of the drop is carried out by stresses arising from shear and elongational flows. Therefore, the utilized impeller should occupy a big portion of the cross-section of the mixing vessel (Chhabra et al., 2008).

The dispersion of immiscible fluids by an agitator is characterized by dimensionless Capillary number which is the ratio of viscous forces to interfacial forces to surface forces and viscosity ratio of the dispersed phase (η_d) to continuous phase (η_c) such that

$$Ca = \frac{\eta_c \dot{\gamma} d_{32}}{\sigma}. \qquad (1\text{-}165)$$

where σ is interfacial tension, d_{32} is the Sauter diameter of the dispersed phase and it should be noted that created deformation is proportional to impeller speed. At low values of capillary number, dispersive mixing of viscous liquids in the laminar regime is only possible by elongational flow and at higher values of capillary number drop deformation occurs by shear and elongational flows (Paul et al., 2004; Thakur et al. 2012).

3-2 Power characteristic of agitators in laminar flow regime

Dimensionless numbers are used for the designing and process characterization of a mixer usually. Maybe the most frequently used dimensionless number for the mixing calculation is the mixing Reynolds number

$$\mathrm{Re} = \frac{\rho \mathrm{N} \mathrm{D}^2}{\mu} \tag{1-166}$$

where N is the rotational speed of the impellers and D is the diameter of the impellers. For the mixers, flow is laminar if $\mathrm{Re} < 10$ and fully turbulent for $\mathrm{Re} > 10^4$. The mixers with close-clearance impellers such as anchor and helical-ribbon, mixing is regarded as laminar about $\mathrm{Re} < 100$ (Doran, 2012). Cooke (Cooke et al.,2012) pointed out that laminar flow occurs for $\mathrm{Re} < 1000$ in the case of the Silverson rotor-stator mixer, and Vial (Vial et al., 2015) stated that flow is laminar for $\mathrm{Re} < 100$ for flat blade rotor-stator mixers.

The power consumption of a mixer in dimensionless form is defined by power number which is given as follows

$$\mathrm{Po} = \frac{\mathrm{P}}{\rho \mathrm{N}^3 \mathrm{D}^5} \tag{1-167}$$

In the turbulent regime, Po is constant and in the laminar flow regime, the value of Po depends on the Reynolds number. For Newtonian fluids, the relationship between Po and Re is given by (Netusil and Rieger, 1992)

$$\mathrm{PoRe} = \frac{\mathrm{P}}{\mu \mathrm{N}^2 \mathrm{D}^3} = \mathrm{C} \tag{1-168}$$

where C is the power draw coefficient and is only depends on the geometry of the mixer. Since, non-Newtonian fluids possess high apparent viscosity, mixing of such fluids takes place in the laminar flow regime. However, the determination of Re is problematic since apparent viscosity varies with the shear rate. Metzner (Metzner and Otto, 1957) proposed a method for the determination of shear viscosity by introducing effective shear rate ($\dot{\gamma}_{\mathrm{eff}}$)

$$\dot{\gamma}_{\mathrm{eff}} = \mathrm{k_s N} \tag{1-169}$$

In Eq. 1-169, $\mathrm{k_s}$ is Metzner-Otto coefficient and the value of $\mathrm{k_s}$ is dependent on the type of the impeller and geometrical ratios of the mixer. From Eq. 169, the apparent viscosity (η_a) for the power-law model is given by

$$\eta_a = K(k_s N)^{n-1} \tag{1-170}$$

and Reynolds number in terms of Eq. 1-170 can be written as

$$Re_{MO} = \frac{\rho N D^2}{\eta_a} = \frac{\rho N^{2-n} D^2}{K(k_s)^{n-1}} \tag{1-171}$$

where Re_{MO} is the Reynolds number defined by Metzner and Otto (Metzner and Otto, 1957). The power number-Reynolds number relationship according to Eq. 1-171 is

$$P_o \frac{\rho N^{2-n} D^2}{K(k_s)^{n-1}} = C \tag{1-172}$$

Eq. 1-172 were discussed by Rieger and Novak (Rieger and Novak, 1973) and they defined Reynolds number for power-law fluids as follows

$$Re_{RN} = \frac{\rho N^{2-n} D^2}{K} \tag{1-173}$$

where Re_{RN} is the Reynolds number defined by Rieger and Novak and Eq. 1-172 enables to determine Reynolds number independently of k_s and a very convenient approach for the evaluation of Reynolds number if k_s of the investigated mixer is unknown. The Po- Re_{RN} relationship according to Rieger and Novak is given as follows.

Table 1-2 C and k_s values of some impellers (Kresta et al., 2016)

Impeller	C
Pitched blade impeller	60
Rushton impeller	70
Anchor	170
Helical ribbon	200
Double helical ribbon	300
Kneaders	400-800
Impeller	**k_s**
Turbine	10.00
Anchor	25
Maxblend	20-25
Helical ribbon	30

$$Po_o \frac{\rho N^{2-n} D^2}{K} = C k_s{}^{n-1} = C(n) \tag{1-174}$$

Taking the logarithm of both sides of Eq. 1-174

$$\log C(n) = \log C - (1-n)\log(k_s) \quad (1\text{-}175)$$

According to Rieger and Novak (Rieger and Novak, 1973), the curve of log $C(n)$ versus $1-n$ is a straight line and the slope of curve is equal to k_s.

In terms of Bingham plastic, apparent viscosity in terms of effective shear rate can be defined as (Bertrand et al.,1996)

$$\eta_a = \frac{\tau_o}{k_s N} + \mu_p \quad (1\text{-}176)$$

and P_o- Re relationship for the Bingham plastic is

$$Po \frac{\rho N D^2}{\frac{\tau_o}{k_s N} + \mu_p} = C \quad (1\text{-}177)$$

Bertrand (Bertrand et al.,1996) defined Reynolds number independently of k_s same as the approach of Rieger and Novak for Bingham plastic as follows

$$Re_B = \frac{\rho N D^2}{\mu_p} \quad (1\text{-}178)$$

and introducing Bingham (Bi) number

$$Bi = \frac{\tau_o}{N \mu_p} \quad (1\text{-}179)$$

Hence, Po- Re_B relationship according to Eq. 1-177 can be written as

$$Po Re_B = \frac{CBi}{k_s} + C \quad (1\text{-}180)$$

The first term on the right side of Eq. 1-111 is the power necessary to exceed yield stress and initiating flow, the second term indicates to power for the flow generated by the agitator (Bertrand et al.,1996).

In terms of yield-shear thinning fluids, Herschel–Bulkley model is frequently used to model apparent viscosity of such fluids (see Eq. 1-22) and apparent viscosity can be expressed using the effective shear rate as follows

$$\eta_a = \frac{\tau_o}{k_s N} + K(k_s N)^{n-1} \quad (1\text{-}181)$$

Hence, Reynolds number according to Eq. 1-181 is given as follows

$$Re = \frac{\rho N D^2}{\frac{\tau_o}{k_s N} + K(k_s N)^{n-1}} = \frac{\rho N^2 D^2 k_s}{\tau_o + K(k_s N)^n} \quad (1\text{-}182)$$

and P_oRe expression from Eq. 1-182 is

$$Po\frac{\rho N^2 D^2 k_s}{\tau_o + K(k_s N)^n} = C \tag{1-183}$$

Another important phenomenon related to the agitation of viscous fluids is the formation of caverns. As stated before, the value of the shear rate is maximum near the impeller and it has a minimum value close to the wall of the vessel. Especially in the case of agitation of yield stress fluids, a region in the vessel may be formed where stress generated by the impeller is greater than yield stress is called cavern (sheared zone), and the stagnant region where generated stress by the impeller is less than the yield stress of the fluid which is demonstrated in figure 1-16.

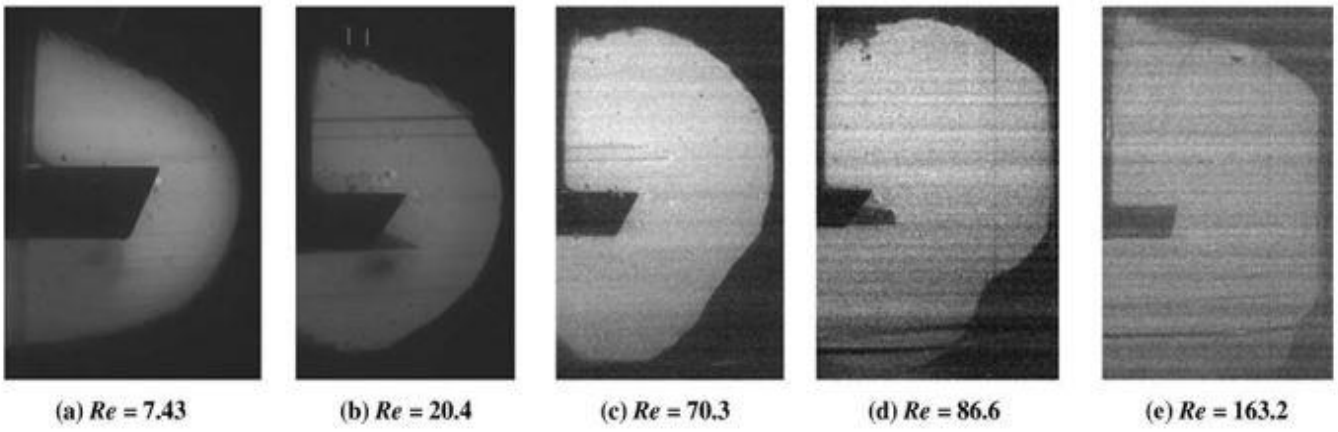

Figure 1-16 Developed caverns in viscoplastic fluid and size increment with Reynolds number (Adams and Barigou, 2007)

Solomon et al. (Solomon et al., 1981) considered the shape of the cavity as spherical and proposed a method for estimation of cavern size based on torque balance which is given as follows

$$\left(\frac{D_c}{D}\right)^3 = \left(\frac{4P_o}{\pi^3}\frac{\rho N^2 D^2}{\tau_0}\right) \tag{1-184}$$

where D_c is the diameter of the cavern. Elson et al. (Elson et al., 1986) re-cast the Eq. 1-184 concerning the cylindrical shape of cavities

$$\left(\frac{D_c}{D}\right)^3 = \left(\frac{P_o}{(\pi^2\frac{h_c}{D_c}+\frac{1}{3})}\frac{\rho N^2 D^2}{\tau_0}\right) \tag{1-185}$$

It should be noted that both correlations given above are valid for $D \leq D_c \leq T$. In some mixing applications of yield stress fluids, cavern formation is unavoidable and thus the prediction of cavern size

is essential to analyze given mixing process and scale-up. For an ideal mixing process, the value of D_c should be close to the diameter of the vessel and cavern volume should occupy a big portion of the vessel.

3-3 Experimental and numerical studies in literature

Researches related to the agitation of the non-Newtonian fluids in the laminar flow regime usually deal with the determination of power consumption, shear rate, and velocity profile regardless of the type of the mixer. Power consumption is one of the uppermost designs and process parameters for the mixers and generated shear rate in the mixing tank is considered as one of the most important parameters of the efficiency for the agitation of non-Newtonian fluids. (Paul et al., 2004; Chhabra et al., 2008)

Determination of power consumption of the agitation of non-Newtonian fluids in laminar flow regime is based on Metzner-Otto coefficient (k_s) and dependency of k_s according to the type of impeller, the geometry of the mixer and rheological model of the agitated fluid have been investigated by various researches and the value of k_s usually depends only on the type of the impeller and the geometrical configuration of the mixer. (Rieger and Novak, 1973)

Iranshahi (Iranshahi et al.,2007) investigated power consumption and mixing time of the Maxblend impeller using viscous Newtonian fluid in the laminar and transition flow regime and effect of baffles on power consumption and shear profile was studied as well. They concluded that the onset of Reynolds number from the laminar to transition region has been found as 25 for unbaffled and 35 for the baffled configurations. Baffles have a significant effect on the shear profile in the vessel. Also, they pointed out that predicted power consumption and mixing time from the CFD and experiments are in good agreement. Similar work has been carried by Mozaffari (Mozaffari and Upreti, 2009). They investigated the power consumption and velocity profile of the shear-thinning yield stress fluid agitated in a batch vessel by the pitched blade, turbine, and marine impellers. They conducted simulation by multiple reference frame method. It has been concluded that a good agreement has been found between the numerically and experimentally obtained results. The MRF method has the potential for the prediction of power consumption in the agitated tank.

Archard (Archard et al., 2006) examined the flow field and power characteristic of the anchor and double helical ribbon impellers for the yield stress fluids numerically. It has been indicated that the flow field and pumping capacity of the investigated mixers are affected by Bingham number (Yield stress), namely pumping capacity decreases with increasing Bingham number.

Cooke (Cooke et al. 2012) studied the power consumption characteristics of an in-line Silverson rotor-stator mixer experimentally using water, silicon oil, and an aqueous solution of carboxymethyl under the laminar and turbulent flow conditions. It has been pointed out that the power number-Reynolds number relationship of an in-line rotor-stator agitator in the laminar flow regime can be expressed the same as a typical batch mixer. However, in the turbulent regime, the power of flowing fluid in the system influences power numbers whereas this effect is negligible in the laminar flow regime. Effect of slots of investigated rotor-stator mixer on Metzner and Otto coefficient was also studied in the laminar flow regime and Metzner and Otto coefficient has been found 45.2 with slots and 6.6 without slots.

Zhang (Zhang et al., 2017) analyzed the power consumption of in-line high shear mixers with ultrafine teeth and the effect of tip-to-base clearance and shear gap width on power consumption and flow field numerically through multiple reference frame (MRF) technique. They concluded that numerically and experimentally obtained power consumption values are in good agreement and it has been found that power and Otto-Metzner coefficient decreases with increasing values of clearance and shear gap.

Vial et al. (Vial et al., 2015) carried out similar work using an in-line, rotor-stator mixer which is composed of flat blades. Their study has been carried out for Newtonian and power-law fluid (xanthan aqueous solution) under the laminar flow condition for the different flow rates by experimental and numerical methods. It has been indicated that power consumption and design parameters such as power and Metzner-Otto constants are significantly affected by the geometry of the mixer and it has been proven that the CFD technique can be used to designing and scaling-up a new designed in-line mixer.

From the mentioned researches above, it can be concluded that numerical methods are a useful tool for the determination of power consumption, shear and velocity profiles for the mixing of non-Newtonian fluids in laminar flow regime and can be utilized for analyzing shear rate, velocity, and power consumption of the investigated mixer in this study

4- Numerical Methods

An accurate and optimum design of equipment or process lines has considerable importance in terms of the quality of the final product, process safety, and cost. However, designing such systems can be challenging since transport equations (mass, momentum, and energy) are described by partial differential equations and the design of complex systems is carried out by experimental or approximate methods. The numerical methods enable us to evaluate partial differential equations using finite element or finite volume methods which are commonly used for designing equipment, or process optimization. The

commercial software ANSYS FLUENT 15 is used for the numerical studies in this study which provides solutions based on the finite volume method. The numerical methods are carried out to achieve the following tasks:

1- Verification of the suggested method for the rectangular slit rheometer.
2- Validation of the suggested method for the prediction of friction factor of the power-law fluids in non-circular ducts
3- Validation of experimentally obtained power draw values of newly designed rotor-stator mixer and for the determination of design parameters such as power constant and Otto-Metzner coefficients as well as, shear rate and velocity profiles.

Any numerical simulation process consists of three steps; pre-processing, simulation, and post-processing which are described briefly as follows.

4-1 Preprocessing

In this step, the fluid domain (geometry) and grids (meshes) are created. The fluid domain is divided into the smaller domain, which is called mesh. In simulations, the flow and energy equations are solved in those meshes. The accuracy of the simulations is directly associated with the structure and number of generated meshes. In 2-D models, the geometry of meshes can be triangular or quadrilateral and in 3-D models, tetrahedron, hexahedron, pyramid, and prism. In addition, grids can be classified as structured and unstructured grids. In structured mesh, cells follow a regular pattern, whereas, in unstructured grids, mesh cells have an irregular pattern. Structured meshes give rise to get a better solution, however, this grid pattern is possible only for regular geometries (ANSYS Fluent, 2013).

4-2 Simulation

This section is composed of selection solution set-up, such as type of solver, selection of the materials, flow regimes, boundary conditions, and solution methods. In this study, all simulations are carried out in the laminar flow regime, using single-phase flow.

FLUENT (ANSYS Fluent, 2013) provides viscosity functions for the inelastic non-Newtonian fluid model. In this study, simulations are conducted for the Newtonian, shear-thinning, and viscoplastic fluids. In the case of viscoplastic fluids, for $\tau < \tau_0$, the shear rate is zero and viscosity has an infinite value which results in convergence problems during the simulation. In FLUENT, critical shear rate ($\dot{\gamma}_c$) is introduced (see figure 1-17) to reduce convergence problems arising from infinite shear rate and at

yield stress, infinite viscosity is replaced by a large but infinite viscosity. Therefore, the viscosity function of the Herschel–Bulkley model in terms of the critical shear rate is:

If $\dot{\gamma}_c > \dot{\gamma}$, the viscosity is

$$\eta = \frac{\tau_0}{\dot{\gamma}} + K\left(\frac{\dot{\gamma}}{\dot{\gamma}_c}\right)^{n-1} \quad (1\text{-}186)$$

If $\dot{\gamma}_c < \dot{\gamma}$

$$\eta = \frac{\tau_0\left(2 - \frac{\dot{\gamma}}{\dot{\gamma}_c}\right)}{\dot{\gamma}_c} + K\left[(2-n) + (n-1)\frac{\dot{\gamma}}{\dot{\gamma}_c}\right] \quad (1\text{-}187)$$

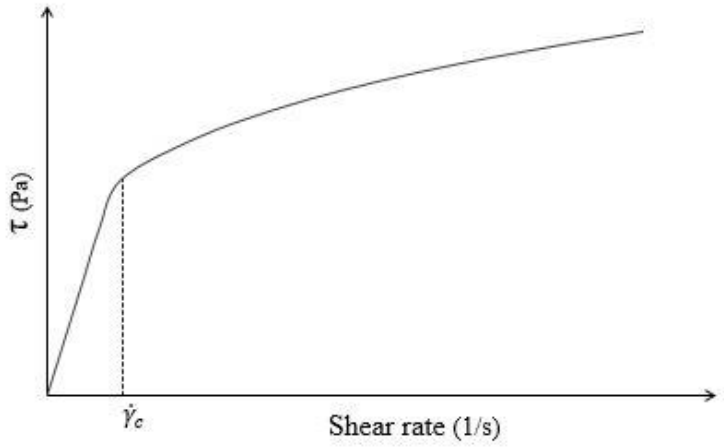

Figure 1-17 Critical shear rate versus shear stress

In this study, numerical simulations are carried out for the modeling of the designed rotor-stator mixer, hence in this section, we mention the methods for the simulation of agitators briefly. There are two main approaches for the modeling of moving fluid domains which are moving reference frame and dynamic mesh methods. In moving reference frame, the shape of the fluid domain does not change when it moves, whereas in the dynamic mesh the shape of the fluid domain change as it moves (ANSYS Fluent, 2013). Moving reference frame approach fits for the modeling of agitation, hence the methodology of this approach is addressed here. There are three different approaches to the moving reference frame.

Single reference frame: In the single reference frame (SRF), the whole fluid domain is considered as rotating concerning a determined axis and it is the simplest method for the modeling of the rotational bodies. It is important to note that in SRF, the walls are stationary and must be considered as the surface of revolution.

Multiple reference frame: It is a steady-state model and a frequently used method for modeling mixers since this model enables less expensive computations. In the MRF approach, the domain of the fluid is divided into moving reference frame and stationary zone by an interface which is the surface of the revolution. The interface between the zones can be conformal or non-conformal interfaces. In the conformal interface, cell zones are physically connected, and the number of mesh elements is equal on both sides of the zones, namely zones are connected by the same nodes. In the non-conformal interface, the surface of the interphase composes of two overlapping surfaces and the number of nodes and mesh elements on both sides of the surfaces are not the same. The MRF method does not consider the relative motions of the zones to each other, so mesh geometry does not change. Therefore, this method is only suitable for steady-state cases. In this study, simulations of rotor-stator mixers are carried out by using the MRF method.

Sliding Mesh: The sliding mesh approach is very similar to the MRF method. The domain is divided into the rotational and stationary bodies by only creating non-conformal interphase between the two bodies. Unlike the MRF method, in the sliding mesh method the relative motion between the rotating and stationary zones is considered, namely, grids are moving. Hence, this method provides numerical solutions for unsteady flow cases and provides more realistic results than the MRF method, but the sliding mesh method is computationally more expensive than the MRF method.

In all simulations in this work, the pressure-based solver is selected. For the solution method, the SIMPLE algorithm was applied for the pressure-velocity coupling which is a widely utilized procedure to solve the momentum equation iteratively.

4-3 Post-Processing

The final step of numerical simulation is the post-processing step. After getting the numerical solution, the desired properties are analyzed as magnitude or vectors which is shown in the result part of the mixing section in this study. In FLUENT, the obtained specified property such as velocity, pressure, etc. is expressed in the cartesian coordinate system. In this work, acquired data from the simulations are converted to the cylindrical coordinate system using MATLAB codes.

4-4 Grid Convergence Index

One of the most important procedures of numerical simulation is the estimation of the optimum number of grids (meshes) for the numerical simulation. The accuracy of numerical simulation is dependent on the size (number) of created grids and the accuracy of the solution is increased by refining the meshes.

The result of a simulation reaches an asymptotic (accurate) value for the infinitely large number of mesh elements. However, performing a simulation with a very high number of mesh elements is computationally expensive and leads to higher computational time. Therefore, the determination of the appropriate number of mesh elements is required for the simulations which should be within a certain interval of the accurate result. The grid convergence index (GCI) is a frequently used method for evaluation of the discretization errors and GCI indicates how far the computed value is away from the accurate value (Rorache, 1998; Celik et al. 2008; Elsayed and Lacor, 2013). In this study, an optimum number of mesh elements is evaluated by applying the GCI method suggested by Celik et al. (Celik et al., 2008) and the method is described as follows.

The relationship between the result of the numerical solution and the number of mesh element is given by the following equation

$$\phi = \phi_{ext} + ah^p \tag{1-188}$$

where ϕ is the result of the numerical solution for the given number of mesh and ϕ_{ext} is the extrapolated value of the solution for the infinitely large number of mesh elements. The coefficient a is a fitting parameter, p indicates the order of the solution accuracy, and h is given by

$$h = \left(\frac{1}{N}\right)^{1/D} \tag{1-189}$$

In Eq. 1-189, N is the number of mesh elements and D is the dimension of the performed numerical simulation (2 in 2-D case, and 3 in 3-D). Eq. 1-188, has three unknown parameters (ϕ_{ext}, p, a), hence the solution of the Eq. 1-189 requires the result of the numerical solution for 3 different mesh sizes. Therefore Eq. 1-188 is written as follows

$$\begin{aligned} \phi_1 &= \phi_{ext} + ah_1{}^p \\ \phi_2 &= \phi_{ext} + ah_2{}^p \\ \phi_3 &= \phi_{ext} + ah_3{}^p \end{aligned} \tag{1-190}$$

If we assume that $h_1 < h_2 < h_3$ and $r_{21} = h_2/h_1$, $r_{32} = h_3/h_2$, the term p can be calculated by the following equation

$$p = \frac{1}{\ln r_{21}}\left[\frac{\varepsilon_{32}}{\varepsilon_{21}} + \ln\frac{r_{21}{}^p - 1}{r_{32}{}^p - 1}\right] \tag{1-191}$$

where $\varepsilon_{21} = \phi_2 - \phi_1$, $\varepsilon_{32} = \phi_3 - \phi_2$ and the value of p is evaluated numerically. After obtaining the value of p, ϕ_{ext} is determined by

$$\phi_{ext} = \frac{\phi_1 {r_{21}}^p - \phi_2}{{r_{21}}^p - 1} \quad (1\text{-}192)$$

From Eq. 1-192, the accuracy of numerical solution for the finest mesh is expressed in terms of GCI (Grid Convergence Index) as

$$GCI_{21} = \frac{1.25 * (\phi_{ext} - \phi_1)}{\phi_1} = \frac{1.25 e_{a21}}{{r_{21}}^p - 1} \quad (1\text{-}193)$$

In Eq. 1-193, 1.25 is the safety factor and e_{a21} is

$$e_{a21} = \frac{(\phi_1 - \phi_2) * 100}{\phi_1} \quad (1\text{-}194)$$

The same expression can be written for the middle size of mesh as well

$$GCI_{32} = \frac{1.25 e_{a32}}{{r_{32}}^p - 1} \quad (1\text{-}195)$$

where e_{a32} is

$$e_{a32} = \frac{(\phi_2 - \phi_3) * 100}{\phi_2} \quad (1\text{-}196)$$

For the 3-D simulations, the ratio between the number of mesh elements should be higher than 2.2 and for 2-D simulations, this ratio is 1.7.

Chapter 2 -Objectives of the Study

Mixing and transportation of the non-Newtonian fluids are commonly encountered processes in the industry. For the transportation of the non-Newtonian fluids, the essential design and process control parameter is the pressure drop which is necessary for the sizing of the channels and selection of the pumps in the system. Especially, the friction factor-Reynolds number relationship for the fully developed laminar flow of power-law fluids through non-circular channels relies on approximate methods. And in these methods, Reynolds numbers are the function of the shape of the channel and geometric ratios. Moreover, available methods are not practical for the estimation of the pressure drop.

Regarding the laminar mixing of the non-Newtonian fluids, the essential design and process parameter is the power consumption of the mixer, and dimensionless power and Metzner-Otto coefficients are necessary for the determination of the power demand of the mixer in the laminar regime. In the case of the mixing of viscoplastic fluids, the total energy is dissipated in the mixer to overcome yield stress for initiating flow and providing fluid flow, however, there is no explicit correlation to express them individually. Furthermore, there is no practical method for the estimation of the Metzner-Otto coefficient for the laminar mixing of viscoplastic shear-thinning fluids. Determination of the rheological parameters of the purely viscous fluids is essential for the design of the systems, prediction of the pressure drop or power demand of the mixer, and usually capillary or slit rheometers are employed for the determination of the rheological parameters.

In this work, based on the mentioned applications and cases mentioned above, we aim to propose practical and alternative methods and correlations for the transportation and mixing of non-Newtonian fluids. The objective of this work is listed as follows

- To show that rectangular channels and concentric annulus can be used for the determination of rheological parameters of the power-law fluids as capillary and slit rheometers. An alternative, one parameter correlation will be suggested for the estimation of the rheological parameters.
- To propose a new and very simple correlation for the prediction of the pressure drop for the laminar flow power-law fluids through non-circular channels by using geometrically independent

Reynolds number and expressing friction factor-Reynolds number relationship by a simple linear equation.

- Analyzing power characteristics and flow profiles of an in-line rotor-stator mixer experimentally and numerically using shear-thinning viscoplastic fluid under the laminar regime. And then, suggesting expression to specify the effect of yield stress on the power demand of a mixer. Finally, proposing a practical method for the determination of the Metzner-Otto coefficient for the Herschel–Bulkley fluids.

Chapter 3 - Rectangular Channel Rheometer and a Method for the Prediction of Friction Factor of Power-Law Fluids

In this section of our study, firstly, a simple and unique method is introduced for the determination of the shear viscosity of power-law fluids utilizing rectangular channels and capillary annulus. The suggested method is compared with existing methods analytically, experimentally, and by means of numerical simulations. Then, on the basis of the suggested method, a very simple equation is introduced for the prediction of the friction factor of the power-law fluids in non-circular channels.

1- Rectangular and capillary annulus Rheometers

The shear viscosity is one of the most measured rheological properties of the fluids which is necessary for piping, mixing process, heat transfer, and process control, and as stated earlier the measurement of shear viscosity is carried by using a slit or capillary rheometers at high shear rates of the fluid. On the other hand, it might be necessary to measure shear viscosity using rectangular channels or capillary annulus since these geometrical cross-sections are frequently encountered in the industry and there are few works in literature for the measurement of shear viscosity by capillary annulus and rectangular channels. However, the required equations for the prediction of shear viscosity can be complicated and requires more than one parameter. In this section, a simplified method is proposed for the measurement of shear viscosity using only one parameter especially for the rectangular and capillary annulus cross-sections.

The correlation is given in Eq. 1-134 successfully to characterize the wall shear stress-shear rate relationship, but it is not so practical due to the existence of two parameters a and b. A simpler approach can be obtained by expressing the wall shear stress -wall shear rate relationship by one parameter C (see Eq. 1-139) instead of a and b relying on the method suggested by Ayas (Ayas et al. 2019-a). The methodology of simplification is described as follows. If the term $(b + a/n)^n$ in Eq. 1-134 is defined as α.

$$\alpha = (b + a/n)^n \tag{3-1}$$

The ratio of α to $(0.75 + 0.25/n)^n$ is ε

$$\varepsilon = \left(\frac{4(bn + a)}{3n + 1}\right)^n \tag{3-2}$$

The curves of the ε versus flow index (n) for rectangular channel and concentric annulus with the aspect ratios between zero and one are demonstrated in figure 3-1. Ayas et al. (Ayas et al., 2019-a; Ayas et al., 2020-a) has suggested that the ε can be assumed as a linear function of flow index for $0 < n < 1$ for the rectangular channel and concentric annulus. Hence Eq. 3-2 can be expressed as follows

$$\varepsilon = Mn + N \tag{3-3}$$

As flow index n approaches zero, the limit of ε in Eq. 3-2 equals one which can be seen from the plot in figure 3-1.

$$\lim_{n\to 0}\left(\frac{4(bn+a)}{3n+1}\right)^{n} = \lim_{n\to 0}(Mn+N) = 1 \tag{3-4}$$

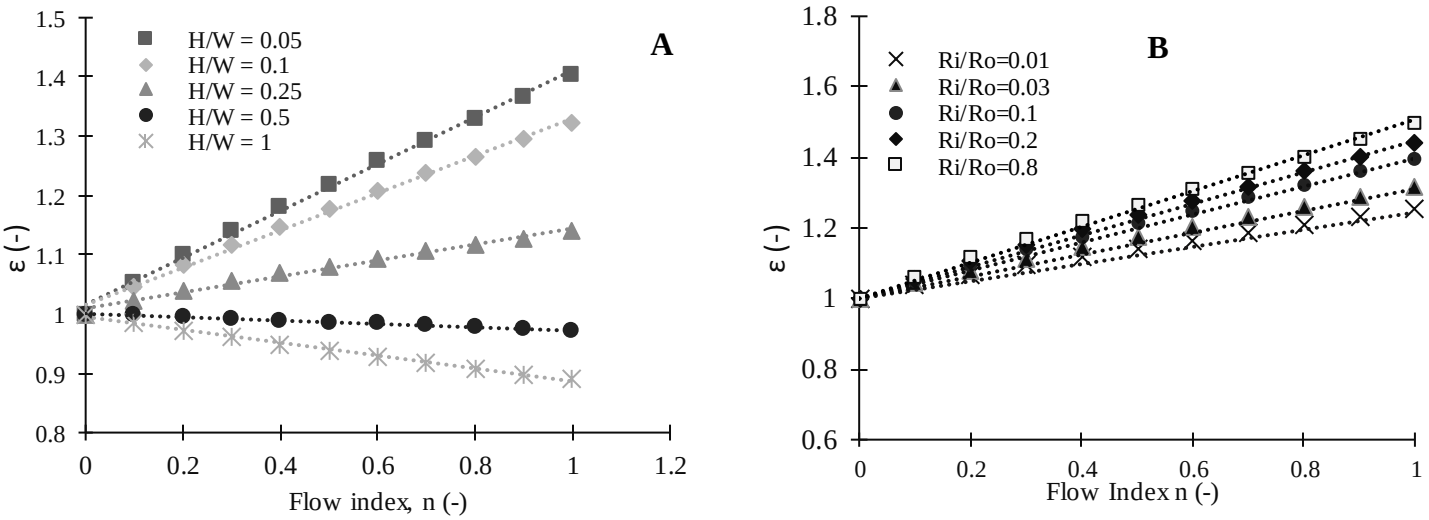

Figure 3-1 Relation between ratio ε and flow index n, (A) – Rectangular channel (B)- Concentric Annuli (Ayas et al., 2019-a; Ayas et al., 2020-a)

Therefore, constant N should be equal to one. The coefficient M can be obtained for the Newtonian flow case. For $n = 1$, ε given in Eq. 3-4 reduces to Eq. 1-138 and the coefficient M can be found as

$$M = \left(\frac{C}{16} - 1\right) \tag{3-5}$$

From the obtained correlations given in Eq. 3-4 and Eq. 3-5, the Eq. 3-1 (α) can be expressed by one parameter as follows

$$\alpha = (b + a/n)^{n} = (Mn+1)\left(\frac{3n+1}{4n}\right)^{n} \tag{3-6}$$

Consequently, Eq. 1-134 can be stated as

$$\tau_w = K((\frac{C}{16} - 1)n + 1)\left[\left(\frac{3n+1}{4n}\right)\frac{8u}{D_h}\right]^n \quad (3\text{-}7)$$

and the wall shear rate is

$$\dot{\gamma}_w = \left[(\frac{C}{16} - 1)n + 1\right]^{1/n}\left(\frac{3n+1}{4n}\right)\frac{8u}{D_h} \quad (3\text{-}8)$$

As seen from Eq. 3-7 and Eq. 3-8, the wall shear rate-wall shear stress can be expressed only one geometrical coefficient C instead of a and b (Ayas et al., 2019-a; Ayas et al., 2020-a). The determination procedure of shear viscosity power-law fluids is the same as the method provided by Son (Son, 2006), only two parameters can be replaced by one parameter model given in Eq. 3-6.

A similar correlation can be obtained by using the parameters of parallel plates ($a = 0.5$ and $b = 1$) instead of the parameters of the circular channel ($a = 0.25$ and $b = 0.75$). If the ratio of $(1 + 0.5/n)^n$ to Eq. 3-1 is defined as ε'

$$\varepsilon' = \frac{(1 + \frac{0.5}{n})^n}{(b + \frac{a}{n})^n} = \left[\frac{2n+1}{2(bn+a)}\right]^n \quad (3\text{-}9)$$

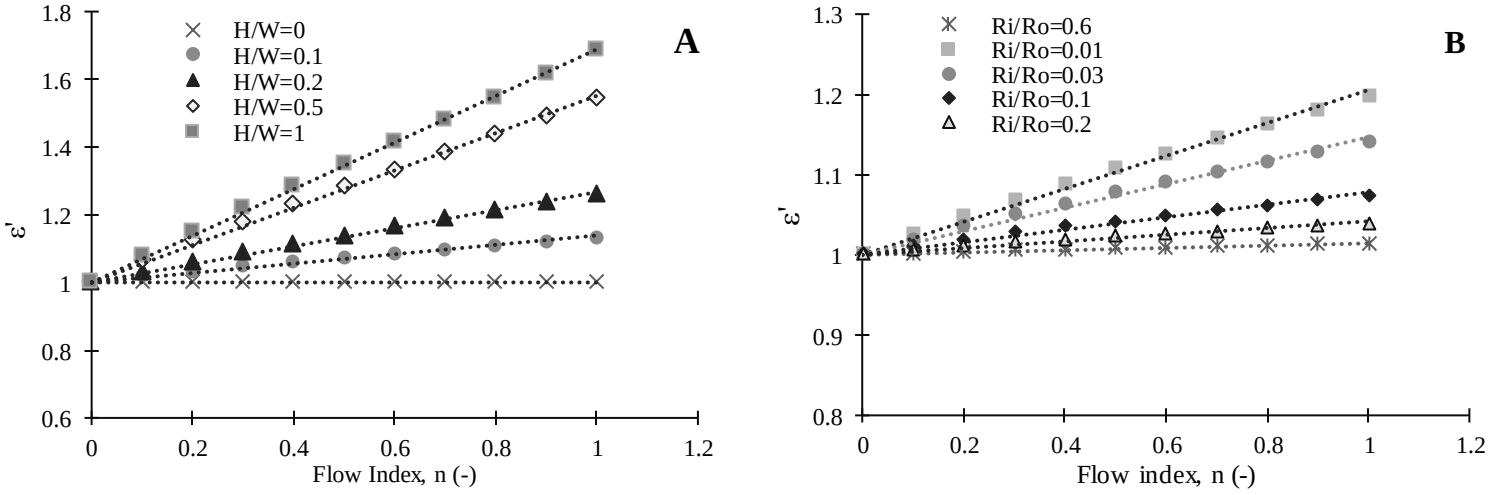

Figure 3-2 Approximated linear variation of ε' (A)- Rectangular channel, (B) - concentric annulus

The variation of $\varepsilon'$with respect to flow index in the range of $0 < n < 1$ and geometric ratios for the investigated cross-sections are given in figure 3-2. From the regression analysis ε'can be assumed as a linear function of flow index and geometric ratios the same as Eq. 3-3. Therefore Eq. 3-9 can be written for $0 < n < 1$ as

$$\varepsilon' = M'n + N' \tag{3-10}$$

As flow index n approaches zero, the limit of ε' equals one, hence the constant N'should be equal to one, and the term $(b + a/n)^n$ can be written as

$$\alpha = (b + \frac{a}{n})^n = \frac{\left(1 + \frac{0.5}{n}\right)^n}{M'n + 1} \tag{3-11}$$

The value of M' can be determined from the Newtonian flow case as

$$M' = \frac{24}{C} - 1 \tag{3-12}$$

and substituting Eq. 3-11 into Eq. 1-134, wall shear stress is given as follows

$$\tau_w = \frac{K}{M'n + 1}\left[\left(\frac{2n + 1}{2n}\right)\frac{8u}{D_h}\right]^n \tag{3-13}$$

The suggested method for the determination of K and n values can be described briefly as follows. Firstly, wall shear stress and apparent shear rates are determined from the Eqs. 1-137 and 1-140 from the measured pressure and volume flow rate values and using Eq. 1-82 flow index n is obtained. Finally using Eq. 3-8 or Eq. 3-13, the consistency K is determined.

In both methods, the way of determination of wall shear stress and flow index are the same and the difference is arising from the calculation procedure of consistency (K). For the rectangular channel with higher aspect ratios or concentric annulus of lower values of aspect ratios, Eq. 3-7 is recommended for the determination of K and the geometries with narrow gaps, Eq. 3-13 gives better results for the prediction of K.

1-1 Validation and discussion

The provided method is validated analytically and experimentally. Ayas et al. (Ayas et al., 2019-a, Ayas et al., 2020-a) validated the suggested α functions given in Eq. 3-6 and Eq. 3-11 with Eq. 3.1 analytically which is shown in figure 3-3. From the comparison, the maximum deviation between the equations was found less than 2.5%.

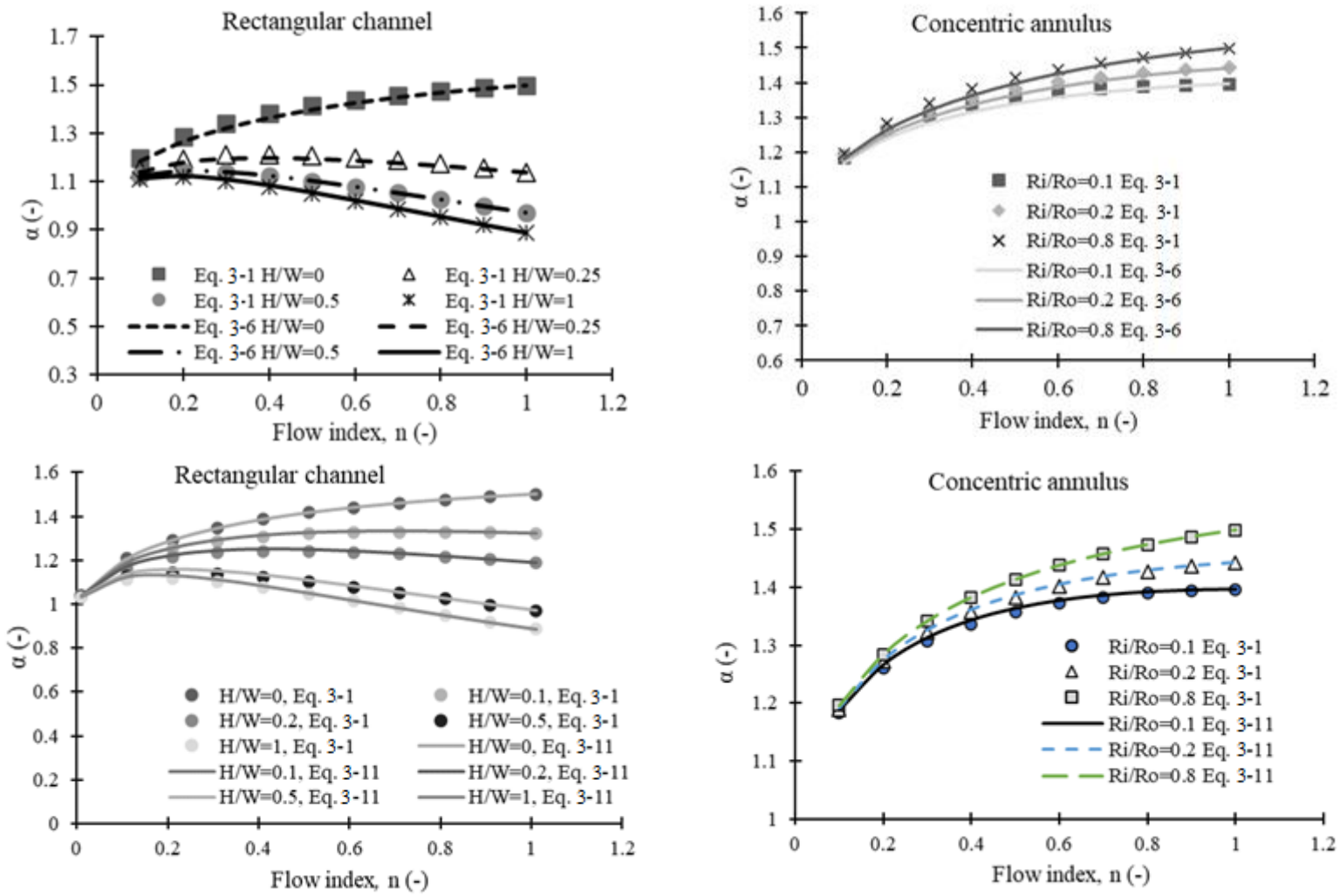

Figure 3-3 Variation of α functions (Ayas et al., 2019-a; Ayas et al., 2020-a)

The proposed correlation has been verified through experimental data available in the literature (Skocilas et al, 2017). Experiments were conducted in a piston-driven extrusion rheometer for the investigation of the rheological properties of the water solution of bovine collagen with a mass fraction of 9.5 % and density of 1100 kg/m^3. The channel used in the experiment has a rectangular cross-sectional geometry with a length of 200 mm and a width of 20 mm (see figure 3-4). Three different heights of channels were utilized in the experiment with the heights of 1 mm, 2 mm, and 4 mm. The rectangular channels were equipped with five pressure transducers which were mounted along the lower surface of the channels and locations of transducers are shown in figure 3-4. The flow in the die channels was provided by the movement of the piston. The measurement was repeated ten times for each die and extruded materials were not reutilized. In this study, experimental data of die with height (H) 2 mm and 4 mm was taken into account for the validation of the proposed correlation. Measured pressure values from the transducers

with corresponding mean velocities within the fully developed region of the dies for the channels of 2 mm and 4 mm are demonstrated in figure 3-5.

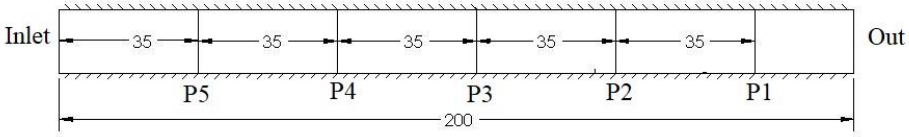

Figure 3-4 Locations of pressure sensors (Skocilas et al., 2017).

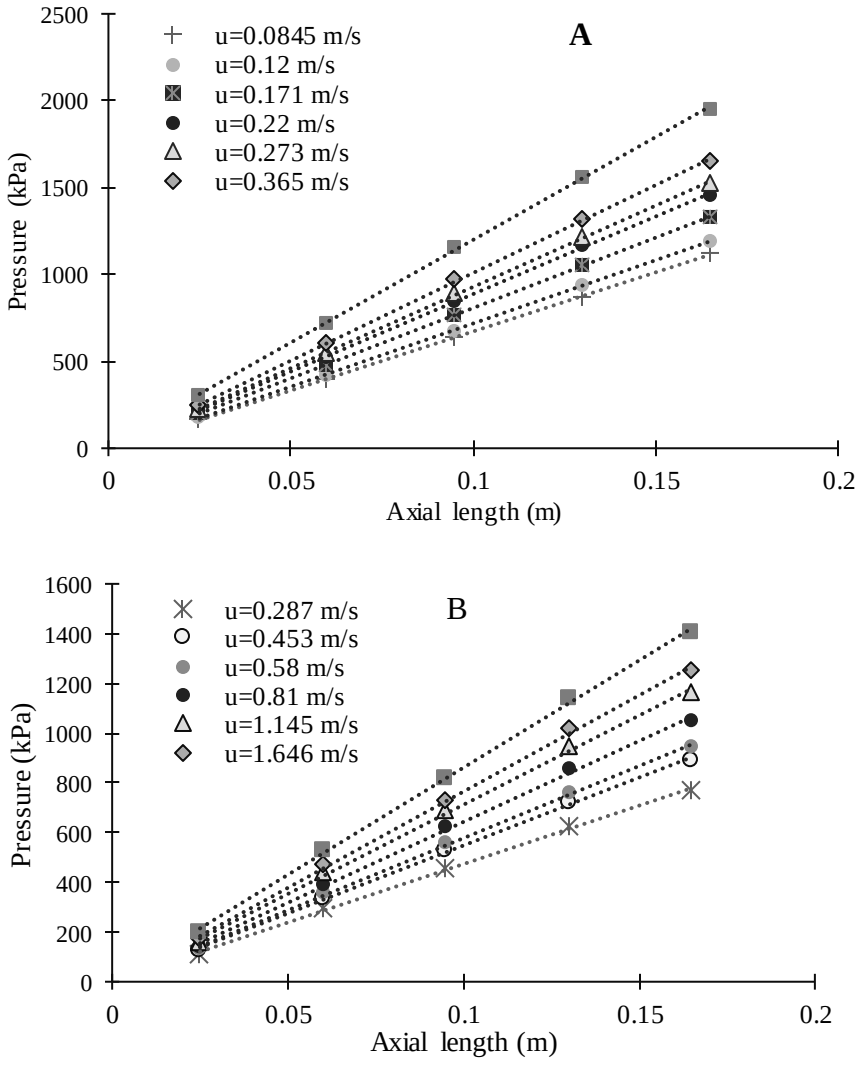

Figure 3-5 Experimentally measured pressure vs mean velocity (A) H= 2 mm, (B) H=4 mm (Skocilas et al., 2017)

The channel with a height of 2 mm has an aspect ratio of 0.1 and can be regarded as a slit rheometer (Han, 1971). From the experimentally measured pressure and volume flow rate values, the flow curve is

obtained from Eq. 1-131 for the power-law model with a coefficient of determination (R^2) greater than 0.99 which is given in figure 3-6-a. The consistency and flow index values were found as $K = 1238$ Pa. s^n and $n = 0.275$ respectively.

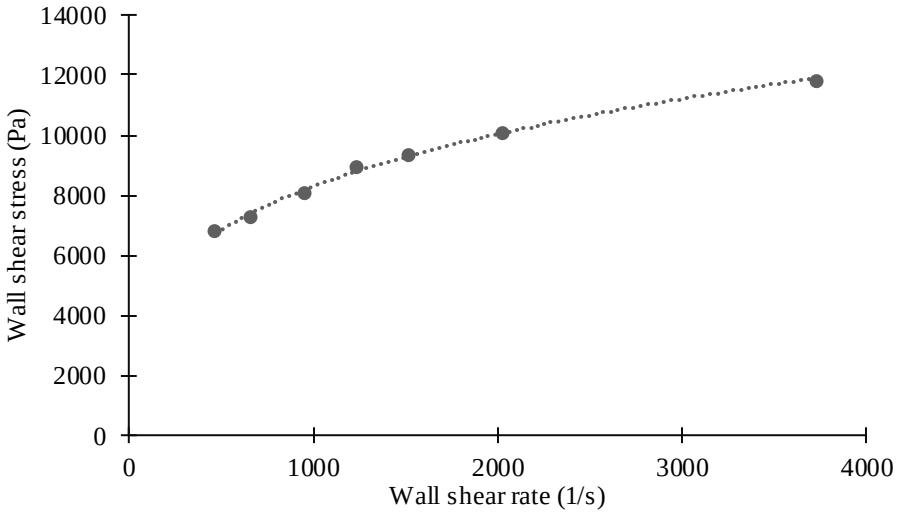

a- Flow curve of channel H/W=0.1, $\dot{\gamma}_w = 470 - 3700$ (1/s)

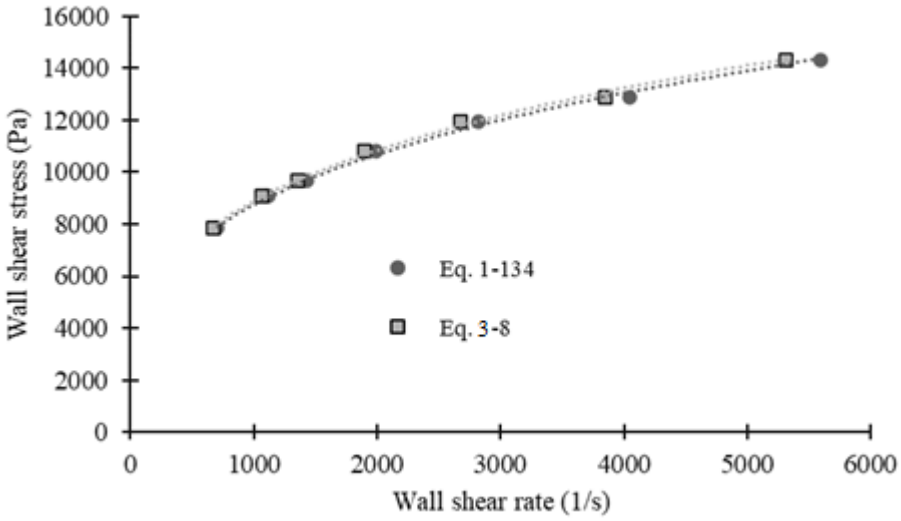

b- Flow curve of channel H/W=0.2 $\dot{\gamma}_w = 670 - 5500$ (1/s)

Figure 3-6 Obtained flow curves from the experimental data

The channel with a height of 4 mm has an aspect ratio of 0.2. It is convenient for the investigating validity of the suggested correlations. Obtained curves from the Eq. 3-1 and Eq. 3-8 are given in figure 3-6-b. As

seen from the curves, obtained flow curves are almost coincident. Determined wall shear rates are approximately the same at low shear rates and deviate slightly at high shear rates. The flow index has been found as 0.288 for both methods. The consistency K has been evaluated as 1197 $Pa.s^n$ from Eq. 3-1 and as 1213 $Pa.s^n$ from Eq. 3-8 respectively which are almost the same. The obtained overall flow curve for the dies with H of 2 mm and 4 mm with a coefficient of determination of 0.98 is shown in figure 3-7. The flow index has been found as 0.3 and consistency is 1060 $Pa.s^n$.

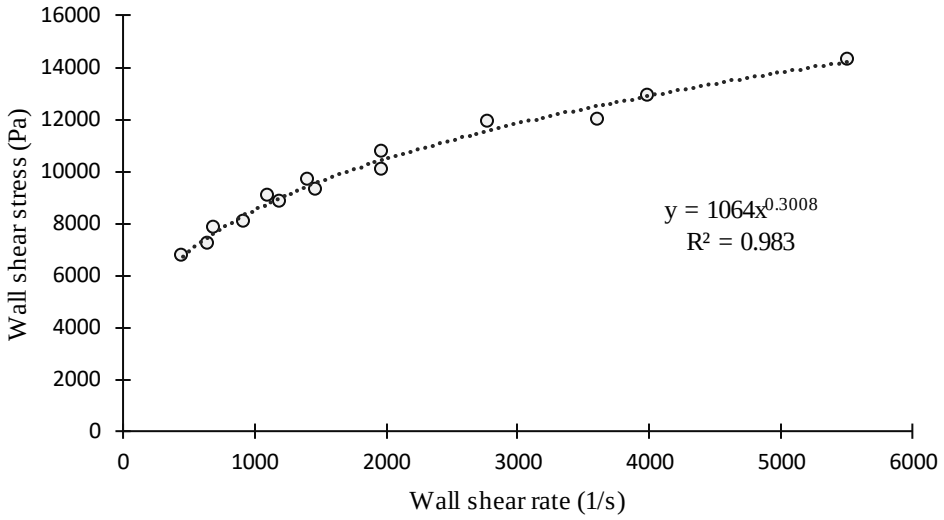

Figure 3-7 Overall flow curve for H = 2 mm and H = 4 mm

Moreover, the rheological properties of the investigated fluid are determined for Herschel–Bulkley from the Eq. 1-132 model using the experimental data from the channel with an aspect ratio of 0.1. The yield stress value is determined by the extrapolating flow curve at low shear rates to zero shear rate using a 3-degree polynomial equation and flow index and consistency are obtained by curve fitting method (Nguyen and Boger, 1992). The obtained yield stress value is 5000 Pa, consistency (K), and flow index (n) are 124 $Pa.s^n$ and 0.52, respectively.

In the case of the concentric annulus with high aspect ratios, the flow can be regarded as the flow between parallel plates as stated earlier. The validity of this assumption can be seen from figure 3-2 based on Eq. 3-11. As given in figure 3-2, for the aspect ratios greater than 0.1, the deviation between the parallel plate assumption and Kozicki's method is less than 10 % and for the aspect ratios greater than 0.6, this deviation is found less than 3 %.

The results reveal that the correlations of slit rheometer can be used for the concentric annuli with aspect ratios greater than 0.6. This assumption has been confirmed by Skocilas et al. (Skocilas et al.2016) experimentally by using a capillary annulus rheometer with an aspect ratio greater than 0.66. They measured rheological parameters of water solution of collagen at different concentrations and rheological properties of the collagen were determined for power-law and Herschel–Bulkley models. As seen from figure 3-2, parallel plate approximation is quite successful for this geometry and re-calculating rheological parameters for this geometry is not necessary and results can be seen in their work (Skocilas et al.2016). Moreover, those rheological data are used for the analysis of the rotor-stator mixer section.

2- A Method for Predicting the Friction Factor of Power-Law Fluids in non-Circular Channels

The friction factor is the one of most commonly investigated design parameters and various method has been suggested for the prediction of the friction factor of the laminar flow of power-law fluids through non-circular channels and conventionally used methods are shown in the previous chapter. In general, available methods are relatively complicated since defined Reynolds numbers are a function of the geometrical cross-section of the channels and mostly require more than one geometrical parameter except the method suggested by Delaplace (Ayas et al., 2019-a).

In this section, an alternative, simple method is proposed for the prediction of friction factor for the flow of power-law fluids in non-circular channels under the laminar flow regime. The simplification is achieved by using the Reynolds number suggested by Metzner and Reed and then a very simple correlation is introduced in order to express the relationship between friction factor and Reynolds number (Re_M) based on the assumption given in Eq. 3-6 in the previous section. Then this assumption is extended (Ayas et al., 2020-a) to other non-circular cross-sectional shapes (i.e. elliptical, concentric annuli, symmetrical L-shape, isosceles triangle, eccentric annuli, square duct with a central cylindrical core) shown in figure 3-8. Furthermore, a second alternative method is introduced for the prediction of friction factor of the flow of power-law fluids in non-circular channels with a narrow gap. The suggested method is compared with other methods analytically and by numerical methods.

Concentric annuli

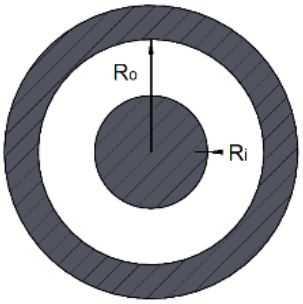

$$\kappa = \frac{R_i}{R_o}$$

Rectangular duct

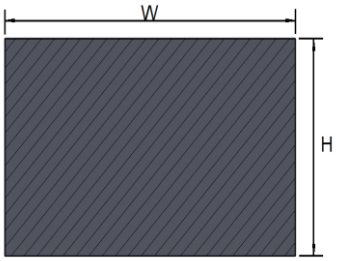

$$\kappa = H/W$$

Isosceles triangle

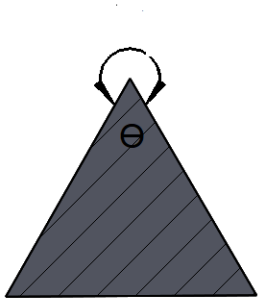

$$\kappa = \theta$$

Elliptical duct

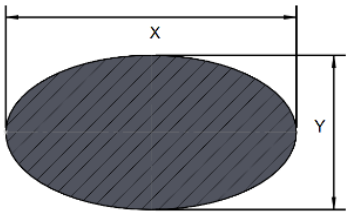

$$\kappa = Y/X$$

Symmetrical L-shape

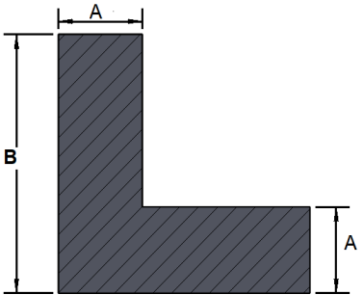

$$\kappa = A/B$$

Eccentric annulus

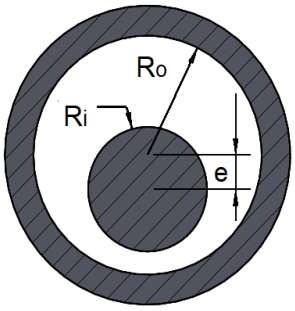

$$[\kappa = \frac{R_i}{R_o}; e^* = \frac{e}{R_o - R_i}]$$

Square duct with a centered cylindrical core

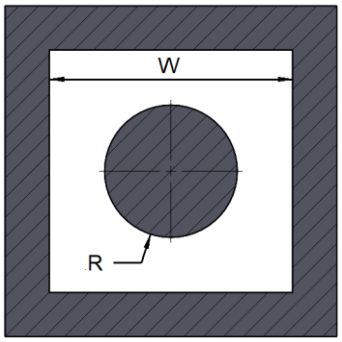

$$\kappa = 2R/W$$

Figure 3-8 Investigated cross-sectional geometries

2-1 Theory

The proposed simplified method is based on analyzing the relationship between the Reynolds number suggested by Metzner and Reed (Re_M) and by Kozicki (Re_G) for shear-thinning fluids (Ayas et al., 2019-a). The Reynolds number defined by Metzner and Reed (Re_M) for a rectangular channel can be written as

$$Re_M = \frac{\rho u^{2-n} {D_h}^n}{8^{n-1} K \left(\frac{3n+1}{4n}\right)^n} \tag{3-14}$$

The ratio of Re_M to Re_G is

$$\frac{Re_M}{Re_G} = \left(\frac{4(bn+a)}{3n+1}\right)^n \tag{3-15}$$

As seen, the ratio Re_M/Re_G is equal to the defined function ε given in Eq. 3-2. Using the linear approximation for ε given in Eq. 3-3 for the flow indexes in the range of $0 < n < 1$, the ratio Re_M/Re_G is equal to

$$\frac{Re_M}{Re_G} = Mn + N \tag{3-16}$$

It has been shown that the value of coefficient N is equal to 1 and the coefficient M is given in Eq. 3-5. Substituting Eq. 3-16 into Eq. 1-153, the final expression is given as follows

$$\lambda Re_M = (C-16)n + 16 \tag{3-17}$$

It can be seen that for the circular channel ($C = 16$) Eq 3-17 reduces to Eq. 1-151 and for $n = 1$ (Newtonian flow case) reduces to Eq. 1-150. It has been pointed out by Ayas et al. (Ayas et al. 2020-a) that obtained linear approximation of ε exists for cross-sectional shapes of elliptical, concentric annuli, symmetrical L-shape, eccentric annuli, square duct with a central cylindrical core (Ayas et al.,2020-a) which is shown in figure 3-9. Hence, Eq. 3-17 can be used to calculate the friction factor of fully developed laminar flow of power-law fluids through investigated geometries except for isosceles triangle cross-sections. Since the explicit linear relationship of ε does not exist for this geometrical shape. Besides, it has been indicated that the linearity of ε deteriorates for the geometries with narrow passages. For instance, the eccentric annuli of κ =0.9, regression analysis indicate that ε has linearity with an R^2 greater than 0.99 for $e^* = 0.1$, whereas, for $e^* = 0.9$, R^2 was found as 0.97.

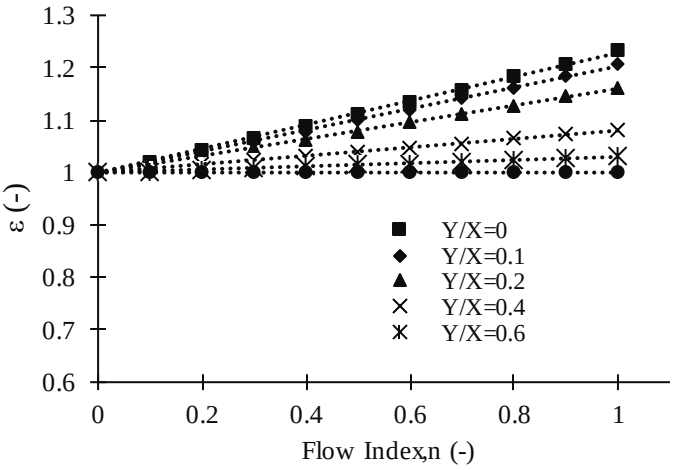

Elliptical

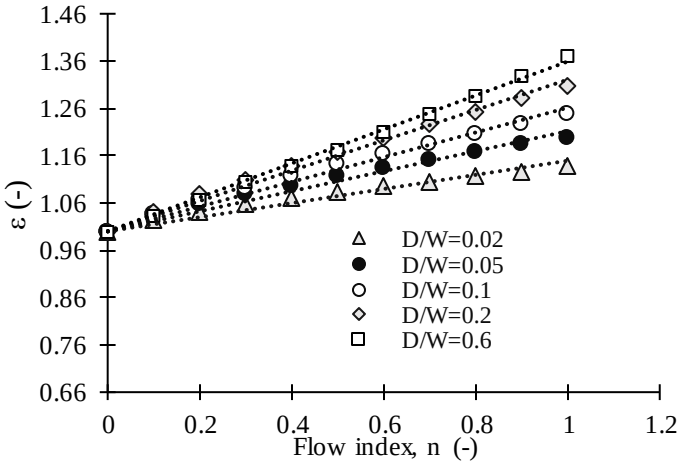

Square duct with a central cylindrical core

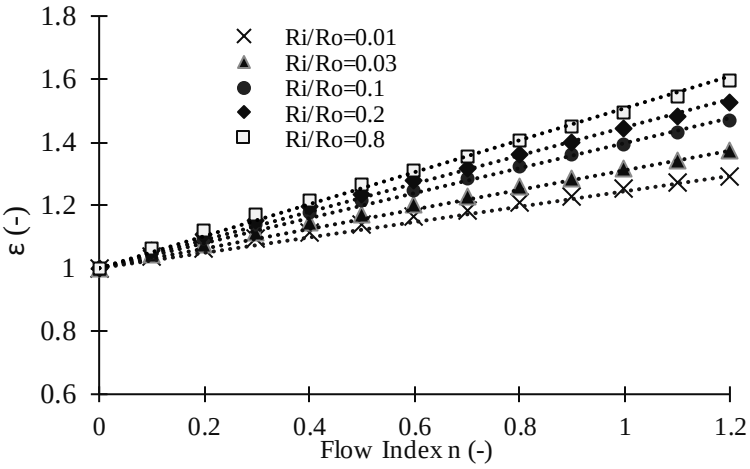

Concentric annuli

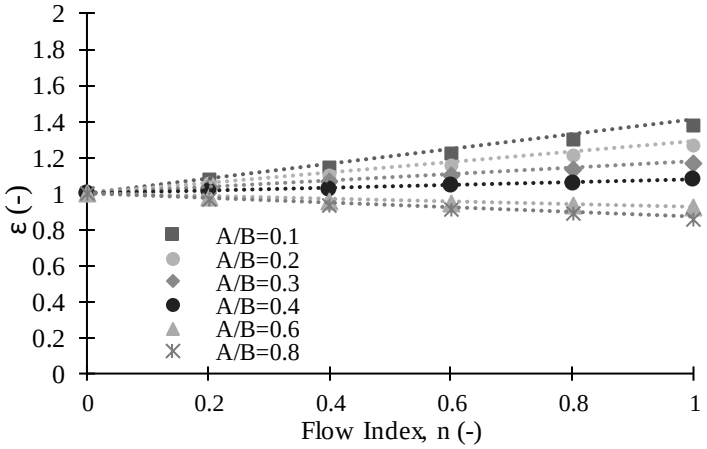

L-shape

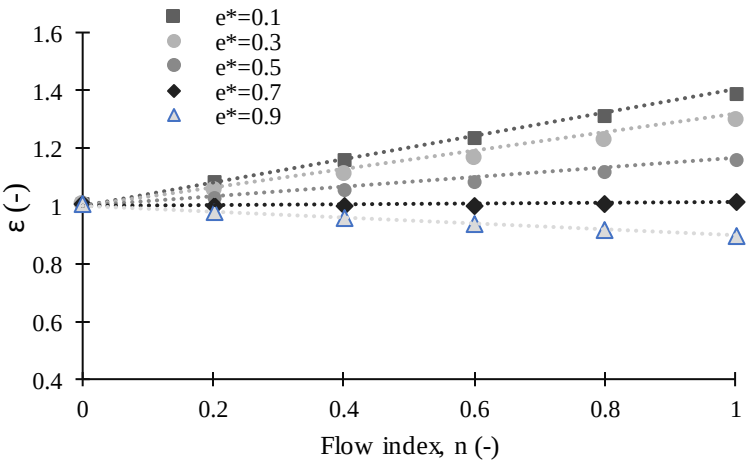

Eccentric annuli for κ = 0.1

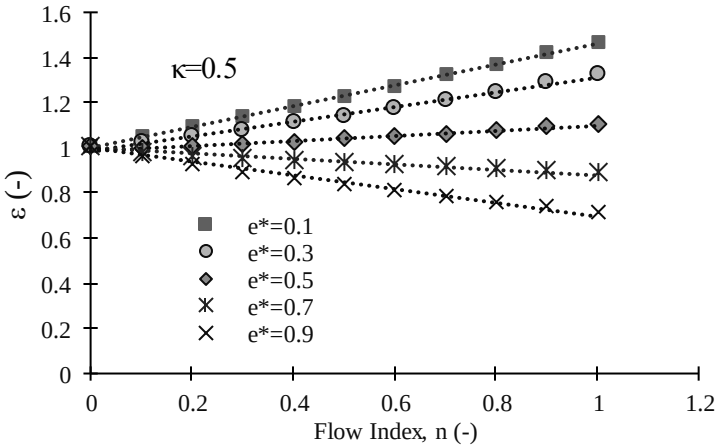

Eccentric annuli for κ = 0.5

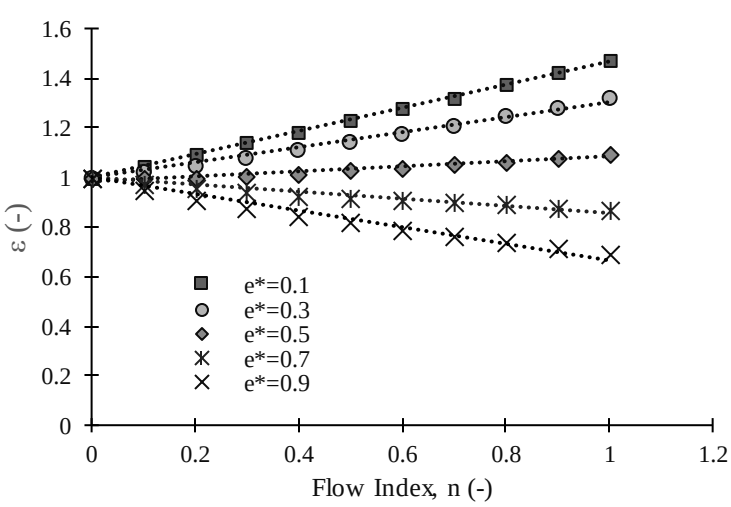

Eccentric annuli for $\kappa = 0.7$

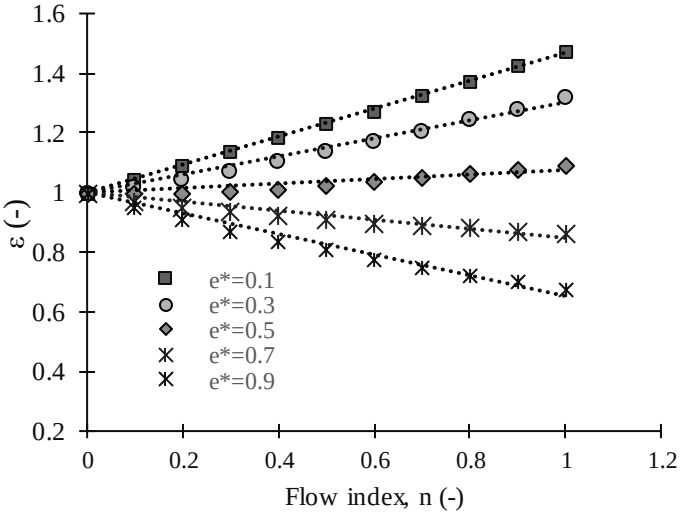

Eccentric annuli for $\kappa = 0.9$

Figure 3-9 The linear relation of ε and flow index (Ayas et al., 2020-a)

Alternatively, a different correlation can be obtained in terms of the parameters of parallel plates ($a = 0.5, b = 1$) especially for the channels with a narrow gap. It has been shown that Eq. 3-11 indicates approximately a linear relationship for the concentric annulus and rectangular channels and performing the same procedure for other non-circular sections, obtained approximate linear relationships are given in figure 3-10. It has been found that ε' indicates better linearity for the channels with narrow gaps. Besides, ε' shows a linear characteristic for the isosceles triangular which is not exist for the Eq. 3-15.

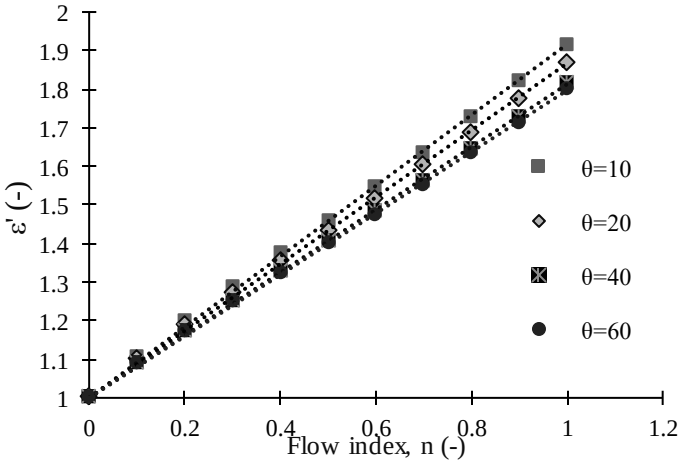

Isosceles triangle

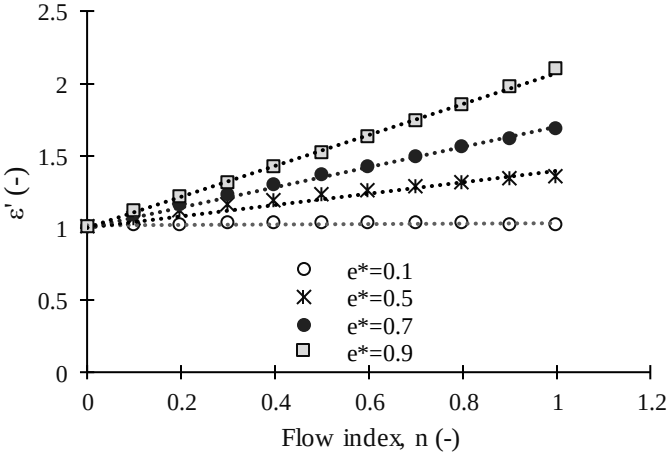

Eccentric annuli for $\kappa = 0.5$

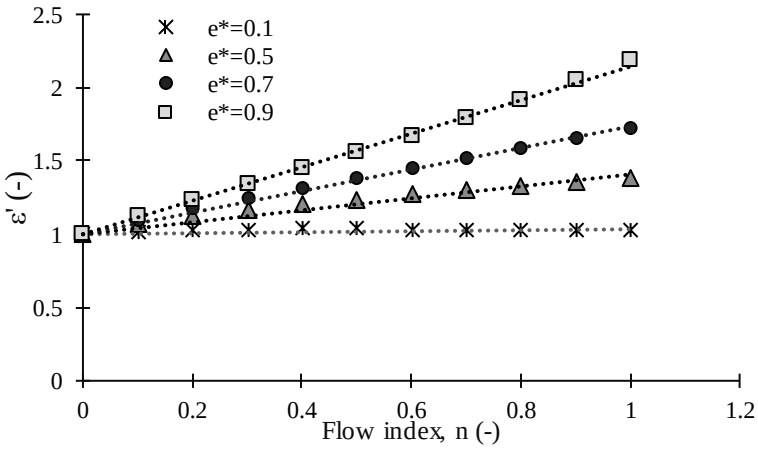

Eccentric annuli for $\kappa = 0.7$

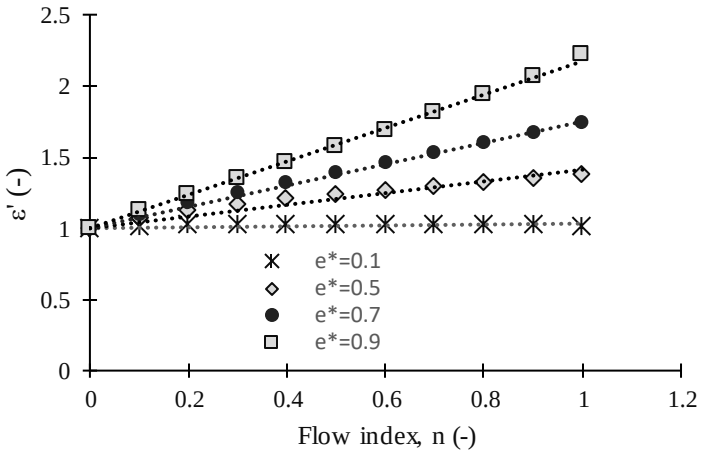

Eccentric annuli for $\kappa = 0.9$

Figure 3-10 The linear relation of ε' and flow index

Finally, substituting Eq. 3-11 into Eq. 1-153 with Eq. 3-12, the alternative correlation for the friction factor Reynolds relationship is

$$\lambda \mathrm{Re'_M} = \frac{16\mathrm{C}}{(24-\mathrm{C})\mathrm{n}+\mathrm{C}} \tag{3-18}$$

where $\mathrm{Re'_M}$ is

$$\mathrm{Re'_M} = \frac{\rho \bar{u}^{2-\mathrm{n}} \mathrm{D_h}^{\mathrm{n}}}{8^{\mathrm{n}-1}\mathrm{K}\left(1+\frac{1}{2\mathrm{n}}\right)^{\mathrm{n}}} \tag{3-19}$$

For the Newtonian flow case, Eq. 3-18 reduces to Eq. 1-150 and for $\mathrm{C} = 16$, Eq. 3-18 equal to Eq. 1-151. The critical value of Reynolds number ($\mathrm{Re_M}$) for the onset of the turbulent region has been considered as 2100 and the effect of the shape of cross-section on critical Reynolds number is neglected in this study.

2-1 Validation and discussion

The correlation proposed in Eq. 3-17 relies on the simplified α function in Eq. 3-6. Hence α function defined by Kozicki in Eq. 3-1 and the simplified α function in Eq. 3-6 is compared analytically for studied non-circular cross-sectional shapes for $0 < \mathrm{n} < 1$ (Ayas et al., 2020-a). Although non-existence of a linear characteristic of ε for isosceles triangular cross-section, the Eq. 3-6 was compared with Eq. 3-1 for isosceles triangles and the maximum deviation has been found less than 3.5 %. From the comparison, it follows that Eq. 3-17 can be used for isosceles triangular cross-sections.

The results of the comparison indicate that the deviation between the Eq. 3-1 and Eq. 3-6 are minimum for symmetrical L-shape and elliptical cross-sections and maximum deviation has been found less than 1 % for those geometries. The maximum deviation has been found less than 2 % for the concentric annulus and 2.5 % for the square duct with central cylindrical core and rectangular cross-sections.

In the case of the eccentric annulus, the difference between 3-1 and Eq. 3-6 is significantly affected by geometric ratios. The minimum deviation has been found for $\kappa = 0.1$ as less than 1 % and the deviation increases with increasing values of κ, so the maximum deviation has been found less than 4% for $\kappa = 0.9$. In general, the maximum deviations have been found for the flow indexes between $0.3 \leq n \leq 0.5$ for all geometries cross-sections.

The one-parameter model introduced by Delplace and Leuliet (Delplace and Leuliet, 1995) was derived from Kozicki's two-parameter model same as Eq. 3-17 with the aim of reducing two parameters to one parameter. Therefore, the comparison between the Eq. 3-17 and Delplace's method (Eq. 1-158) has been carried out analytically by comparing relative deviations of friction factors obtained by Eq. 3-17 and Delplace's method with Kozicki's method. In other words, Kozicki's method has been taken as a reference value. The relative deviation is defined as

$$\text{Deviation} = \frac{(\lambda_G - \lambda_i)}{\lambda_G} * 100 \tag{3-20}$$

In Eq. 3-20, λ_G indicates the friction factor obtained from Kozicki's method (Eq.1-153) and λ_i represents the friction factors for one-parameter models from Eq. 3-17 and Eq. 1-158 (my suggested method in Eq. 3-17 and Deplace's methods). The results of comparisons for the eccentric channel of $\kappa = 0.9$, square duct with a centered cylindrical core, and symmetrical L-shape are depicted in figure 3-12. As seen in figure 3-12, the deviations between Kozicki's method (λ_G) and proposed method in Eq. 3-17 (λ_M) increase with the increasing values of e* and maximum deviation has been found less than 4 % for e*=0.9. As seen from the figure, the variation between friction factor values from Kozicki's (λ_G) and Delplace's (λ_D) methods are found less than 4 % as well for the eccentric channel. Regarding the square duct with a centered cylindrical core and symmetrical L-shape suggested method in Eq. 3-17 provides 1% better results than Delplace's method.

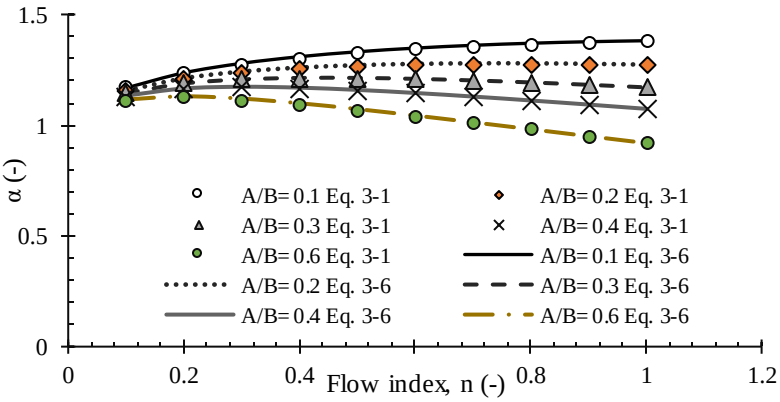

Symmetrical L-shape

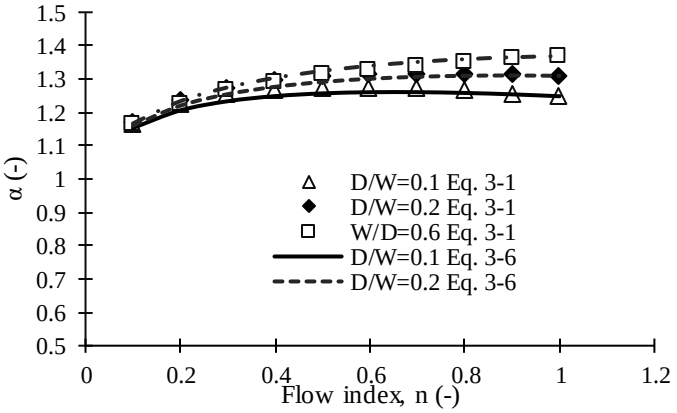

Square duct with a centered cylindrical core

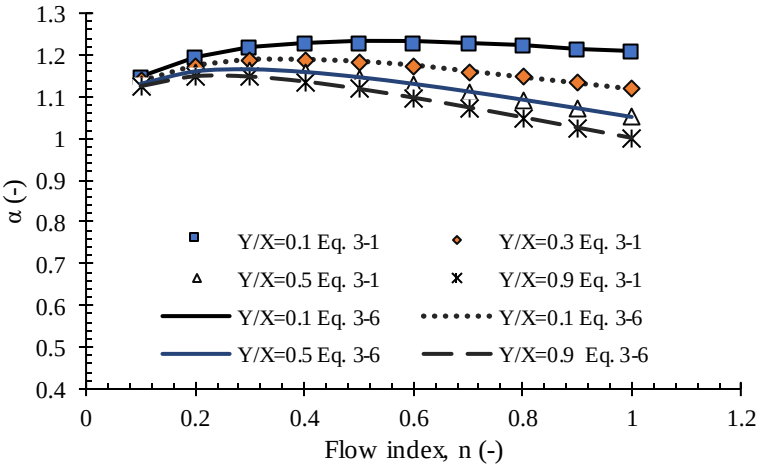

Elliptical

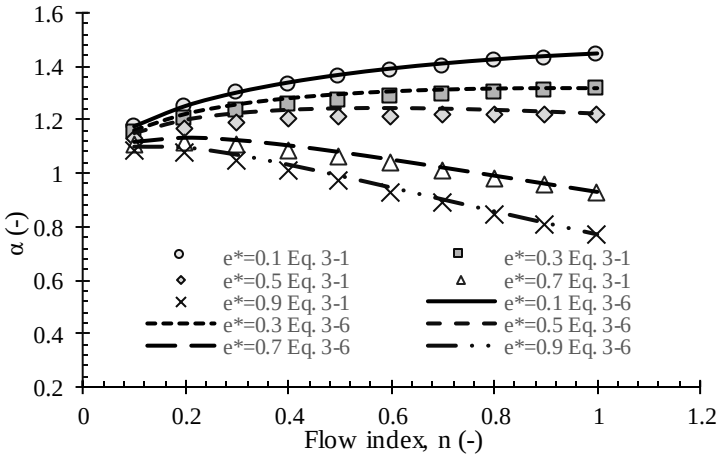

Eccentric annulus κ = 0.3

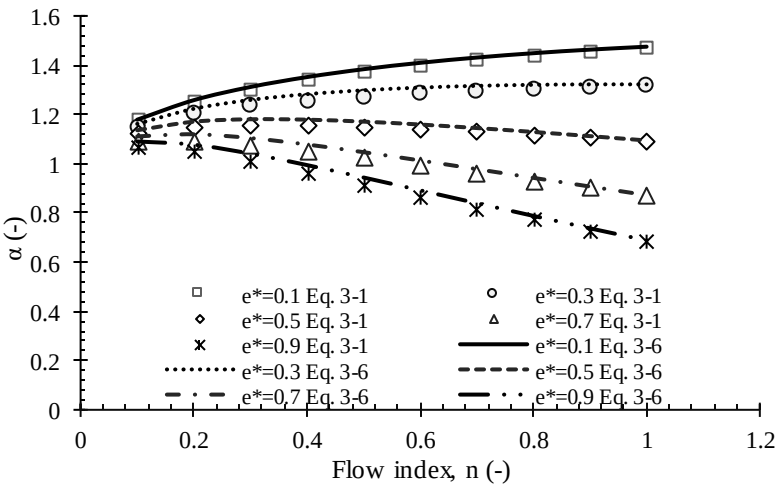

Eccentric annulus κ = 0.7

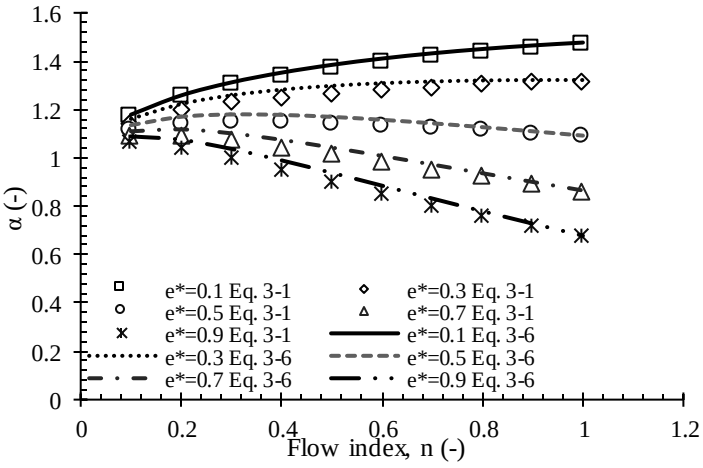

a- Eccentric annulus κ = 0.9

Figure 3-11 Comparison of α functions between Eq. 3-1 and Eq. 3-6

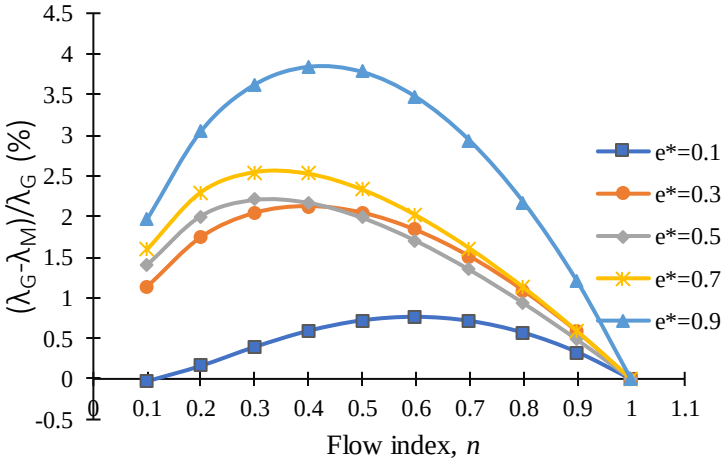

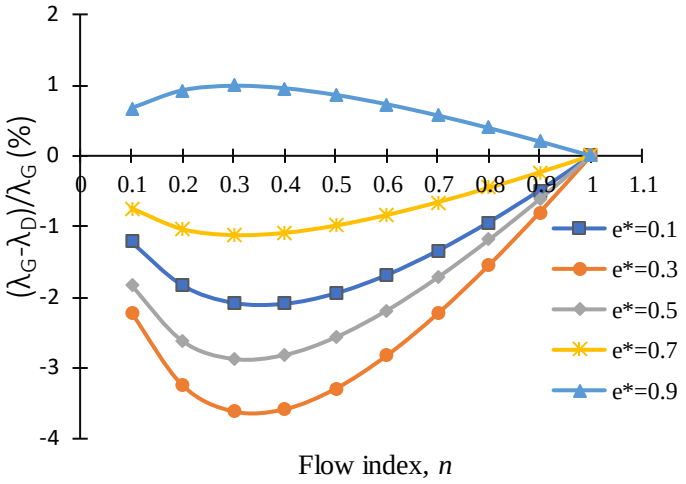

A- Eccentric channel of $\kappa = 0.9$

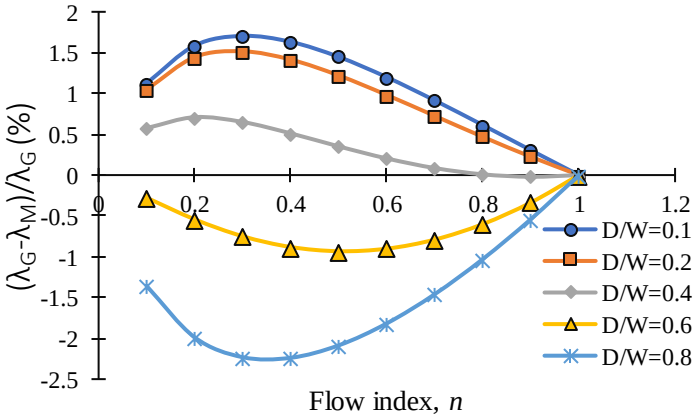

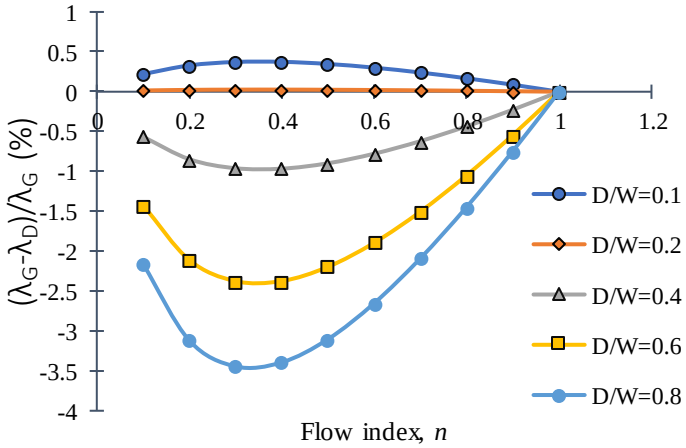

B- The square duct with a centered cylindrical core

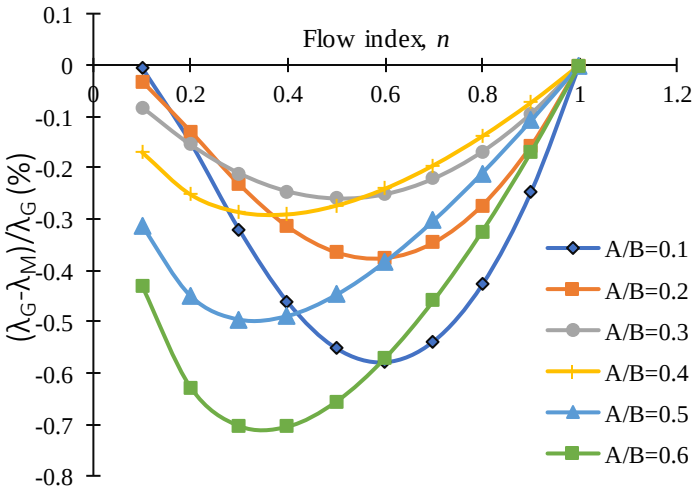

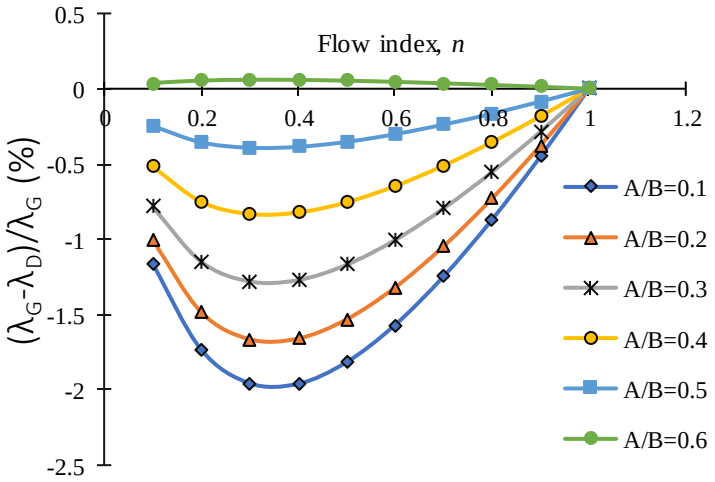

C- Symmetrical L-shape

Figure 3-12 Relative deviations of λ_M and λ_G with respect to Kozicki's method

From the results of comparisons, one can be concluded that Eq. 3-17 and Delplace's method leads to predict friction factors with similar accuracy. It should be indicated that even though Delplace's method and Eq. 3-17 are one-parameter models, there is a significant difference between the two methods. Firstly, the Reynolds number (Re_{DL}) suggested by Deplace is a strong function of geometrical parameter C, whereas in the provided method Re_M is independent of geometrical parameter C. Secondly, Delplace's method is valid only in the laminar flow case, but λ-Re_M relationship exists for turbulent flow of power-law fluids in non-circular cross-sections. Since our study is restricted by laminar flow, λ-Re_M relationship is not described for the turbulent regime in this study and more information can be found in the studies of Kozicki et al. (Kozicki et al., 1966) and Kostic and Hartnett (Kostic and Hartnett, 1984).

A further comparison is carried out by comparing the α in Eq. 3-1 and provided alternative α function given in Eq. 3-11 which are demonstrated in figure 3-13 for the isosceles triangle, elliptical channel, and eccentric annulus cross-sections. The alternative method gives better results for the channels with narrow gaps. The maximum deviation between Eq. 3-1 and Eq. 3-11 is found approximately 1% for isosceles triangles and concentric annulus and eccentric annulus of $\kappa = 0.9$ maximum deviation is less than 2.7 %. For the other geometries, Eq. 3-6 gives better results than Eq. 3-11. From the comparison, it can be deduced that the alternative approach given in Eq. 3-18 is more suitable for the prediction of friction factor of isosceles triangular cross-section and channels with narrow gaps.

Suggested correlation in Eq. 3-17 was also validated (Ayas et al., 2019-a) by experimental data in the literature (Hartnett et al., 1986). They carried out experiments using viscous shear-thinning fluid (aqueous solutions of polyacrylic acid, Carbopol 934 and 960) and viscoelastic fluid (aqueous solutions of polyacrylamide, Separan AP-273) through a square duct with a width (W) of 10 mm and with the length of 2500 mm and measurements were taken within the fully developed region of the channel. Only the results of Carbopol 960, $n = 0.64\text{-}0.65$ have been investigated from the experimental data. The comparison of experimental data and determined friction factor values using Eq. 3-18 are given in figure 3-14. Friction factor values obtained from the experimental data and Eq. 3-18 are in good agreement and the maximum deviation was found less than 4%.

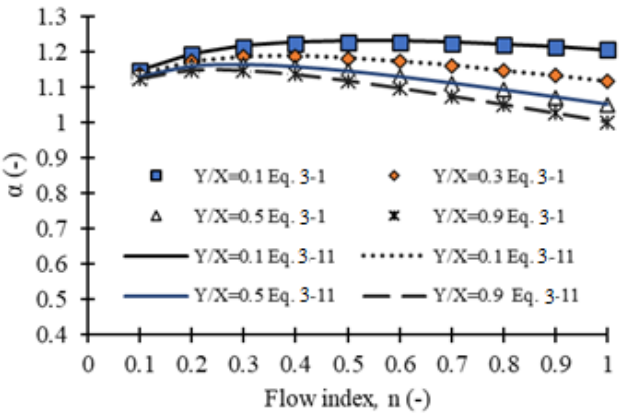

a- Elliptical duct

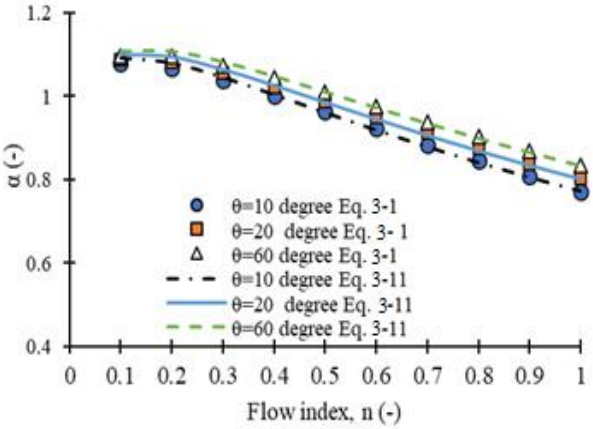

b- Isosceles triangles

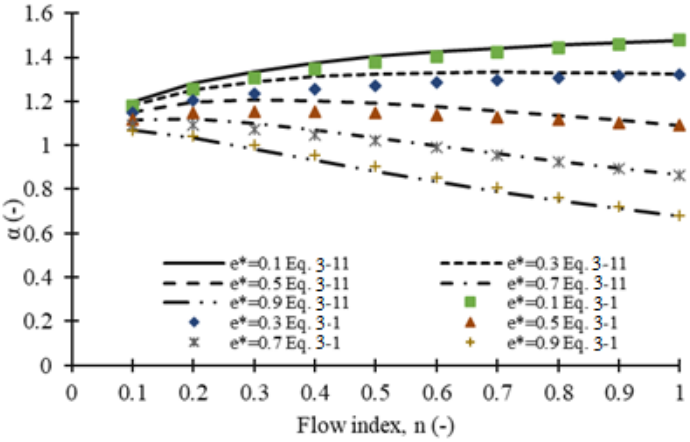

c- Eccentric annulus $\kappa = 0.9$

Figure 3-13 Comparison of α functions between Eq. 3-1 and Eq. 3-11

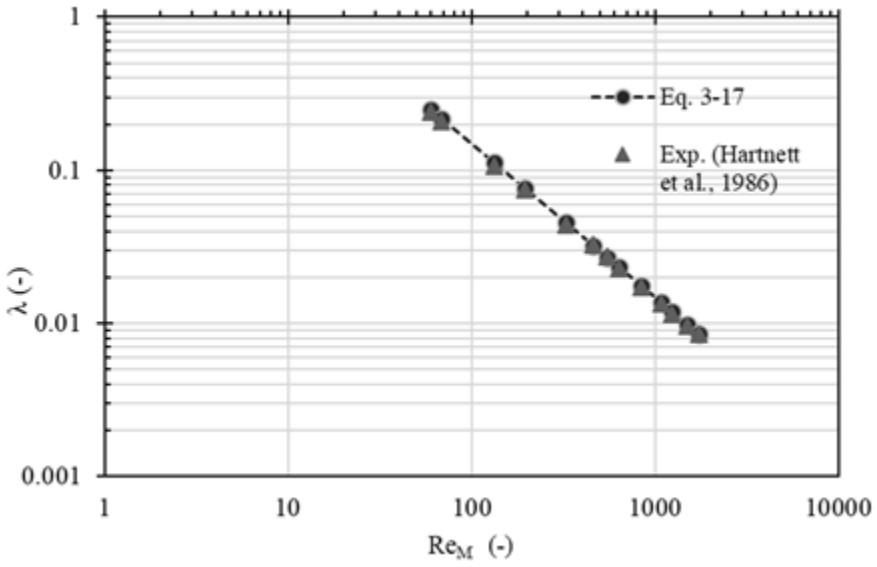

Figure 3-14 A comparison between Eq. 3-17 and experimental data (Hartnett et al., 1986)

Another experimental verification (Ayas et al., 2019-a) was carried out using experimental data obtained by Hartnett (Hartnett and Kostic, 1985). Experiments were conducted in a rectangular duct with a width (W) of 18 mm and a length of 6400 mm using an aqueous polyacrylamide solution. Results of experimental data o and calculated friction factor values according to Eq. 1-153 and Eq. 3-17 are shown in table 3-1. The maximum deviation has been found less than 9 % and calculated friction factor values from Eq. 1-153 and Eq. 3-17 are very close.

Table 3-1 Result of validation Eq. 3-17 and experimental data (Hartnett and Kostic,1985).

n	Re_M	Re_G	λ_{exp}	λ (Eq. 1-153)	λ (Eq. 3-17)
0.542	297	292.5	0.04951	0.0539	0.0538
0.563	616	606.3	0.02414	0.0260	0.0260
0.577	749	736.9	0.02177	0.0214	0.0214
0.59	1291	1269.7	0.01161	0.0124	0.0124
0.601	1715	1686.2	0.00875	0.0093	0.0093
0.616	2170	2132.6	0.00735	0.0074	0.0074

The other comparison has been carried out by performing numerical methods using ANSYS FLUENT 15 for, isosceles triangles, eccentric and concentric annulus, elliptical, symmetric L-shape, and a square duct with central cylindrical core cross-sections (Ayas et al., 2019-a; Ayas et al., 2020-a). The length of the created geometries was greater than $100D_h$ for each cross-section and 150000-200000 hexahedral mesh elements were used according to grid convergence index analysis (Celik et al., 2008). The grid convergence index analysis MATLAB codes are given for the eccentric channel of κ=0.7 by creating 40000, 120000 and 292000 mesh elements in appendix B. Simulations were carried out for isosceles triangle of 90^o and eccentric channel of κ=0.7, e $*$=0.9 for the flow indexes (n) of 0.4, 0.5, 0.6, 0.7, 0.8 and concentric annulus, elliptical, symmetric L-shape and a square duct with central cylindrical core cross-sections for $n = 0.5$ and various aspect ratios. The consistency (K) was chosen as 0.5 $Pa.s^n$ and the mean velocity was taken as 1.5 m/s for all simulations. For the boundary conditions, the inlet was chosen as velocity inlet, the outlet was selected as pressure outlet and the walls were taken stationary wall. For the solution method, the simple scheme was specified for pressure-velocity coupling and second-order pressure and momentum were selected for spatial discretization. The convergence criteria was taken for the continuity residual below 10^{-6}.

Numerically evaluated λRe_M values were compared with suggested methods and as well as conventionally used methods (Kozicki's and Delplace's methods), namely the results of simulations were taken as reference values. The results of the comparison are illustrated in figure 3-15.

For concentric annulus, Eq. 3-17 yields better results than Kozicki et al. and Delplace and Leuliet's methods, and maximum deviation remain less than 5% for those three methods. For elliptical and L-shape channels predicted λRe_M values by Kozicki et al.'s method and Eq. 3-17 are very close and Deplace and Leuliet's method yields less accurate results than the other two methods. For those two geometries, Eq. 3-17 ensures to predict friction factor less than 4% deviation.

For Square duct with a centered cylindrical core, Koziki's method gives better results than Eq. 3-17 and Delplace's method especially for the higher values of D/W. The difference between determined λRe_M values have been examined for $D/W = 0.8$ and different values of flow indexes. It was found that Eq. 3-17 gives better results than Delplace's method and the maximum deviation remains less than 5 % for the three methods.

The difference between evaluated λRe_M is checked for the eccentric channel of $\kappa = 0.7$ and $0.3 \leq e* \leq 0.9$. It was found that investigated three methods provide a successful result for $0.3 \leq e* \leq 0.5$, with a deviation of less than 4 % but for e*> 0.5, deviation increases as eccentricity increases for the three methods. Especially Eq. 3-17 yields unsatisfactory results with a deviation of 15 % for e*=0.9. Indeed, that is an expected result since as stated before, in terms of the isosceles triangle and eccentric annulus of high aspect ratios, Eq. 3-2 does not provide a good linear characteristic and Eq. 3-19 has been suggested for the prediction of the friction factor for those geometries based upon the parameters of the parallel plates.

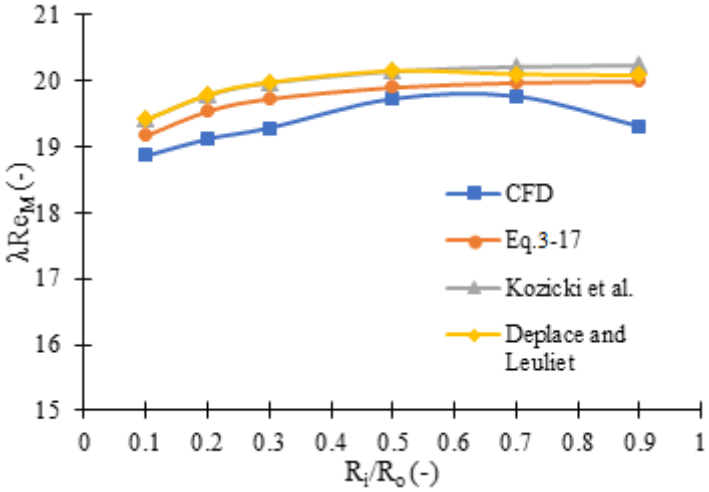

a- Concentric annulus, n=0.5 (-)

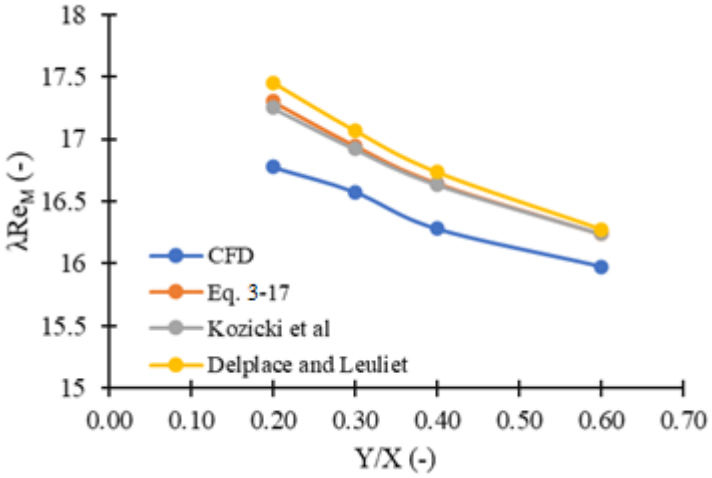

b- Elliptical channel, n=0.5 (-)

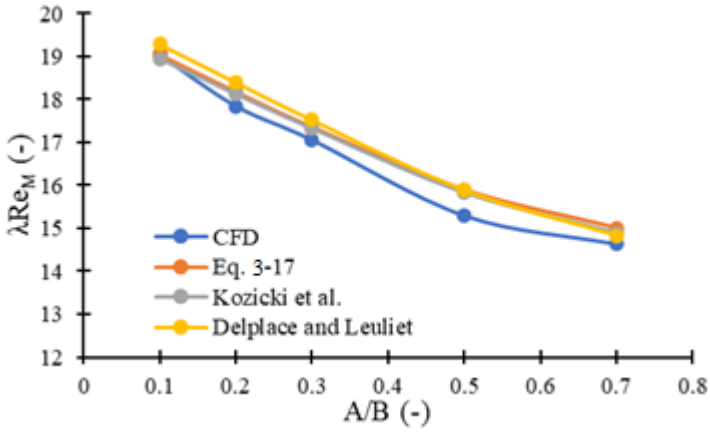

c- Symmetrical L-shape, n=0.5 (-)

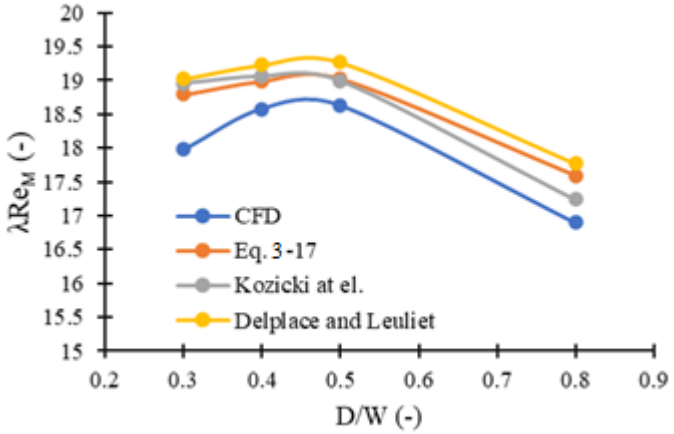

d- Square duct with a centered cylindrical core, n=0.5 (-)

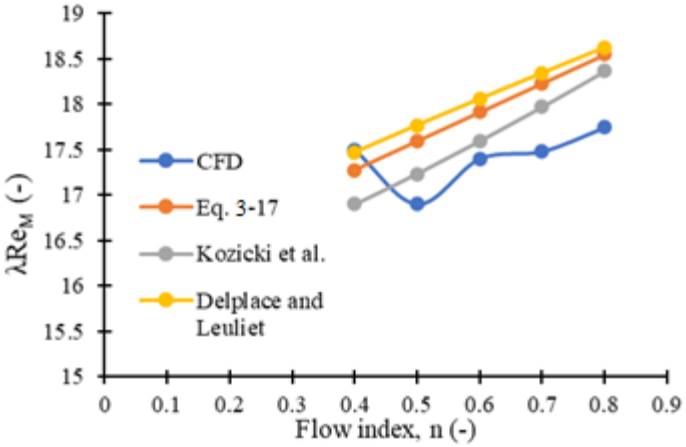

e- Square duct with a centered cylindrical core, D/W=0.8

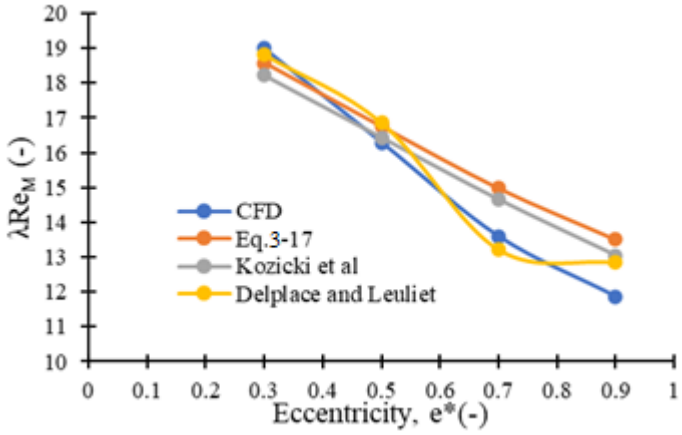

f- Eccentric channel κ=0.7

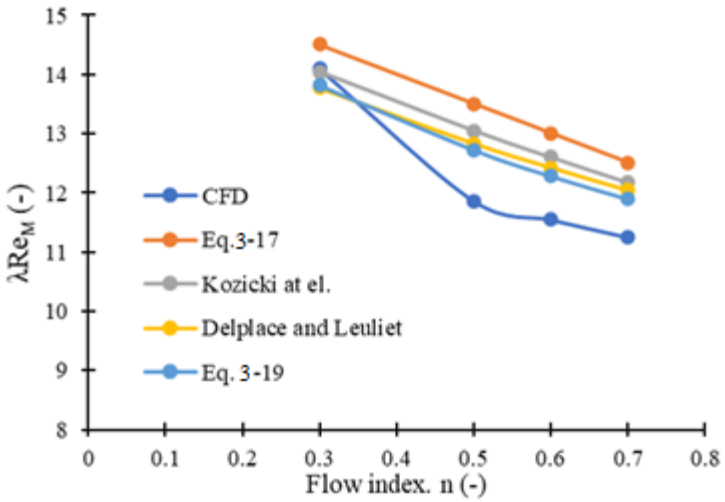

g- Eccentric channel κ=0.7, e*=0.9

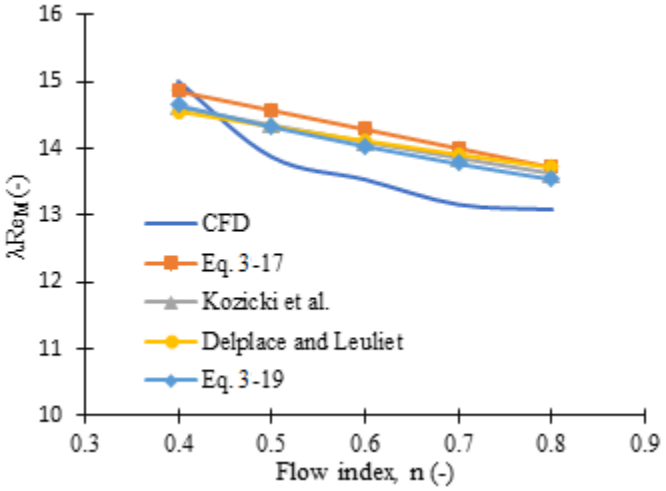

h- Isosceles triangle , θ=90°

Figure 3-15 The comparison between approximate models and results of simulations

Conclusion

In this section, rectangular channels of aspect ratios greater than 0.1 and concentric annulus were investigated for the measurement of shear viscosity of power-law fluids which is the most frequently used rheological model in the industry. An approximate one-parameter model was suggested for the determination of the wall shear rate for the power-law model. The provided correlation was validated using experimental data and compared with conventionally used methods. From the comparisons, it was deduced that provided correlation enables to determine shear viscosity of power-law fluids and it was proven that parallel plate approximation is quite successful and correlations of the slit rheometer can be used for the concentric annulus with high aspect ratios.

Then, the relationship between the friction factor and the Reynolds number was studied to obtain a practical, generalized method for laminar, fully developed power-law fluids in non-circular ducts using the Reynolds number suggested by Metzner–Reed, which can be calculated without regard to parameters dependent on aspect ratios. Then a very simple correlation was suggested to express λRe_M for fully developed, laminar flow of shear-thinning fluids for rapid engineering calculations. It was indicated that λRe_M depends on the flow index and the geometrical constant C, and the term λRe_M can be expressed by a very simple linear equation for shear-thinning fluids. The applicability of obtained correlation was examined with experimental data in the literature, analytically by comparison with the most widely used conventional method, and by numerical computations for the rectangular, concentric annulus, elliptical, symmetrical L-shape, square duct with a central cylindrical core, eccentric annulus, and isosceles

triangles cross-sectional geometries. It was found that the suggested correlation can be used successfully for the cross-sectional geometries of the rectangular, concentric annulus, symmetrical L-shape, square duct with a central cylindrical core, eccentric annulus with low aspect ratios, elliptical cross-sectional geometries for $0 < n < 1$ with a deviation of less than 5% and the model ensures slightly better results than other one parameter Delplace and Leuliet's method for those geometries. It should be noted that provided method in Eq. 3-17 is not as successful as other methods for the prediction of friction factor values for isosceles triangles and eccentric annulus of high aspect ratio. The alternative correlation based on Reynolds number Re'_M specified in Eq. 3-19 is giving better results for the prediction of friction factor for the geometries with narrow clearances and isosceles triangles, hence it is recommended to use infinite plate parameters for the channels with narrow gaps.

Chapter 4 -Agitation of viscoplastic fluid in in-line rotor-stator mixer

Mixing is one of the most frequently used unit operations in the industry which is carried out to reduce gradients of specified properties such as concentration, temperature, etc. Mixing of liquids is generally achieved in mechanically agitated vessels. Mixing of non-Newtonian fluids commonly employed in the polymer, food, and pharmaceutical industries for the preparation of dispersions, homogenization, etc. and agitation of non-Newtonian fluids mostly carried out under the laminar flow regime due to their high viscosities (Paul et al., 2004; Doran, 2012).

The mixing performance in the laminar flow regime is considered poor since fluid flow in the mixing environment is dominated by viscous forces and agitation of such fluids results in high power consumption (Paul et al., 2004). Especially, agitation of viscoplastic fluids gives rise to the formation of the well-mixed region (cavern) in the vicinity of the impeller, and dead zones are generated next to the wall of the mixing vessel and which leads to poor mixing. In order to obtain efficient mixing, bulk flow (shear rate) should be provided within the large part of the mixing vessel since the distribution of shear rate is regarded as one of the key parameters for the mixing efficiency (Archard et al., 2006). Hence, close clearance impellers are preferred for the mixing of non-Newtonian fluids to obtain efficient mixing.

However, it should be noted that agitated vessels stirred with close clearance impellers may not provide an effective mixing performance for the viscoplastic fluids possessing high yield stress and can lead to a decrease in the mixing quality. In such cases, a more efficient mixing operation can be achieved by agitation viscoplastic fluids in rotor-stator mixers. Those mixers provide a shorter processing time than conventionally used stirred vessels with close clearance impellers which is more desirable for industrial purposes.

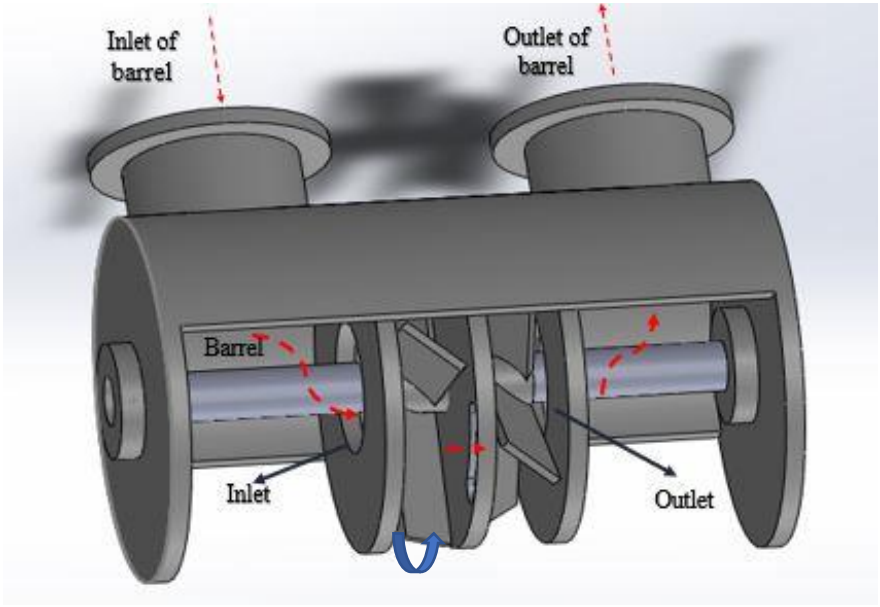

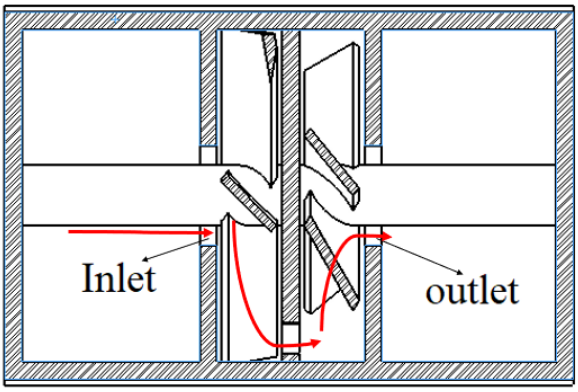

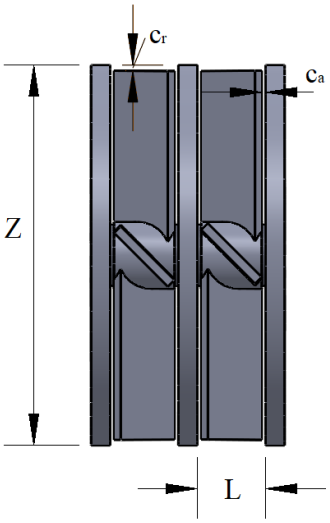

Figure 4-1 Description of the in-line rotor-stator (Flow direction is indicated by red lines)

1- Description of designed in-line rotor-stator mixer

The design of the studied mixer (see figure 4-1) was created by the research and development team of the Process engineering department by Dr. Jan Skocilas Ing. Dr. Jiri Moravec Ing., Dr. Lukas Kratky, and Prof. Dr. Tomas Jirout Ing and detailed design of the mixer is given in Appendix E. The newly designed in-line rotor-stator mixer consists of two serial mixing heads which are installed in a cylindrical barrel and two impellers were mounted on the same shaft. Stators have a cylindrical shape and the lateral surface of the stator is the wall of the barrel. For the designed mixer, the radial clearance (c_r) between the rotor and stator is 3 mm constant. The flat surfaces of the cylindrical stator are composed of three partitioning discs and those discs are movable, hence the axial clearances (c_a) between rotor and stator can be adjusted according to requirements of the process. The agitation of the mixer is provided by 45° four-pitch blade impellers with a diameter (D) of 194 mm and the diameter of the stator (Z) is 200 mm. The inlet and outlet of the mixer are hollow disks and the shaft of the mixer is located at the center of the disk. The passage of fluid from one mixing head to the other one is enabled by four slots which are located at the edge of the disk. (Ayas et al., 2019-c). Hence, in the designed mixer, it was aimed to generate flow is mainly between the rotor and stator in the axial direction. In this chapter energy consumption, flow, and shear rate profile of designed in-line rotor-stator mixers are investigated experimentally and numerically. Power consumption of the rotor-stator mixer is measured using yield shear-thinning fluid experimentally and obtained power consumption values are validated using numerical methods by ANSYS FLUENT. Then, power consumption, flow field, velocity profile, and shear profile will be studied using numerical methods for Newtonian, power-law, and Herschel–Bulkley model. Mixing Reynolds number-power number relationship and scale-up criteria are discussed.

2- Theory

In terms of in-line rotor-stator mixers, the generated power is the sum of power created by impellers (rotor) and power of flowing fluid from the inlet and to the outlet of the mixer (Kowalski, 2009).

$$P_{total} = P_R + P_f \tag{4-1}$$

In Eq. 4-1, The power generated by the rotor (P_R) and the power of flowing fluid is given as (Vial et al. 2015)

$$P_f = \Delta p \dot{V} \tag{4-2}$$

Dividing each term Eq. 4-1 by $\rho N^3 D^5$, Eq. 4-1 is stated in the dimensionless form as (Cooke et al., 2012).

$$\frac{P_{total}}{\rho N^3 D^5} = \frac{P_R}{\rho N^3 D^5} + \frac{\Delta p \dot{V}}{\rho N^3 D^5} \quad (4\text{-}3)$$

Hence, the total power number for an in-line rotor-stator mixer is

$$Po = Po_R + kN_Q \quad (4\text{-}4)$$

Where k is power flow constant and N_Q is the flow number

$$N_Q = \frac{\dot{V}}{ND^3} \quad (4\text{-}5)$$

According to Eq. 4-4, the total power of an in-line rotor-stator mixer is the sum of the power number of rotor and power number arising from the fluid flow between inlet and outlet sections of the mixer(Cooke et al., 2012) and it was suggested that the effect of fluid flow on the power consumption of a rotor-stator mixer in a laminar flow regime is neglected. Namely, in the laminar mixing of an in-line mixer, $Po = Po_R$. Power number analysis can be extended for viscoplastic fluids to obtain a simplified correlation. In the case of Bingham fluids, Hedstrom number for the mixing case is given as follows (Bertrand et al.,1996)

$$He = \frac{\rho \tau_0 D^2}{\mu^2} \quad (4\text{-}6)$$

Introducing effective shear rate, Eq. 4-6 can be stated as

$$He = \frac{\rho \tau_0 D^2}{(K(k_s N)^{n-1})^2} \quad (4\text{-}7)$$

and using Reynolds number (Re_{MO}) suggested by Metzner and Otto, Bingham number is described as

$$Bi = \frac{He}{Re_{MO}} = \frac{\tau_0}{K(k_s)^{n-1}(N)^n} \quad (4\text{-}8)$$

Using Bi and Re_{MO}, Eq. 1-183 can be stated alternatively as follows.

$$PoRe_{MO} = \frac{C}{k_s} Bi + C \quad (4\text{-}9)$$

Dividing both sides of Eq. 4-9 by $(k_s)^{n-1}$, the Eq. 4-9 is expressed by Re_{RN} such that

$$PoRe_{RN} = \frac{C}{k_s} Bi^* + C(k_s)^{n-1} \quad (4\text{-}10)$$

where Bi^* is (Archard et al., 2006)

$$Bi^* = \frac{\tau_0}{K(N)^n} \quad (4\text{-}11)$$

The suggested expression Eq. 4-10 is quite convenient for the evaluation of k_s. The left-hand side of Eq. 4-10 is independent of geometrical parameters and on the right-hand side Bi^* is the function of rheological parameters and rotational speed. According to Eq. 4-10, the plot of $PoRe_{RN}$ versus Bi^* for the same fluid at different velocities should be linear and the slope of that curve is equal to C/k_s. Hence, k_s the value of the mixer can be calculated from the slope of the linear curve easily if the C value is known.

On the other hand, power number according to Eq. 4-10 can be expressed as follows (Ayas et al., 2020-b)

$$Po_R = Po_Y + Po_S \tag{4-12}$$

where Po_Y indicates the power number for overcome yield stress and Po_S represents the power number of the sheared flow and can be defined by the following equation.

$$Po_Y = \frac{CBi^*}{Re_{RN}k_s} \tag{4-13}$$

$$Po_S = \frac{C(k_s)^{n-1}}{Re_{RN}} \tag{4-14}$$

Hence, substituting Eq. 4-12 to Eq. 4-1, the power number can be rewritten for yield stress fluids as follows

$$P_o = Po_Y + Po_S + kN_Q \tag{4-15}$$

For an efficient mixing process of yield-shear thinning fluid, Po_S should be high enough since mixing efficiency is proportional to the created shear in the mixer in the laminar flow regime (Ayas et al., 2020-b). Hence, mixing process efficiency in the laminar regime can be defined as

$$X = \frac{Po_S}{Po_Y + Po_S} = \frac{Po_S}{Po} \tag{4-16}$$

From Eq.4-16, it is obvious that the efficiency increases with rotor speed and Metzner-Otto coefficient and decreases by yield stress.

3- Experiment

The investigated in-line rotor-stator mixer has been designed with the aim of preparation of homogeneous dispersion of dye in collagen matter which is an extremely viscous material. Several experiments were conducted to investigate the concentration distribution of the dye in collagen, mixing efficiency, and determination of optimum operating conditions for the mixer. Moreover, the pressure drop of the fluid between the inlet and outlet sections and temperature increase due to viscous heat dissipation, and the

power consumption of the investigated mixer was measured. All measurements were taken for the axial clearances of 1 mm, 2 mm, and 3 mm and rotor speeds of 150 RPM, 300 RPM, and 500 RPM. The water solution of the bovine collagen with a mass fraction of 7.7 % was used as a test material. The rheological properties of the test fluid were examined by a capillary rheometer. It was found that the fluid exhibits a yield shear-thinning characteristic and obtained rheological properties are $\tau_0 = 4600$ Pa, K=420 Pa.s^n , n=0.34 (Skočilas et al., 2016).

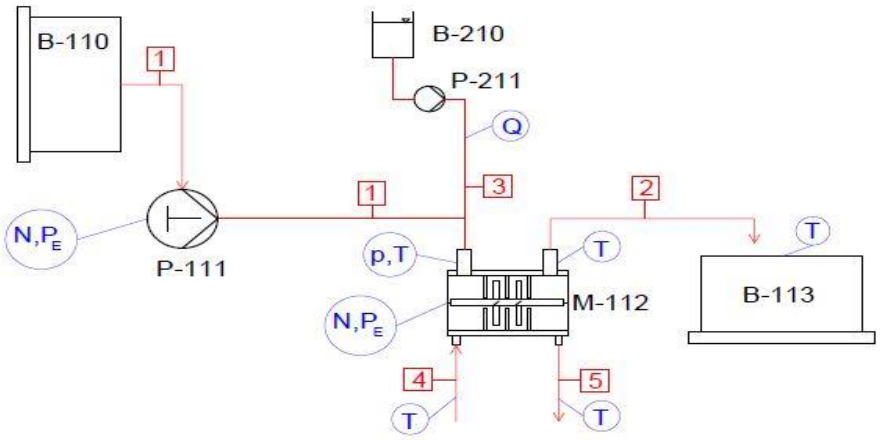

A-Experimental set-up

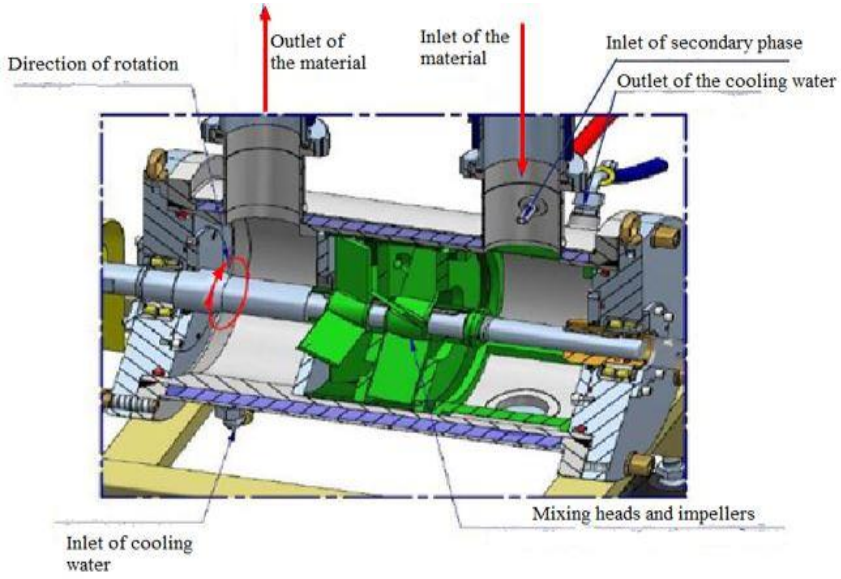

B- Description of the investigated mixer

Figure 4-2 (A) Experimental set-up, Measured quantities: N-rotational speed, p-pressure, T-temperature, P-power; (B) Description of the mixer

The experimental set-up is depicted in figure 4-2-A. Due to the high yield stress value of the collagen, a positive displacement pump (P-111) was used to discharge the material from the reservoir B-110 and feed the mixer. The dye was added to collaged at the inlet of the barrel by pump P-211 from reservoir B-210. In order to obtain a uniform concentration distribution of dye in collagen, processed fluids have passed through the mixer three times. The dye was added to collagen in the first pass and then the mixture re-cycled 2 times more without adding dye. The collagen is a biomaterial and sensitive to temperature and the structure of the material can be deformed due to viscous heat dissipation arising from the rotation of the rotor. Therefore, the temperature increase of the mixed materials was measured at the inlet and outlet of the barrels (streams 3 and 4), and keeping the temperature of the materials in a certain range, mixing heads were covered by the cooling jacket. Iced water was used as a coolant. The pressure of fluid was measured by a diaphragm manometer with a maximum capacity of 40 bar which is located at the inlet of the barrel and at the outlet of the barrel the pressure of the fluid was considered as zero-gauge pressure. Rotation of impellers was provided by an electric motor with a maximum power output of 5.5 kW and a maximum speed of 1000 RPM.

The optimum flow rate of the collagen was determined by measuring temperature increment due to viscous heat dissipation for the mass flow rates of 2 kg/min, 4 kg/min, and 6 kg/min, and the results are shown in figure 4-3. As seen from the figures, the lowest temperature variation collagen was acquired for the flow rate of 6 kg/min and this value is more suitable in terms of the economical aspect. Consequently, experiments of the investigated rotor-stator mixer were carried out for the mass flow rate of 6 kg/min (0.1 kg/s). The results of temperature growth are discussed in the following section in detail.

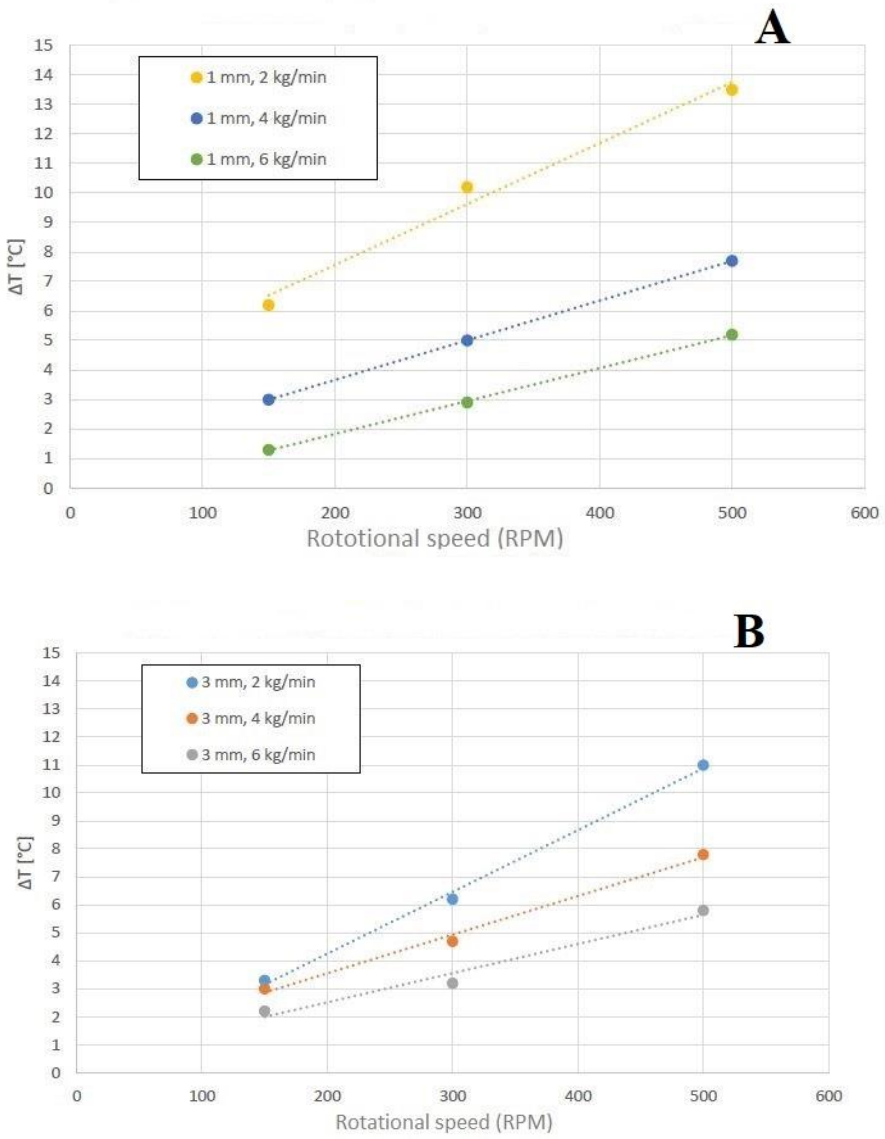

Figure 4-3 Deviation of temperature due to viscous energy dissipation for (A) c_a=1 mm and c_a=3 mm

It should be noted that in this work, the result of the concentration distribution of dye in the collagen was not considered due to missing parameters of the investigated materials such as interfacial tension. Therefore, the results of experimental results and further calculations are carried out for the collagen only, and the result of temperature variation, pressure drop, and power consumption are discussed in the following sections. The result of the concentration distribution of die in collagen is not given in this study.

4- Simulation

Three-dimensional numerical simulations (Ayas et al., 2020-b) were carried out in order to verify experimental data, for the determination of the power draw coefficient C and analyzing velocity and shear profile within the mixing heads. In this section, created fluid domain, mesh structure, mesh sensitivity analysis, and simulation strategies are discussed.

The fluid domain of the investigated mixer has been created in the Ansys design modeler tool which is shown in figure 4-4. In order to apply specific mesh strategies, mixing heads have been sliced from the entire domain to generate a convenient mesh structure, and to avoid interfaces, the sliced volume has been combined. Also, the geometrical domain of the moving reference frame is created in this section.

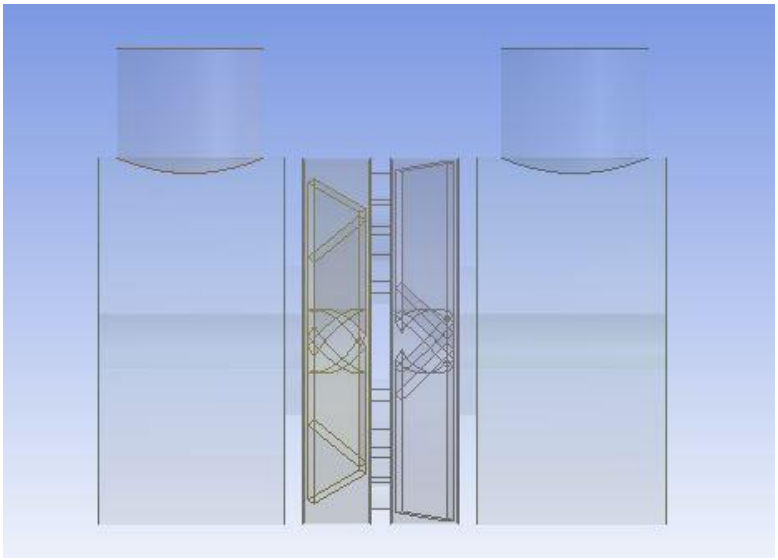

Figure 4-4 Fluid domain of the numerical simulation

After creating the fluid domain, the next step is the generation of grids (meshes) in the ANSYS workbench. The geometry of the heads is not uniform, thus unstructured meshes were created. Especially, to capture velocity and shear profile successfully, fine tetrahedral mesh elements were created at the vicinity of the impeller, and clearance between rotor and stator and coarse meshes have been preferred for the barrel sections.

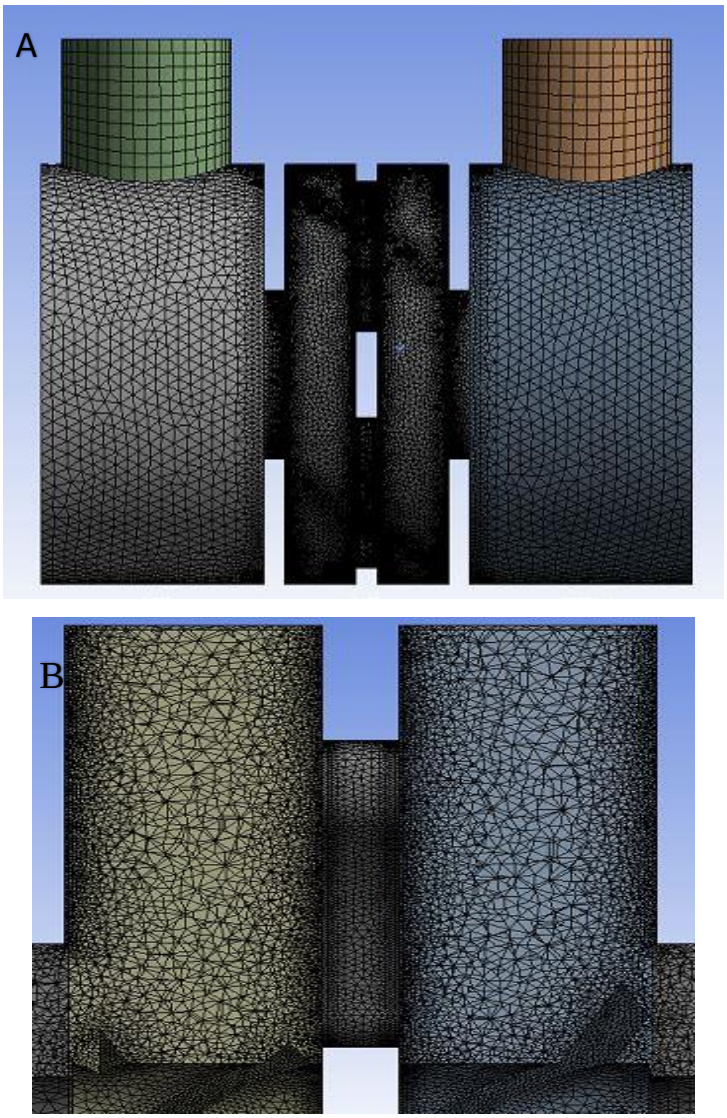

Figure 4-5 Created grids for the simulations (A)- overall view (B)- Cross-sectional view

The different number of mesh elements have been created based on altering mesh size between rotor and stator depending upon the axial clearance of the investigated geometries. The Created mesh structures for $c_a = 1$ mm is shown in figure 4-5.

The simulation of investigated in-line rotor-stator mixer is carried out for the steady-state flow case, under the laminar flow regime and isothermal flow case. Fluent provides the viscosity functions of non-Newtonian fluids, hence simulations have been performed for the Herschel–Bulkley, power-law models, and as well as Newtonian flow case. Simulations were carried out for the Herschel–Bulkley model with the rotor speed of 150, 300, and 500 RPM for $c_a = 1$ and $c_a = 3$ mm and 500 RPM for $c_a = 2$ mm. For the Newtonian case simulations, the viscosity of the fluid was chosen as 10 Pa.s, and simulations were

performed for the rotor speed ranged from 30 RPM to 150 RPM. For the power-law fluids, simulation is conducted for the rotor speed of 60 RPM and using power-law fluids with flow indexes between 0.2 and 0.6 (Ayas et al., 2020-b).

The rotation of the rotor (impeller) has been modeled using the multiple reference frame (MRF) method. In the MRF approach, the domain of the fluid is divided into the moving reference frame and stationary zones shown in figure 4-6. Two cylindrical rotating frames have been created within the mixing heads and the radius of the rotating zones has been considered as the mean value of the radius of the impellers and stator. The clearance between the flat surface of the wall and the rotating zone has been taken as $c_a/2$ and conformal interphases have been created between the moving reference frame and stationary zones.

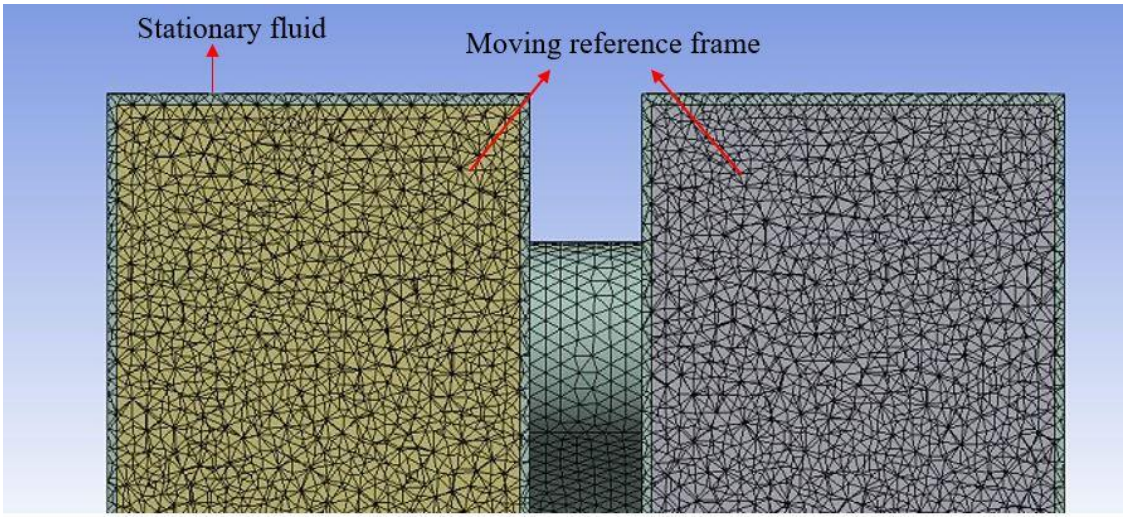

Figure 4-6 Created rotary and stationary bodies for the MRF method

Regarding boundary conditions, the inlet of the barrel is assigned as a mass flow inlet, and the outlet of the barrel is pressure outlet. Shaft and impellers are selected as moving wall. It has been assumed that the effect of wall-slip is negligible. The SIMPLE scheme was applied for the pressure-velocity coupling and, second-order pressure and second-order upwind velocity schemes were utilized as stated before. Convergence criteria for the continuity is below the 10^{-9} for the Herschel–Bulkley model, 10^{-6} for the power-law model, and Newtonian case. In each simulation, standard initialization has been applied with absolute reference frame.

The rotor-stator mixer with an axial clearance of 1 mm should have a greater number of mesh elements than the other investigated two geometrical configurations. Therefore, a grid sensitivity test has been

carried out concerning this geometrical configuration and so 1.1, 2.6 and 11 million mesh elements have been created. Simulations have been implemented for N= 500 rpm and according to investigated fluid in the experiment (Herschel–Bulkley model). Numerically calculated values power and the corresponding number of mesh are given in figure 4-7.

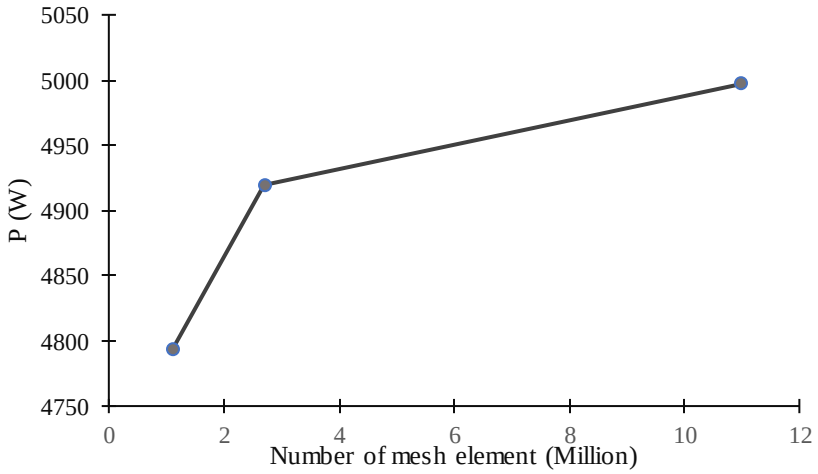

Figure 4-7 Number of grids vs numerical results

The extrapolated value of power consumption has been determined through MATLAB codes (see Appendix B). Extrapolated power consumption value has been found as 5032 W for the infinite number of mesh elements and the GCI index has been determined 0.9 % for the finest number of mesh elements and 3.5 % for middle size mesh elements. Therefore, 2.8 million number of mesh element is considered for the numerical calculation of power consumption.

5- Result and Discussions

In this section, firstly the result of experimental data is assessed, and the results of experimental data are discussed. Then, the experimentally and numerically determined power values are compared and the required design parameters (power-draw constant, Metzner-Otto coefficient) are acquired. Finally, the effect of impeller speed and geometrical ratios on power consumption and flow profile in the mixer are discussed.

5-1 Results of experiment and simulations

The experimental data were analyzed to choose optimum operation conditions for the mixing process for the given material and the determination of the design parameters of the investigated rotor-stator mixer. From the results of measured temperature increments due to dissipative heating (viscous heating) given in figure 4-3, one can be concluded that the flow rate of the fluid and rotational speed of the rotor has a

significant effect on temperature growth. The experimentally obtained temperature gradient is inversely proportional to the flow rate as expected from the enthalpy balance and temperature growth of the fluid is predominantly influenced by the rotational speed of the impellers. Axial clearance does not have a significant effect on the temperature rise.

The results of measured power consumption values are given in figure 4-8. As seen from the figure, the power consumption of the mixer varies almost linearly with the rotational speed of the rotor due to the effect of the high yield stress value of the fluid and c_a does not have a significant effect on the power draw.

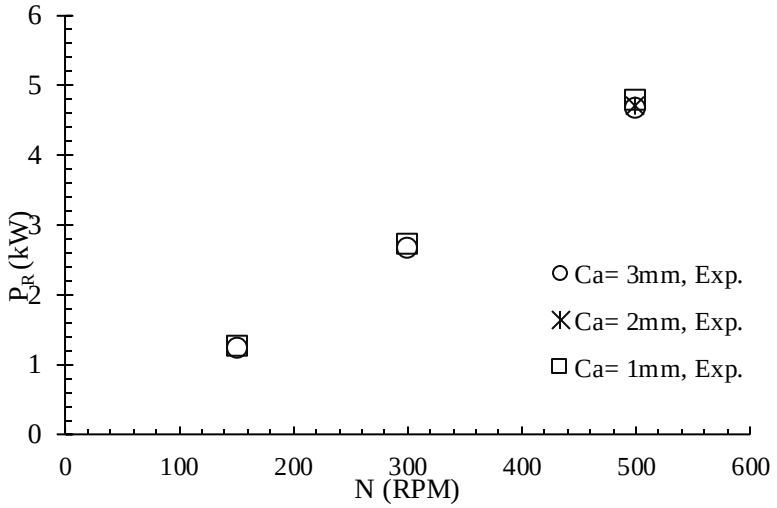

Figure 4-8 Experimentally measured power values

The measured pressure drop between inlet and outlet sections of the barrel and corresponding flow power (P_{flow}) values from the Eq. 4-2 is given in table 4-1

Table 4-1 Result of experimentally obtained pressure drop and P_f values

c_a mm	Mass flow rate Kg/min	Impeller Speed RPM	Δp (P_{in}-P_{out}) kPa	P_f W
3	6	150	510	46.4
3	6	300	503	45.7
3	6	500	500	45.5
2	6	500	500	45.5
1	6	150	500	45.5
1	6	300	500	45.5
1	6	500	500	45.5

As seen from table 4-1, the power arising from fluid flow (P_f) is much less than the power of the rotor, so the power of fluid flow on the power consumption of the mixer is negligible. From the experimentally measured power consumption values, determined Po and Reynolds number (Re_{RN}) values are given in table 4-2.

Table 4-2 Experimentally determined Po and Re values

c_a mm	Impeller Speed RPM	Po (-)	Re_{RN} (-)
3	150	266.4	0.451
3	300	70.7	1.425
3	500	26.67	3.33
2	500	26.61	3.33
1	150	266.8	0.451
1	300	71.46	1.425
1	500	27.33	3.33

As seen from table 4-2, the power number decreases with increasing values of the rotor speed and Reynolds numbers, which confirms that the experiments were carried out in the laminar flow regime. Indeed, the negligible effect of fluid flow on the power draw of the mixer is another evidence of laminar flow as stated by Cooke et al. (Cooke et al.-, 2012).

The results of numerically evaluated power consumption values of the investigated mixer and a comparison with experimental data are depicted in figure 4-9. The difference between numerically and experimentally obtained values is less than 5% which is in an acceptable range.

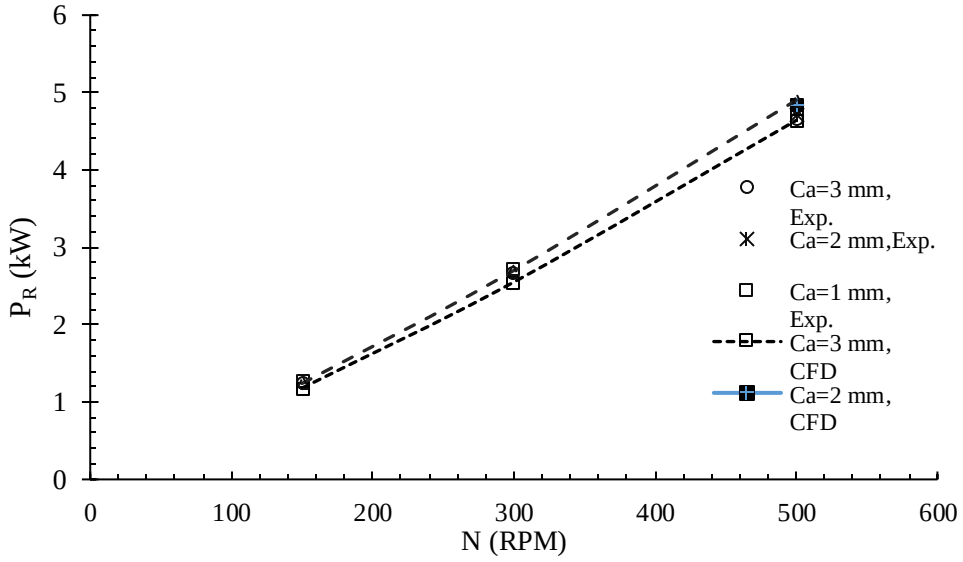

Figure 4-9 Comparison of experimentally and numerically obtained power draw values

The power constant C values have been determined for c_a of 1 mm, 2 mm, and 3 mm by simulations for the Newtonian case. Simulations have been carried out under the laminar regime for the Re between 2 and 50. From the result of simulations, the acquired Po versus the Re curves and evaluated C values are given in figure 4-10. As seen from the log-log curve, a linear relationship exists between the Po and Re with a slope of -1 which agrees with Eq. 1-168.

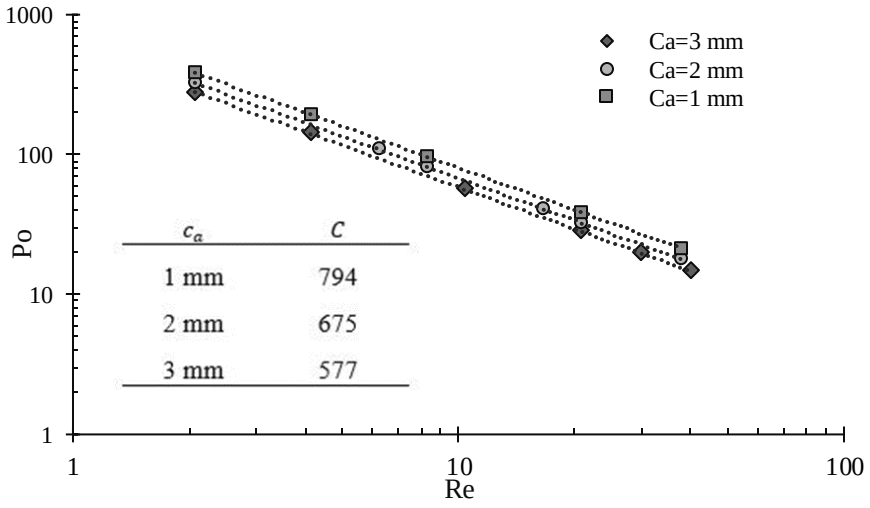

Figure 4-10 Numerically obtained Po-Re curve for the Newtonian case (Ayas et al., 2020-b)

The values of the Metzner-Otto coefficient k_s for the investigated in-line mixer have been evaluated from the experimentally and numerically obtained power consumption values and results are compared. Using Eq. 4-10 and numerically determined C values, determined k_s values are given in table 4-3. Calculated k_s values from the experimental data slightly change with impeller speed, and on the other hand, obtained k_s values from the simulations are almost constant and from the table 4-3, one can conclude that k_s can be considered as a function of geometry.

Table 4-3 Experimentally and numerically determined k_s values (Ayas et al., 2020-b)

N	c_a=1 mm		c_a=2 mm		c_a=3 mm	
RPM	k_s (Exp.)	k_s (CFD)	k_s (Exp.)	k_s (CFD)	k_s (Exp.)	k_s (CFD)
150	82.5	84.0	*	*	57.5	61.6
300	84.4	84.5	*	*	59.2	62.5
500	86.2	83.7	72.5	70.2	60.8	61.3
Average	84.4	84.1	72.5	70.2	59.2	61.8

As stated before, in the case of Herschel–Bulkley fluids, the Metzner-Otto coefficient (k_s) can be determined alternatively from the slope of $PoRe_{RN}$ versus Bi* curves according to Eq. 4-10. From the

experimentally and numerically obtained power consumption values and using C values in figure 4-10, created $PoRe_{RN}$ versus Bi* curves are illustrated in figure 4-11.

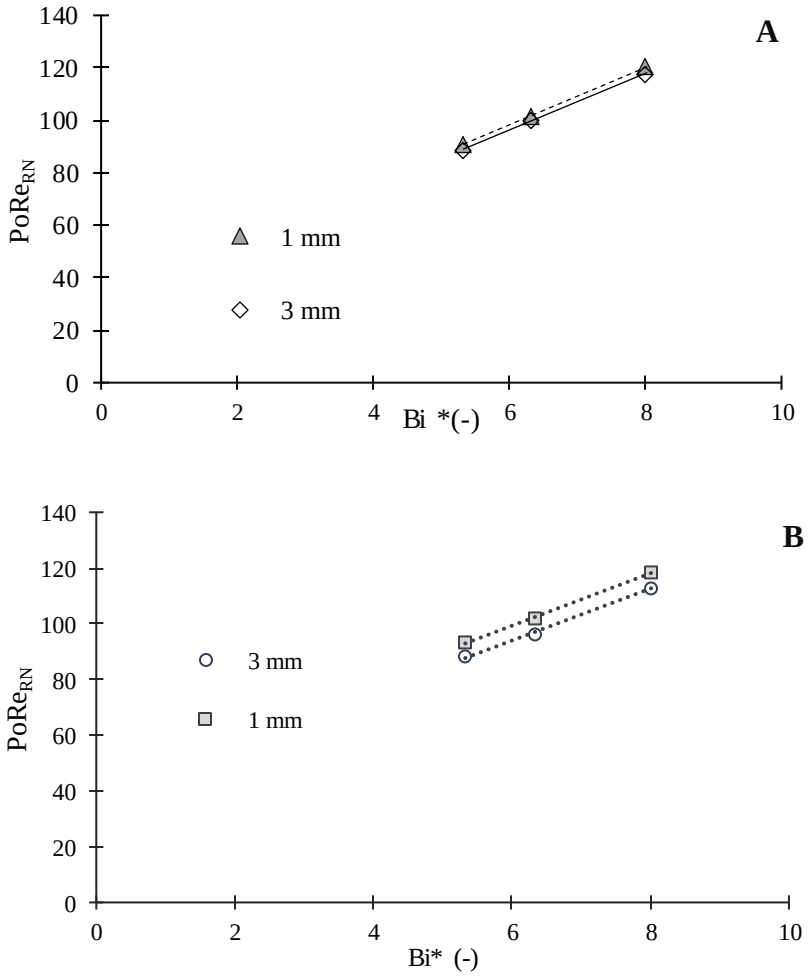

Figure 4-11 P_oRe_{RN} versus Bi* curves (A)-Experiment, (B)- CFD

As seen from the figures, $PoRe_{RN}$ versus Bi* curves show a linear characteristic with a coefficient of determination (R^2) greater than 0.99. From the curves of CFD results, k_s values are found as 84.4 and 61.8 for axial clearances (c_a) of 1 mm and 3 mm respectively which are identical to obtained results of the direct method given in table 4-3. On the other hand, from the experimental obtained k_s values were found as 73 and 53.4 for the axial clearances of 1 mm and 3 mm which shows a reasonable agreement, namely there is a 9 % deviation for $c_a = 3$ mm and 13 % deviation for $c_a = 1$ mm and the reason deviation may arise from the measurement errors, however, results are still in the acceptable range. In order to examine the impact of the rheological model on k_s, another set of simulations has been performed using the power-law model for flow indexes ranged from 0.2 to 0.7. Using the method

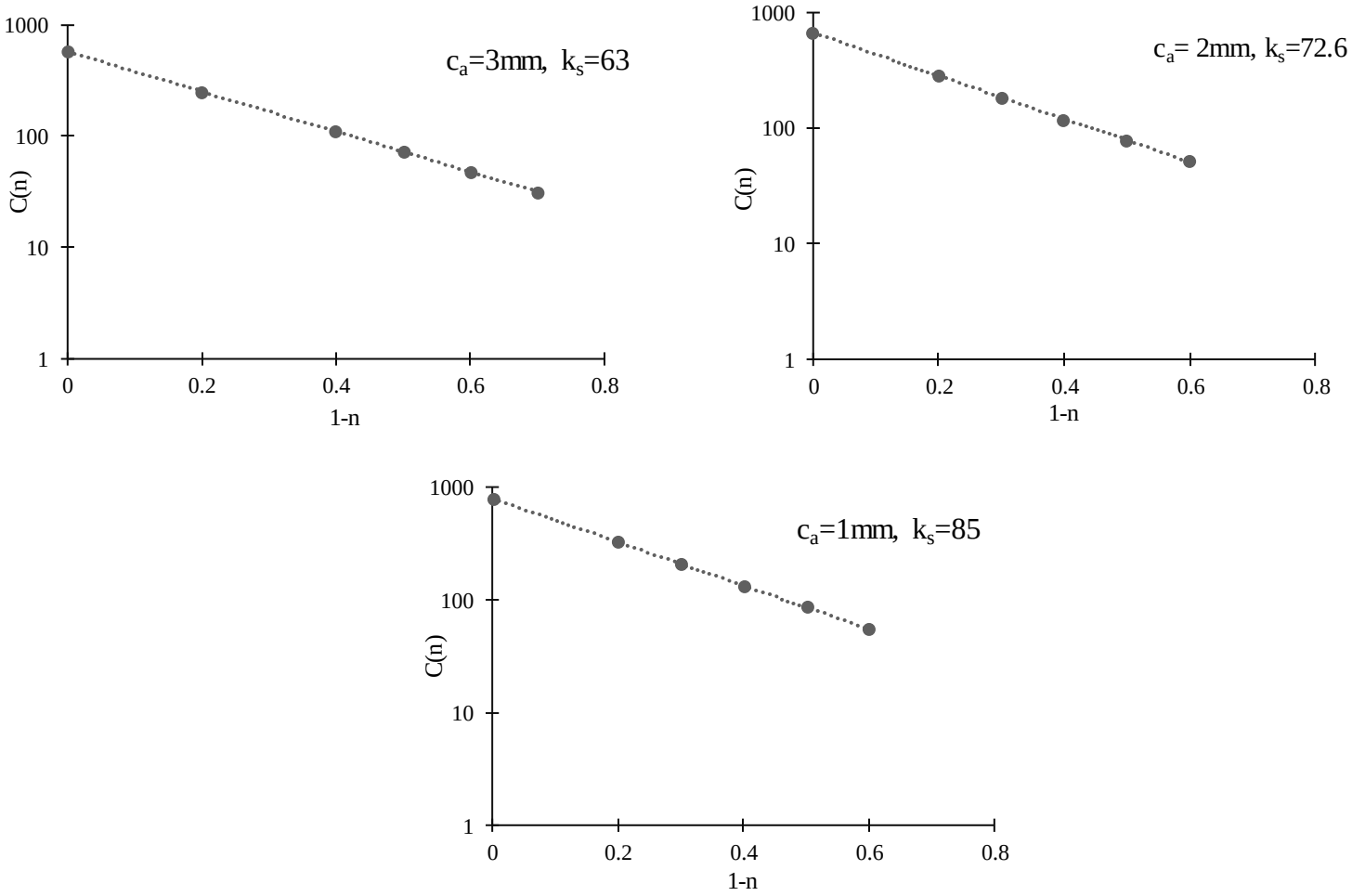

suggested by Rieger and Novak (see Eq. 1-175), obtained $C(n)$ versus $(1-n)$ plot is shown in figure 4-12.

Figure 4-12 Numerically determined k_s values for the power-law case

Results of simulations indicate that numerically evaluated k_s values for the Herschel–Bulkley, and power-law model are approximately the same. As a result, experimental and numerical data reveal that k_s can be regarded as the only function of the geometry of the mixer and can be taken as independently of the rheological model of the agitated fluid in the laminar flow regime. In addition, the relationship between the axial clearance (c_a) and non-dimensional design parameters (C, k_s) have been investigated and a linear relationship found between them for $1 \leq c_a \leq 3$ mm, which is given in figures 4-13.

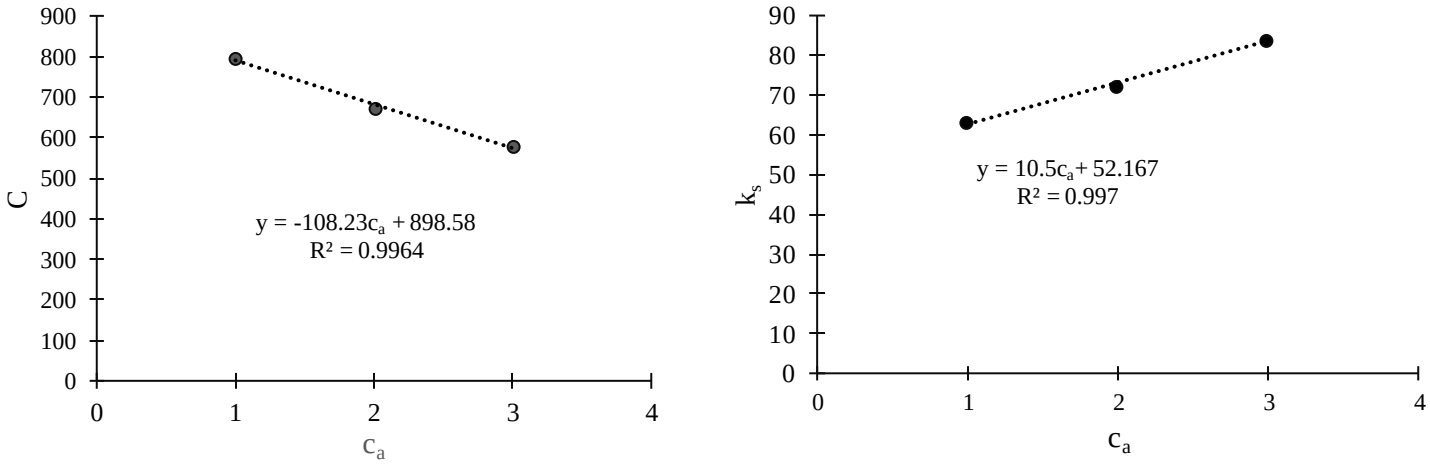

Figure 4-13 Dependence of axial clearance on C and k_s

Another studied parameter associated with the power draw of the mixer is the efficiency (X) given in Eq. 4-16. As stated before, in the case of agitation of the viscoplastic fluids, the total power number can be written as a sum of Po_y and Po_S given in Eq. 4-12 and the terms have been introduced based on Po_y and Po_S. The evaluated Po_y, Po_S and X values from the results experimental and numerical data are given in table 4-4.

Table 4-4 Po_y, Po_S and efficiency values

c_a (mm)	N (RPM)	P_o (Exp.)	Po_y (Exp.)	Po_S (Exp.)	X (Exp.)	Po (CFD)	Po_y (CFD)	Po_S (CFD)	X (CFD)
3	150	266	178.3	88.2	0.33	250.8	166.5	84.3	0.34
3	300	70.4	43.3	27.4	0.39	67.5	41.1	26.4	0.39
3	500	26.7	15.2	11.5	0.43	26.5	15.1	11.5	0.43
2	500	26.9	14.9	12.0	0.45	27.6	14.9	12.0	0.43
1	150	266.78	171.1	95.6	0.36	262.6	168.1	94.5	0.36
1	300	71.5	41.7	30.5	0.41	71.6	41.8	29.8	0.42
1	500	27.3	14.7	12.5	0.46	28.0	15.2	12.8	0.46

As seen from table 4-4, the efficiency X increases with the increasing speed of the rotor and decreases with descending values of the axial clearance. However, it is clear from the table that the clearance has a weak effect on efficiency X and significantly varies with impeller speed.

5-2 Dependence of axial clearance on velocity and shear rate profiles

As stated before, in the case of mixing of a viscous fluid in the laminar regime, the fully sheared flow should be provided in the big portion of the mixer, and dead zones must be eliminated to achieve an efficient mixing process. Therefore, the velocity and shear rate profiles within the mixing heads are studied by numerical simulations and the effect of geometry on the shear and velocity profile is analyzed

for the c_a values of 1 mm, 2 mm, and 3 mm. The shear rate distribution is investigated in midplanes between rotor and stator only. In addition, velocity profiles have been investigated in midplanes between rotor and stator and as well as in the mid-section of the mixing heads. Hence, several cut-planes have been created and velocity and shear profiles analyzed on those cut planes. The locations of the created cut planes are shown in figure 4-14. In general, the maximum velocity is found in the middle section of the mixing heads, close to the impeller tips, and the maximum shear rate is generated in the gaps between the rotor and stator.

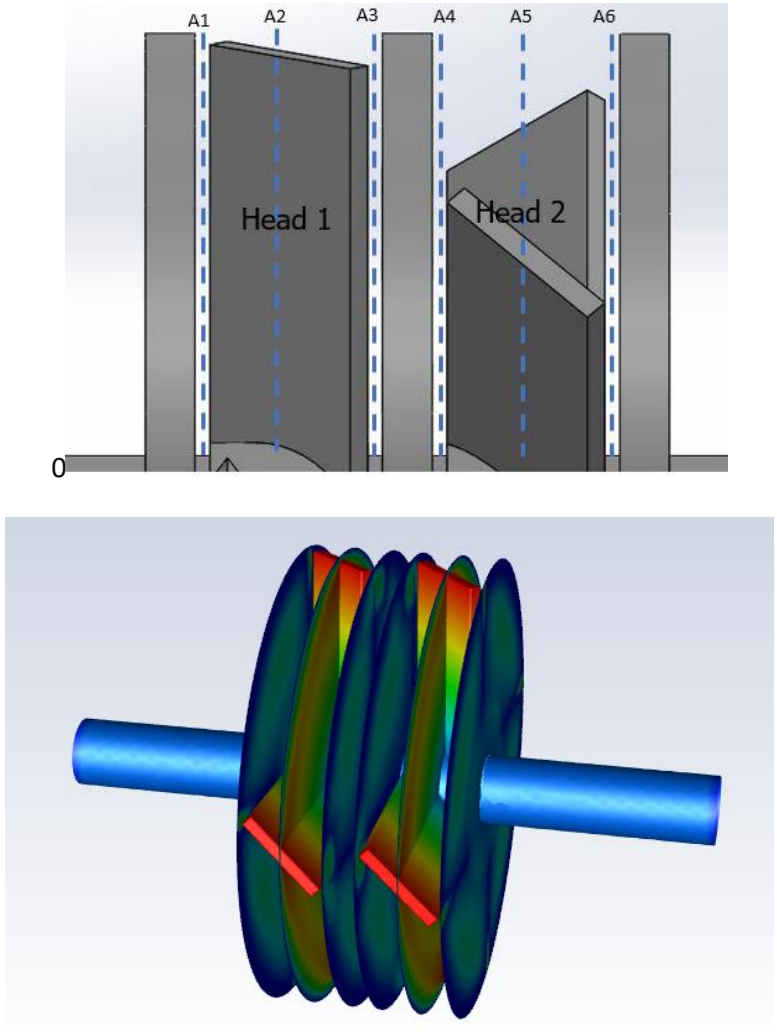

Figure 4-14 Demonstration of cut planes

The obtained dimensionless averaged mean velocities (averaging process carried out by MATLAB codes, see Appendix C) from the examined contours are shown in figure 4-15. The numerically obtained velocity profiles in head 1 and head 2 are symmetric and the results are almost identical, so only the results for the A1, A2, and A3 planes are demonstrated here. It should be noted that $0 < 2r/D < 0.2$

corresponds to the shaft and $0.2 < 2r/D < 0.4$ is inlet and outlet section of the mixer. There is a jump in velocities in the A1 plane for $0.2 < 2r/D < 0.4$ and maximum speed is observed at $2r/D = 0.9$. It is also clear that velocities in the gaps between the rotor and stator are less than the middle section of the mixer.

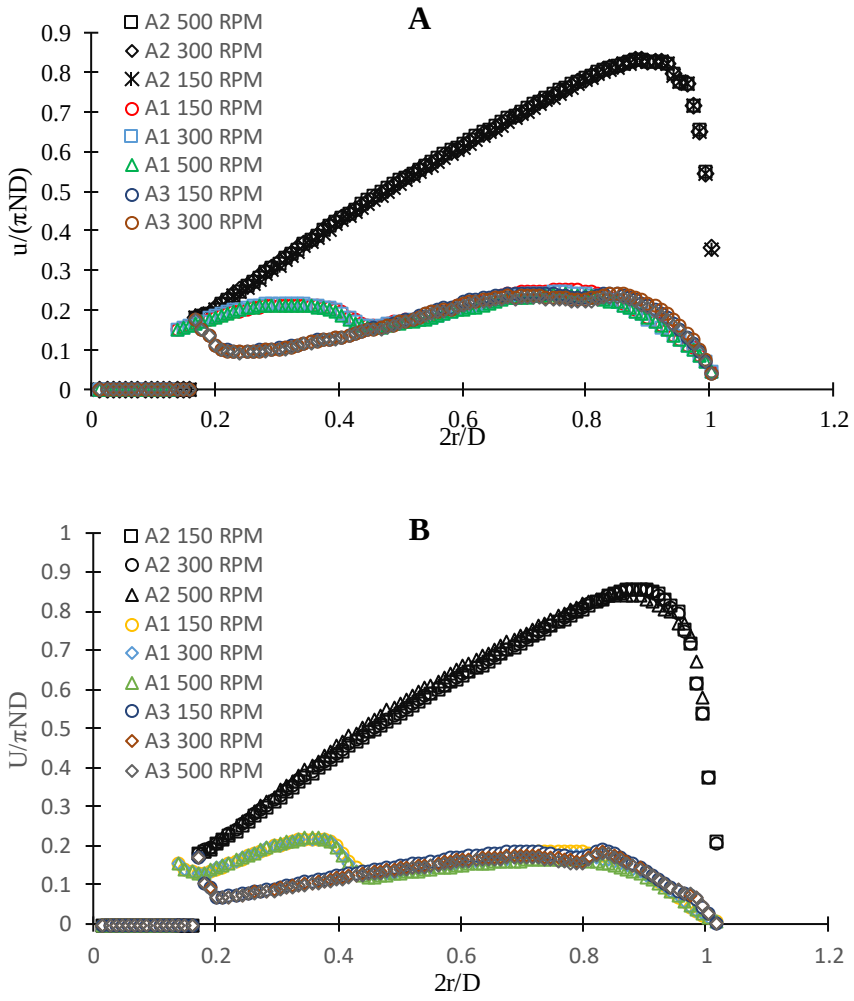

Figure 4-15 Averaged mean velocities for the investigated cut planes, (A)- c_a=3 mm, (B-c_a=1 mm

From the acquired velocity profiles, it can be deduced that the dimensionless velocity profile is strongly dependent on the position for the investigated planes and axial clearance has no significant effect on the velocity profile. The components of the directions of generated velocities within the mixer are analyzed and obtained values of axial, radial, and tangential velocity profiles are given here only for c_a of 1 mm and 3 mm are shown in figure 4-15. From the curves, it is obvious that generated flow is dominated by tangential velocity mostly, regardless of the value of axial clearances.

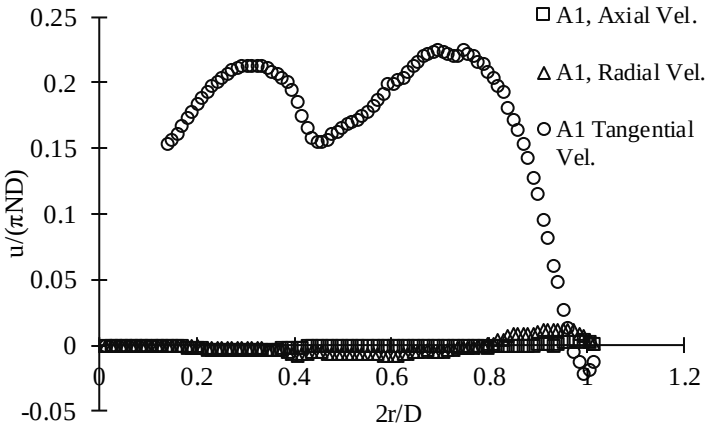

c_a=3 mm, N=500 RPM

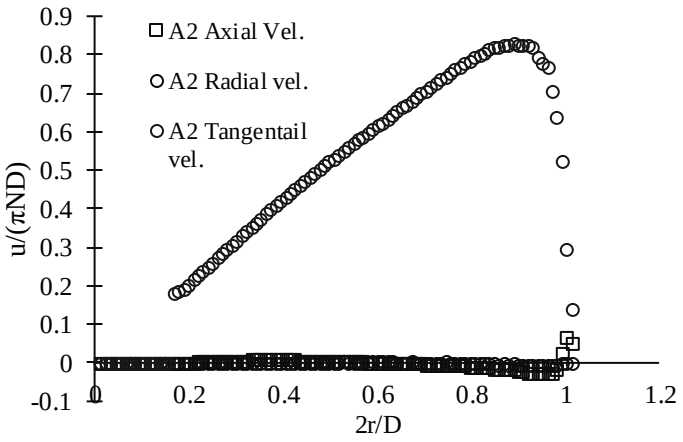

c_a=3 mm, N=500 RPM

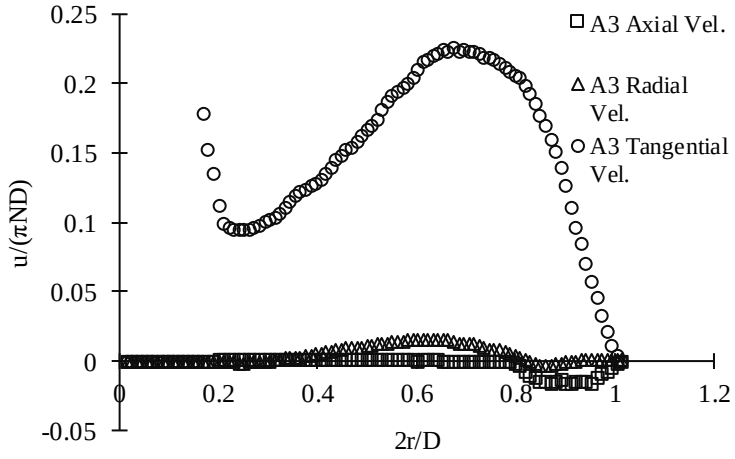

c_a=3 mm, N=500 RPM

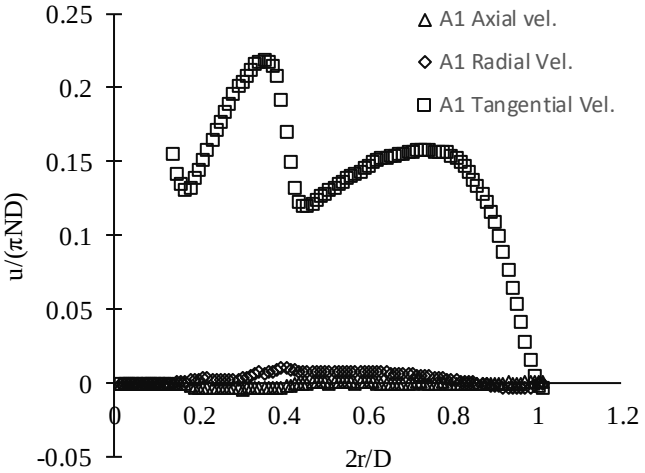

c_a=1 mm, N=500 RPM

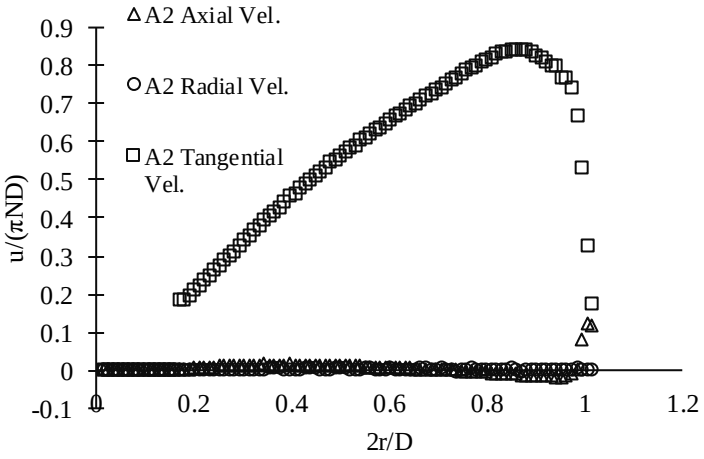

c_a=1 mm, N=500 RPM

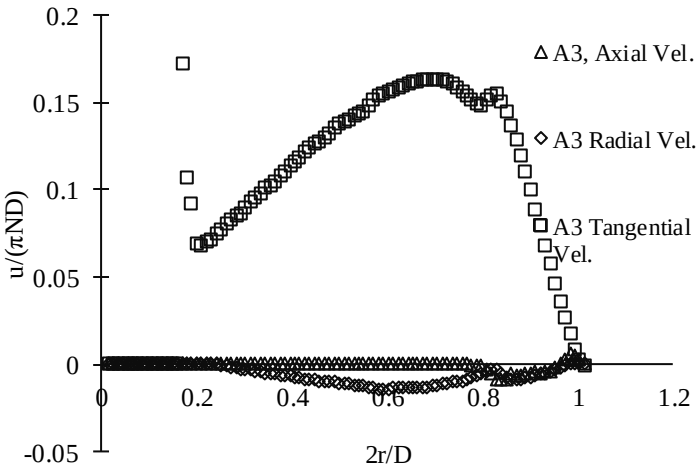

c_a=1 mm, N=500 RPM

Figure 4-16 Axial, radial, and tangential components of velocity profiles

Regarding the shear rate analysis, from the results of simulations attained contours of shear rate profile for the c_a values of 1 mm, 2 mm, and 3 mm and rotor speeds of 150, 300, and 500 RPM examined in detail. Since the generated shear rate by the rotor is inversely proportional to axial clearance and it is highly possible to detect low shear and dead zones for $c_a = 3$ mm for the investigated in-line mixer which is shown in figure 4-17 (see appendix D for the result of other axial clearances). From the figures, fully sheared flow is attained in the A1 and A3 planes and there are no dead zones except at the vicinity of the stator wall. The magnitude of the generated shear rate in plane A1 is higher than plane A3 at the vicinity of the impeller tip, but a more uniform shear profile is found for plane A3. It shows the effect of inlet and outlet sections on created shear rate. In general, the generated shear rate increases as increasing values of rotor speed as expected, and high values of shear rates are generated between the rotors and at the vicinity of the rotor tip.

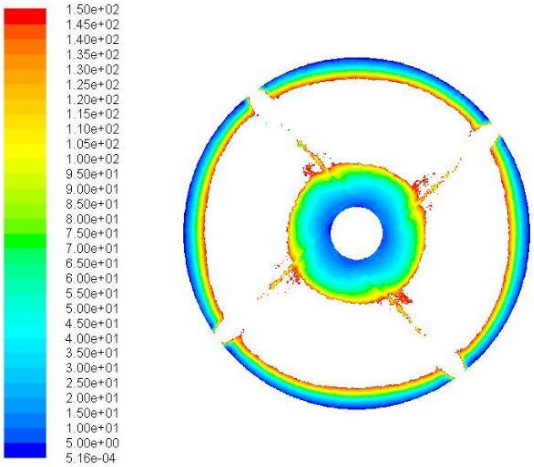

c_a=3 mm, 150 RPM, plane A1 (0-150, 1/s)

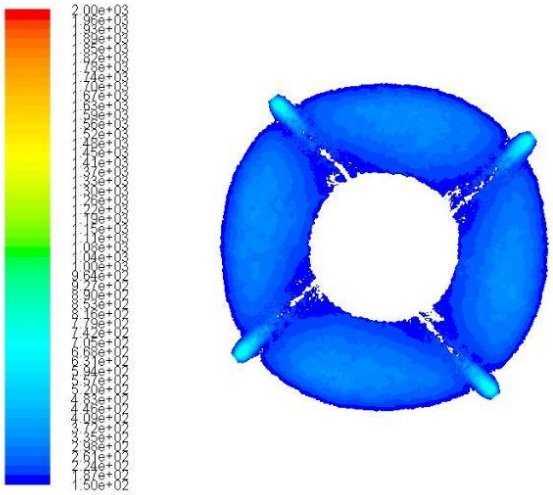

c_a=3 mm, 150 RPM, plane A1 (150-2000, 1/s)

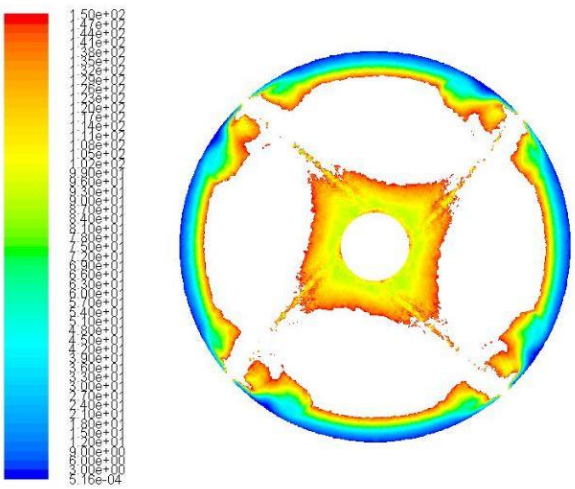

c_a=3 mm, 150 RPM, plane A3 (0-150, 1/s)

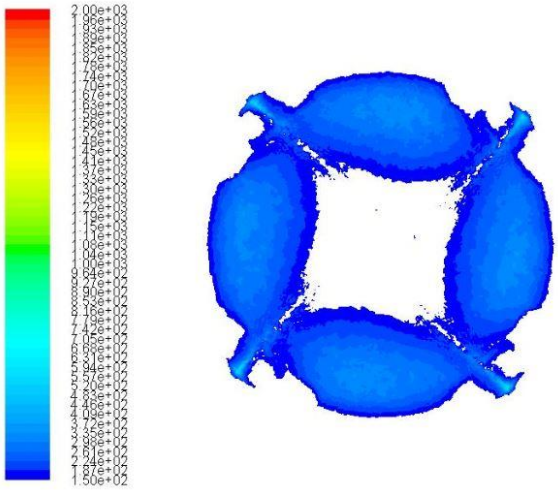

c_a=3 mm, 150 RPM, plane A3 (150-2000, 1/s)

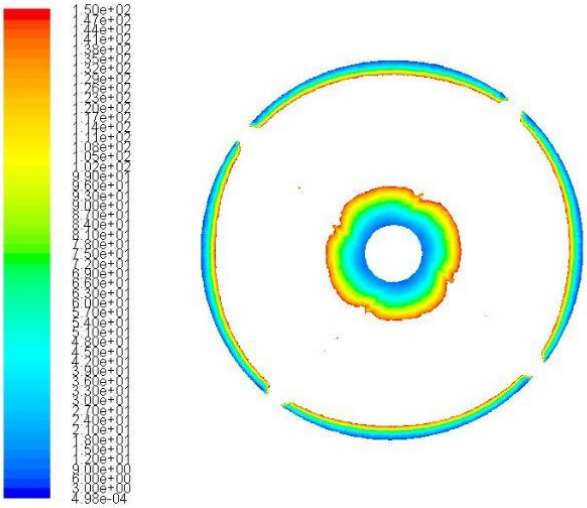

c_a=3 mm, 300 RPM, plane A1 (0-150, 1/s)

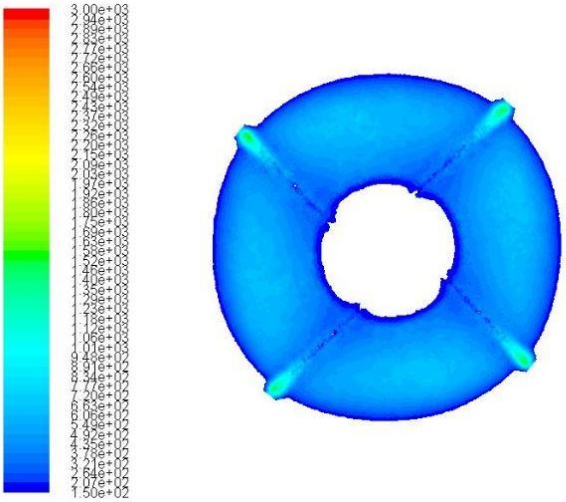

c_a=3 mm, 300 RPM, plane A1 (150-3000, 1/s)

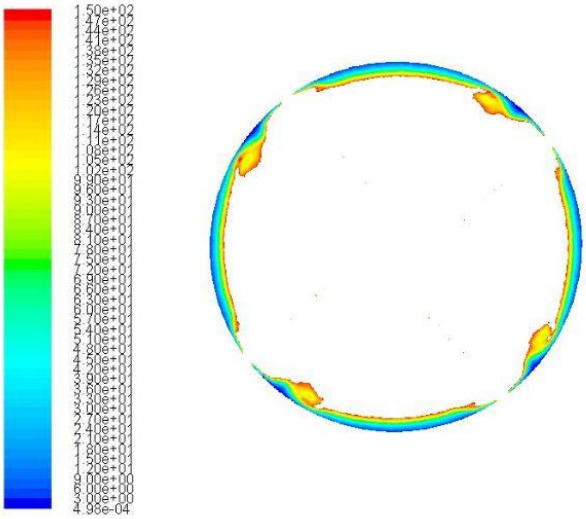

c_a=3 mm, 300 RPM, plane A3 (0-150, 1/s)

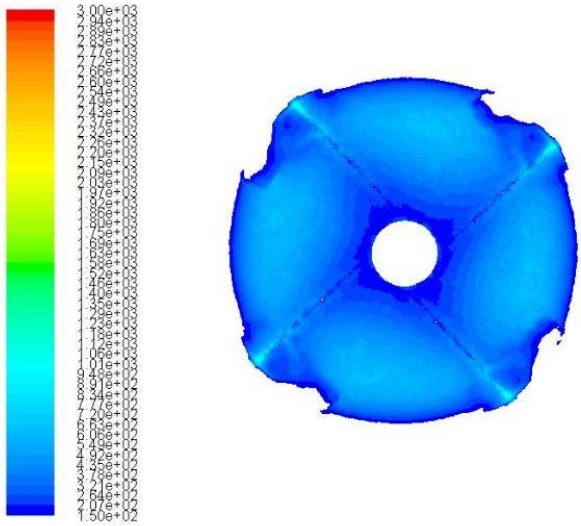

c_a=3 mm, 300 RPM, plane A3 (150-3000, 1/s)

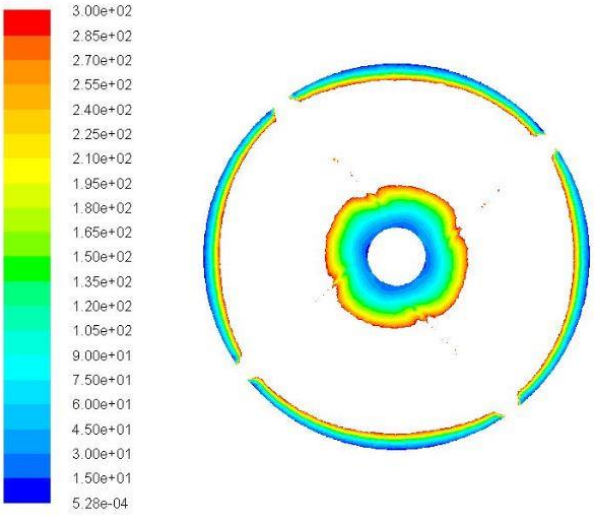

c_a=3 mm, 500 RPM, plane A1 (0-300, 1/s)

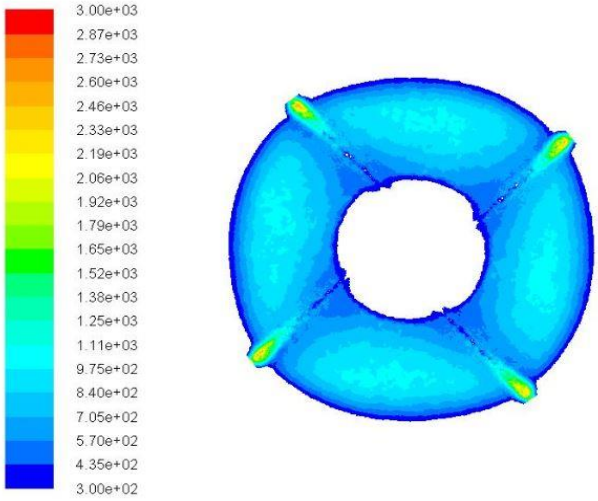

c_a=3 mm, 500 RPM, plane A1 (300-3000, 1/s)

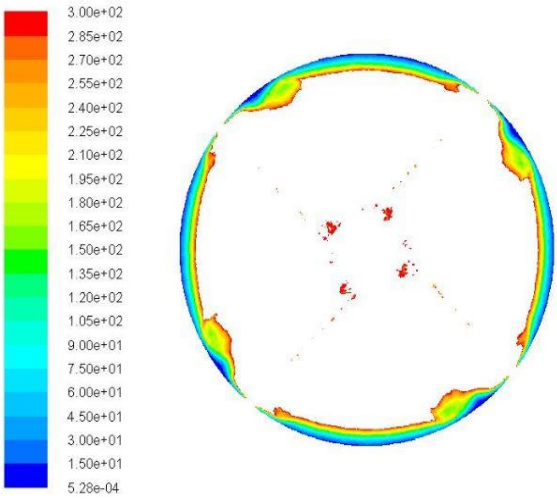

c_a=3 mm, 500 RPM, plane A3 (0-300, 1/s)

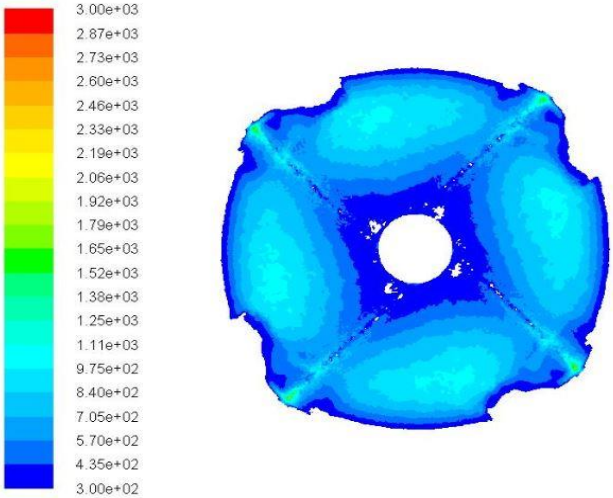

c_a=3 mm, 500 RPM, plane A3 (300-3000, 1/s)

Figure 4-17 Contours of shear rate (1/s) for c_a= 3mm

From the shear rate contours, evaluated non-dimensional shear rate ($\gamma^* = \dot{\gamma}/N$) distribution curves for the c_a values of 1 mm and 3 mm are given in figure 4-19.

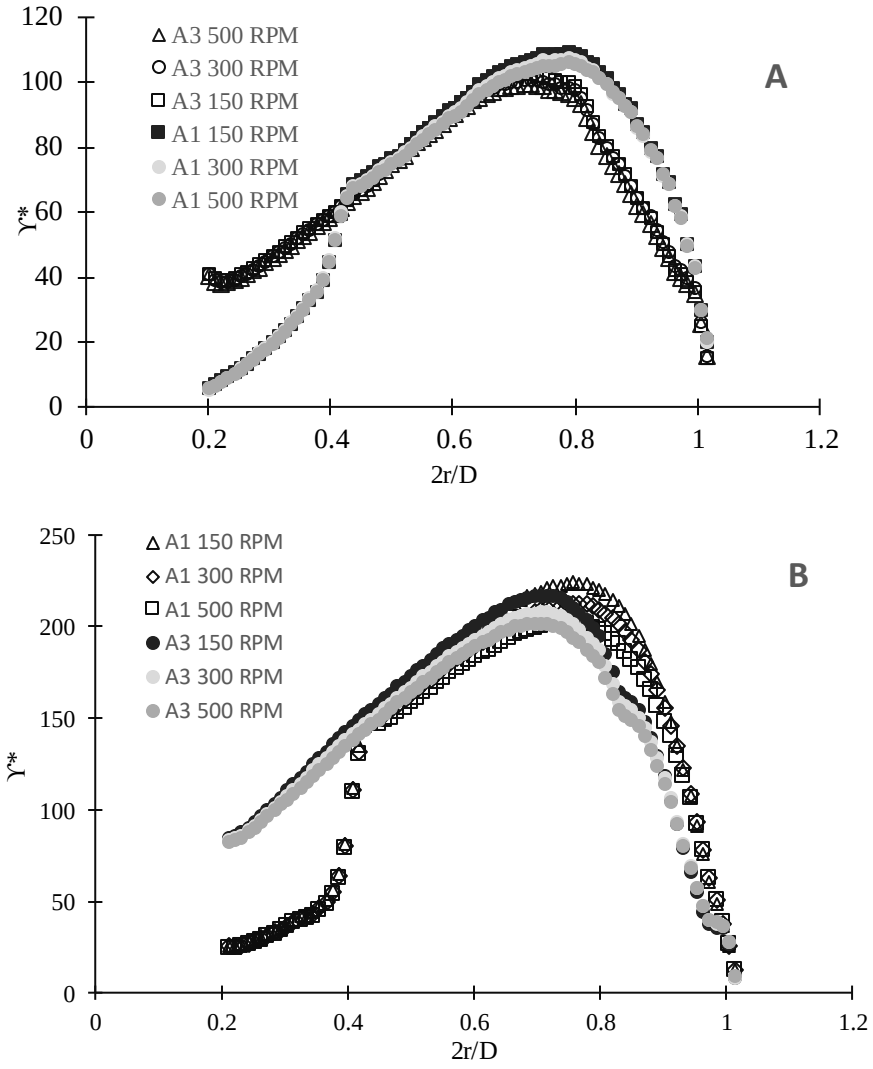

Figure 4-18 Dimensionless shear rate profile (A)- c_a=3 mm (B)-c_a=1 mm

From the figures, it can be concluded that the evaluated dimensionless shear profile is independent of rotor speed and significantly hinge upon the geometry. The curves indicate that fully sheared flow is provided in the investigated planes and there are no dead zones. The generated shear in planes A1 is higher than planes A3 at the vicinity of the impellers, whereas at $0.2 < r/R < 0.4$, generated shear rate in planes A3 is almost two times more than planes of A1 due to the inlet flow effect. The highest values of the shear are created about 2r/D=0.8 for all planes. Variation of dimensionless shear rate concerning axial clearances of 1 mm, 2mm, and 3 mm for N= 500 RPM is given in figure 4-20. The plots indicate that lower values of axial clearance result in higher shear profile and that provides a better mixing.

From figure 4-20, it can be deduced that the shear profile can be improved by changing the geometry between rotor and stator in the axial direction or modifying the geometry of the inlet and outlet section. Especially inlet and outlet sections lead to a decrease in shear rates and a better shear profile can be acquired by changing the cross-sectional area of the inlet and outlet region. It should be indicated that, although higher values of axial clearances result in lower values of shear rate, that provides to agitate more volume of the liquid per unit time. Namely, the economical aspects of the mixing process should be concerned during the designing of the mixers according to the requirements of the process.

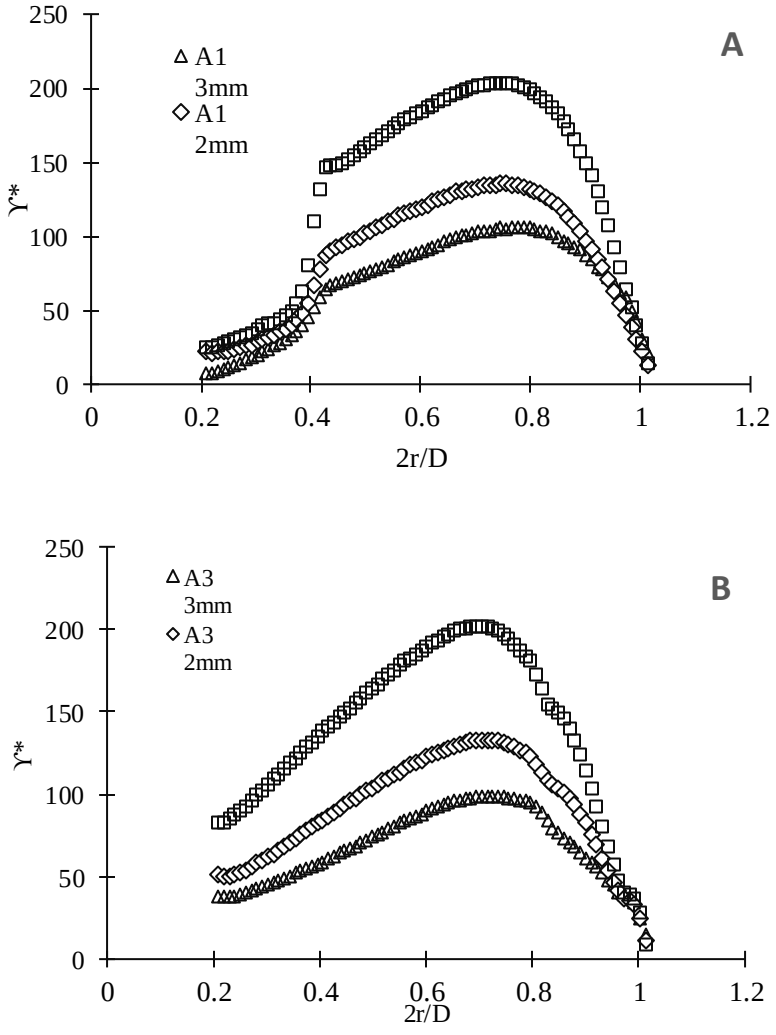

Figure 4-19 Effect of axial clearance on the dimensionless shear rate for N=500 RPM (A)- plane A1 (B)-Plane A2

The final numerical investigation has been performed for the power-law fluids in order to investigate the effect of a different rheological model on non-dimensional shear rate profile and obtained results are

compared with the results of Herschel–Bulkley model. Firstly, the effect of flow indexes on the dimensionless shear rate profile has been examined for c_a = 3 mm and the rotor speed of 60 RPM which is given in figure 4-21. It is a known fact that the Metzner-Otto coefficient is a weak function of flow indexes and the effect of flow indexes on power consumption has been shown in the previous section. A similar effect has been found for the dimensionless shear rates. As seen from the curves, the variation of dimensionless shear rate with respect to flow indexes is almost negligible. The effect of flow indexes on the dimensionless shear rate in the investigated planes is found as a weak function of flow indexes the same as the case of the Metzner-Otto coefficient.

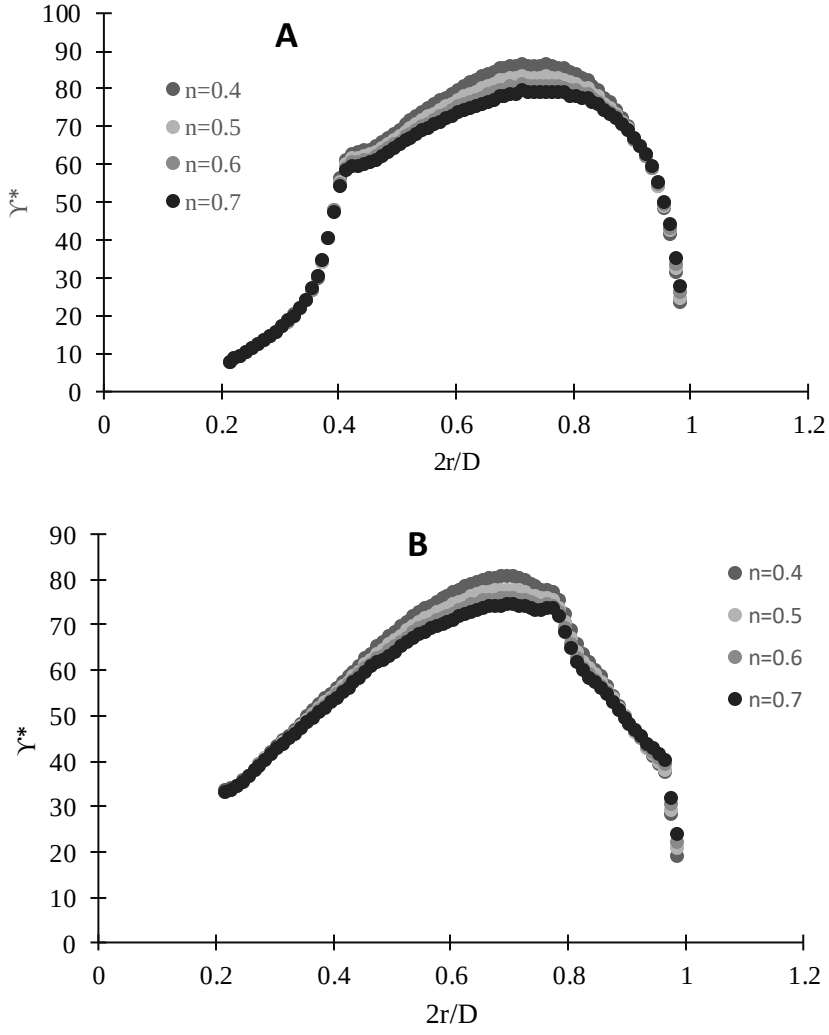

Figure 4-20 Effect of flow index on the dimensionless shear rate (A)- Plane A1 (B)- Plane A3

The effect of axial clearance on the dimensionless shear rate has been examined for n = 0.5 and N = 500 RPM with axial clearances of c_a = 1 mm, 2 mm, and 3 mm, and the result is shown in figure 4-20.

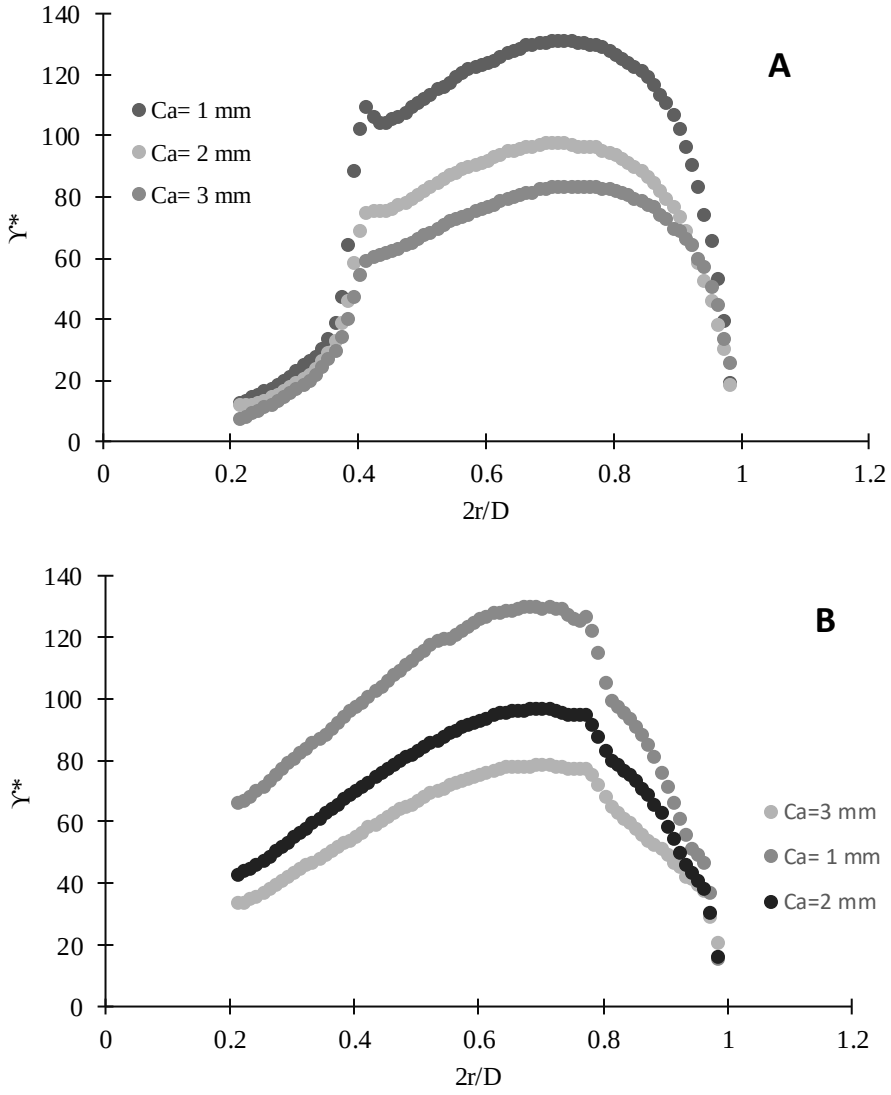

Figure 4-21 Effect of axial clearance on the dimensionless shear rate for n=0.5 (A)- Plane A1 (B)- Plane A3

The curves indicate that generated shear rates in the gaps between rotor and stator vary significantly with the axial clearance the same as in the case of the Herschel–Bulkley model. In addition, obtained dimensionless shear rate profiles from the power-law and Herschel–Bulkley models are quite similar but the magnitude of dimensionless shear rate in the investigated planes affected by the axial rheological model of the fluid. Obtained dimensionless shear rates from the power-law model are slightly lower than the Herschel–Bulkley model for c_a = 3 mm, however for c_a = 1 mm, the calculated dimensionless shear

rates from Herschel–Bulkley model are significantly higher than obtained dimensionless shear rates for the power-law model.

Regardless of the rheological model of the fluid, it is obvious from the curves that obtained dimensionless shear rate from the c_a = 1 mm is approximately two times higher than that obtained from c_a = 3 mm, thus it is strongly recommended that possible minimum clearance should be maintained to provide high shear rates. Also, as seen from the curves the inlet, passage section, and outlet have a decreasing effect on shear rates. In order to obtain a more efficient mixing, the sizes of those sections should be minimized as much as possible.

6- Conclusion

In this chapter, the power characteristics of a newly designed in-line rotor-stator mixer have been investigated experimentally and numerically. The experiments were carried out for the three rotational speeds of the rotor and three axial clearances between rotor and stator using viscoplastic shear-thinning fluid.

The power demand of the mixer, temperature growth of the agitated fluid, and the pressure gradient between inlet and outlet sections of the mixer were measured by experiments. From the results of experiments, it was found that the contribution of the power demand of flowing fluid has a negligible effect on the total power input of the mixer, and the temperature rise in the agitated fluid is only affected by rotor speed.

The experimentally obtained power consumption values of the mixer were verified by numerical simulations. It was shown that experimentally and numerically acquired power consumption values were in good agreement with a 6 % maximum deviation. The dimensionless power constant of the investigated mixer was determined numerically for each geometrical configuration. From the experimentally and numerically obtained power consumption values, Metzner-Otto coefficients of the investigated mixer were determined based on numerically evaluated power draw coefficients. It was shown that evaluated Metzner-Otto coefficients from the experimental and numerical data are very close.

Then, the effect of the rheological model on the Metzner-Otto coefficient was investigated numerically using the power-law model and the same values of Metzner-Otto coefficients were acquired. It was confirmed that the value of the Metzner-Otto coefficient varies with the geometry and is independent of rheological properties for inelastic fluids and numerical simulations can be used to successfully determine power draw and Metzner-Otto coefficients.

A new correlation was proposed to express the power characteristics of a mixer for the Herschel–Bulkley model based on the Reynolds number introduced by Rieger and Novak given in Eq. 4-10. According to Eq. 4-10, the total power consumption of a mixer can be written as the sum of the power necessary to overcome yield stress, and the required power shear flow and corresponding power numbers (Po_y, Po_s) were defined. By using defined Po_y and Po_s the new term efficiency (X) was introduced to analyze the shear efficiency of the agitation of yield stress fluids. One was concluded that even though the higher speed of the impeller results in higher power draw, it provides more efficient mixing in terms of generated shear in the mixer.

Moreover, the shear rate profile in the middle sections between the rotor and stator was examined by numerical simulations. It was shown that fully sheared flow was provided within the mixing heads for the tested rotational speed of the rotor. It was indicated that higher shear rates can be acquired by reducing axial clearance and the power draw of the mixer is significantly varies with the rotor speed.

The most important parameter of the mixing process in the laminar regime is the homogeneity of the product which is proportional to generated flow in the mixer. It depends on the dissipated energy within the process and geometry of the mixer. Hence, providing a better flow profile in the mixing plane and decreasing clearance between the rotor and stator is a better way to avoid high power draw.

Chapter 5 -Conclusion

This work deals with the measurement of rheological properties of the purely viscous non-Newtonian fluid, prediction of friction factor, and power and flow characteristics of an in-line rotor-stator mixer. The design and process parameters of any equipment and apparatus involving non-Newtonian fluid flow are strongly dependent on rheological parameters and models of the processed fluids.

Firstly, a method is suggested for the evaluation of the rheological parameters for the power-law fluids using the rectangular channel and concentric annuli. According to the method, the relationship between wall shear rate and wall shear stress can be represented by one geometrical parameter for any aspect ratios. Then, the suggested method was validated by using experimental data in the literature for bovine collagen. The rheological parameters of the collagen for power-law fluids from the suggested method and Herschel–Bulkley model using conventional methods. It has been shown that rectangular channels and concentric annulus can be used for the determination of rheological parameters the same as slit and capillary rheometers for the power-law fluids. In addition, evaluated rheological parameters for the power-law model from the experimental data were validated using simulations and good agreement was found between them.

Moreover, the obtained simplified correlation has been used to re-cast friction factor-Reynolds number relationship for the flow of power-law fluids in the laminar flow regime by introducing the modified Reynolds number suggested by Metzner and Reed for the rapid engineering calculations. The provided method is validated by comparing the most frequently used methods and through numerical simulations and it was found that the suggested method can predict friction factor accurately. According to the suggested method, the Reynolds number is determined independently of shape and geometrical ratios of the channel, and the friction factor- Reynolds number equation can be expressed by a simple linear equation.

Finally, the power characteristics and flow field of a newly designed in-line rotor-stator mixer have been analyzed experimentally and numerically according to the determined rheological parameters in the previous section. Firstly, the power draw of the mixer has been measured experimentally for the three rotational speeds of the impeller and three different axial clearances of the mixer, and then obtained power draw results have been validated by numerical simulation, and a good agreement was found

between the numerically and experimentally obtained power values. The Newtonian power draw coefficient has been calculated by numerical simulations and then, Metzner-Otto constants have been determined from the experimentally and numerically obtained power draw results. It was found that determined Metzner-Otto coefficients from the experimental and numerical methods are in good agreement. It is shown that numerical methods are a useful tool for the determination of the power characteristics of the mixers in the laminar regime. Besides, the methodology for the determination of Metzner-Otto constant for power-law fluids suggested by Rieger and Novak is extended to the Herschel–Bulkley model, and it was shown that in case of mixing of yield shear-thinning fluids, the total power consumption is equal to the power of shearing flow and the power exceeding yield stress and the term efficiency is introduced. A slope method was proposed for the determination of the Metzner-Otto coefficient for the Herschel–Bulkley model and it was shown that the introduced method is successful for the prediction of the Metzner-Otto coefficient. In the final step, the effect of axial clearance on velocity and shear profile is discussed and it was found that axial clearance has a remarkable effect on flow profile on the agitated fluid in the mixer.

Nomenclature

a	Parameter of Eq. 1-188
A, B	Parameter of Eq. 1-14 (Pa.s)
a, b	Geometrical parameters of Eq. 1-133 (-)
A, B	Dimensions of the symmetrical L-shape duct (m)
Bi	Bingham number (-)
Bi^*	Bingham number for Herschel-Bulkley model (-)
C	Geometric parameter of the Newtonian fluid for channels (-)
C	Integration constant (-)
C	Newtonian power constant (-)
Ca	Capillary number (-)
GCI	Grid convergence index (-)
d, D	Diameter (m)
D_h	Hydraulic diameter (m)
D_c	The diameter of the cavern (m)
d_{32}	Sauter diameter (m)
De	Deborah number (-)
e^*	Dimensionless eccentricity (-)
e	Length of eccentricity (m)
G	Shear modulus (Pa)
h	Height of impeller blade (m)
h_C	Height of cavern (m)
H	Height of the rectangular duct (m)
h	Parameter defined in Eq. 1-189
He	Hedstrom number (-)
K	Fluid consistency for power-law and Herschel-Bulkley models ($Pa.s^n$)
k_s	Metzner-Otto coefficient (-)
L	Length (m)

L_e	Length of the entrance region (m)
m	Consistency for Casson model ($Pa.s^n$)
M	Number of mesh elements (-)
M, N	Parameters of Eq. 3-3 (-)
M', N'	Parameters of Eq. 3-10 (-)
n	Flow behavior index (-)
N	Rotational velocity (RPM)
N_1 , N_2	First and second normal stress difference (Pa)
p	Pressure (Pa)
p	Parameter of Cross model (-)
P	Power (W)
p	Parameter of Eq. 1-188
Po	Power number (-)
R	Radius (m)
R_M	Mean radius (m)
R_i	Inner radius (m)
R_i	Inner radius (m)
R_o	Outer radius (m)
Re	Reynolds number for Newtonian fluids (-)
Re_D	Generalized Reynolds number defined by Delplace and Leuliet (-)
Re_G	Generalized Reynolds number by Kozicki (-)
Re_M	Reynolds number, as defined by Metzner and Reed (-)
Re_M'	Reynolds number, as defined in Eq 3-19 (-)
Re_{MO}	Reynolds number defined by Metzner and Otto (-)
Re_{RN}	Reynolds number defined by Rieger and Novak (-)
t	Time (s)
T	Tank diameter (m)
T	Temperature (K)
T	Torque (N.m)
T_i	Torque at the inner radius (N.m)

t_e	Characteristic time of deformation (s)
u	Velocity (m/s)
$\bar{u}$	Mean velocity (m/s)
u_{max}	The maximum velocity in the cross-section of the duct (m)
u_s	Wall sleep velocity (m/s)
u'	Corrected wall sleep (m/s)
V	Volume
$\dot{V}$	Volume flow rate (m^3/s)
W	Width of the rectangular duct (m)
We	Weber number (-)
X, Y	Major and minor axes of an elliptical duct (m)

Greek letters

α	Function given in Eq. 3-1
ε	Rate of energy dissipation (W/kg)
ε	Ratio of Re_M to Re_G (-)
ε'	Parameter given in Eq. 3-9 (-)
θ	Apex angle of an isoscale triangle (°)
θ	Parameter of Carreu model
κ	Aspect ratio
λ	Kolmogorov length microscale (m)
λ	Relaxation time (s)
λ	Fanning friction factor (-)
μ'	Viscosity of the gas at T_0 (Pa.s)
ν	Kinematic viscosity (m^2/s)
σ	Interfacial tension (Pa/m)
σ	Total stress (Pa)
ψ	Normal stress coefficents ($Pa.s^2$)
ω	Angular velocity (rad/s)
ϕ	Result of numerical simulation (-)

$\dot{\gamma}$	Shear rate (s^{-1})
$\dot{\gamma}_N$	Newtonian wall shear rate (s^{-1})
$\dot{\gamma}_c$	Critical shear rate (s^{-1})
$\dot{\gamma}_w$	Wall shear rate (s^{-1})
η	Apparent viscosity (Pa.s)
μ	Viscosity of Newtnonian fluids (Pa.s)
μ_0	Zero shear viscosity (Pa.s)
μ_∞	Infinite shear viscosity (Pa.s)
μ_a	Apparent viscosity (Pa.s)
μ_c	The viscosity of continuous phase (Pa.s)
μ_d	The viscosity of dispersed phase (Pa.s)
μ_p	Plastic viscosity (Pa.s)
ρ	Density ($kg.m^{-3}$)
ρ_c	Density of continuous phase ($kg.m^{-3}$)
ρ_d	The density of dispersed phase ($kg.m^{-3}$)
τ	Shear stress (Pa)
τ_i	Shear stress at the inner radius (Pa)
τ_o	Yield Stress (Pa)
τ_w	Wall shear stress (Pa)
ϕ_{ext}	Result of numerical simulation for the infinite number of the grid (-)
Δ	Rate of deformation tensor (1/s)
v	Geometrical constants in Eq. 1-155 (-)
δ	Clearance between rotor and stator (m)
δ_{ij}	Unit tensor (-)

References

1. Adams W. L., Barigou M., CFD analysis of caverns and pseudo-caverns developed during mixing of non-Newtonian fluids, Trans IChemE., **85**, 598-604 (2007)
2. Aho J., Syrjala S., Shear viscosity measurements of polymer melts using injection molding machine with adjustable slit die, Polymer Testing, **30**, 595-601, (2011).
3. ANSYS Fluent 15.0 User's Guide, ANSYS Inc. Canonsburg , (2013).
4. Archard A. D., Marouche M., Boisson H.C., Hydrodynamics and Metzner–Otto correlation in stirred vessels for yield stress fluids, Chem. Eng. Sci., **125**, 15-24, (2006).
5. Barners H.A, Hutton J.F, and Walters K., An introduction to rheology 1st edition, Netherland, Elsevier, (1989)
6. Bertrand F., Tanguy P. A., Fuente E. B., A new perspective for the mixing of yield stress fluids with anchor impellers, J Chem. Eng. Jpn., **29**, 51-58, (1996).
7. Chhabra, R.P and Richardson, J.F., Non-Newtonian Flow and Applied Rheology, 2nd edition, Oxford, Butterworth-Heinemann (2008).
8. Collyer A. A., Clegg D. W., Rheological Measurement, 2nd edition, Springer Science-Business Media Dordrecht, (1998)
9. Cooke M., Rodgers T.L., Kowalski A. J., Power Consumption Characteristics of an In-Line Silverson High Shear Mixer, AIChE, **58**, 1683-1692, (2012).
10. Crespi-Llorens D., P. Vicente, A. Viedma, "Generalized Reynolds number and viscosity definition for non-Newtonian fluid flow in ducts of non-uniform cross-sections", Exp Therm Fluid SC., **64**, 125-133 (2015).
11. Darby R., Viscoelastic fluids-An introduction to their properties and behavior, New York, Markel Dekker Inc., (1976)
12. Deglon D.A, Meyer .C.J, CFD modelling of stirred tanks: Numerical considerations, Miner. Eng., **19**, 1059-1068, (2006).
13. Delplace F., Leuliet J.C, "Generalized Reynolds number for the flow of Power-law fluids in cylindrical ducts of arbitrary cross-section", Chem. Eng. J. **56**, 33-37 (1995)
14. Ditl P. and Sulc R., Dispersion kinetics modelling, Technical Transactions, 83-93, (2016)
15. Doran P., Bioprocess Engineering Principles 2nd edition, U.K., Academic Press, (2013)
16. Elson T. P., Cheesman D.J., and Nienow A.W., X-ray studies of cavern sizes and mixing performance with fluids possessing a yield stress, Chem. Eng. Sci**, 10**, 2555-2562, (1986).

17. Ferguson J., Kemblowski Z., Applied fluid rheology, London, Elsevier Applied Science, (1991)
18. FLUENT Theory Guide, Release 14.5. ANSYS, Inc., (2012).
19. Frigaard I. A., C. Nouar C. On the usage of viscosity regularization methods for visco-plastic fluid flow computation, J. Non-Newtonian Fluid Mech., **127**, 1–26, (2005).
20. Fuente E.B, Choplin L., Tanguy P.A., Mixing with helical ribbon impeller: Effect of highly shear thinning behavior and impeller geometry, I. Chem. E. **5**, 45-52, (1997).
21. Han C.D., J., Measurement of the rheological properties of polymer melts with slit rheometer. I. Homopolymer systems, Appl. Polym. Sci, **15**, 2567-2577, (1971)
22. Hanks R.W and Larsen K.M., The flow of power-law Newtonian fluids in concentric annuli, Ind. Eng. Chem. Fundamen., **18,** 33-35, (1979).
23. Hartnett JP, Kostic M, Adv Heat transfer, **19**, 247-356, (1989)
24. Harnby N., Edwards M. F, and Nienow A. W., Mixing in the process industries, 2nd Edition, Butterworth-Heinemann, UK, (1992).
25. Hatzikiriakos S.C., Wall slip of molten polymers , Prog. Polym. Sci. , **37**, 642-634, (2012)
26. Hay G., Mackay M. E., Awati K. M., and Park Y., Pressure and temperature effects in slit rheometer, J. Rheol., **43**, 1099-1116, (1999)
27. Kostic M. and Hartnett J. P., Predicting turbulent friction factor of non-Newtonian fluid in non-circular ducts, Int. Comm. Heat Mass Transfer, **11**, 345-352, (1984).
28. 13- Kowalski A.J., An expression for the power consumption of in-line rotor-stator devices, Chem Eng Process., 2009, 48, 581-585
29. Kozicki W., Chou C.H, Tiu C, Non-Newtonian flow in ducts of arbitrary cross-sectional shape, Chem. Eng. Sci, **21**, pp 665-679; (1966)
30. Kresta S.M, Etchells A.W, Dickey S. D, Obeng-Atiemo V.A., Advances in industrial mixing, 1st Edition, Willey, U.S. (2016).
31. Laun H.M., Polymer melt rheology with a slit die, Rheol. Acta, **22**, 171 - 185 (1983)
32. Macosko C.W., Rheology: Principles, measurements, and applications, Wiley-VCH, New York (1994)
33. Maindarkar S., Dubbelboer A., Meuldijk J., Hoogland H., Henson M., Prediction of emulsion drop size distributions in colloid mills, Chem. Eng. Sci, **118**, 114-125, (2014)
34. Malkin Y.A., Isayev A. I., Rheology- Concept methods and applications 3rd edition, ChemTec, Toronto (2017).

35. Mazzanti V., Mollica F., In-line rheometry of polypropylene-based Wood Polymer Composites, Polymer Testing, **47**, 30-35, (2015)
36. McClements D. J., Food emulsions. 3rd Edition, CRC Press- Taylor & Francis Group, US, (2016).
37. McCabe W.L, Smith J.C, and Harriott P., Unit operations of chemical engineering, 5th Edition, McGraw-Hill, US, (1993).
38. Metzner A.B, Reed J.C., Flow of non-Newtonian Fluids- Correlations of the laminar, transition and turbulent flow regions, AlChe J. 1, 434-440 (1955).
39. Metzner A. B., Otto R.E., Agitation of non-Newtonian fluids, AIChe J. **3**, 3-11 (1957).
40. Mezger T. G., The rheology handbook 4th edition, Hanover, Vincentz Network, (2014).
41. Miller C., "Predicting Non-Newtonian Flow Behaviour in Ducts of Unusual Cross Section", Ind. Eng. Chem. Fundam. 11, 330-332 (1972).
42. Mitsuishi N., Aoyagi Y., "Non-Newtonian flow in the non-circular pipe", Chem. Eng. Sci. 24, 309-319, (1969).
43. Moon J.S., Lee J.M., Shear viscosity measurement of highly filled polycarbonate melts using a slit-die rheometer, Korea-Aust. Rheol. J., **25**, 129-135, (2013)
44. Moravec J., Jirout T., Rieger F., Krátký L., Mixing system for highly concentrated fine-grained suspensions, Pol. J. Chem. Technol., **11**, 52-56, (2009).
45. Morrinson A. F., Understanding rheology, Oxford University Press, New York (2001)
46. Mooney, M., Formulas for slip and fluidity., J. Rheol. **2**, 210-222 (1931)
47. Mory M., Fluid mechanics for chemical engineering, London, Wiley, (2011).
48. Mozaffari F. E., Upreti R. S., Using ultrasonic Doppler velocimetry and CFD modeling to investigate the mixing of non-Newtonian fluids possessing yield stress, Chem. Eng. Res. Des., **87,** 515-523, (2009).
49. Muzychka Y.S, Edge J., Laminar Non-Newtonian Fluid Flow in Noncircular Ducts and Microchannels, J Fluids Eng, **30**, 1-7 (2008).
50. Nassehi Vahid, Practical aspects of finite element modeling of polymer processing, England, John Wiley, (2002)
51. Nguyen Q.D. and Boger D.V, Measuring the flow properties of yield stress fluids, Annu. Rev. Fluid Mech., **24**, 47-88, (1992)
52. Netusil J., F. Rieger, Power consumption of screw and helical ribbon agitators in highly viscous pseudoplastic fluids, Chem. Eng. J., **52**, 9-12, (1992)

53. Iranshahi A., Devals C., Heniche M., Fradette L., Tanguy P. A., Takenaka K., Hydrodynamics characterization of the Maxblend impeller, Chem. Eng. Sci. **62**, 3641-3653, (2007)
54. Osswald T., Rudolph N., Polymer rheology, Munich, Hanser Publication, (2015)
55. Padmanabhan M. and Bhattacharya M., In-line measurements of rheological properties of polymer melts, Rheol Acta, **33**, 71-87, (1984)
56. Paul E.L., Atiemo-Obeng V.A., Kresta S.M., Handbook of industrial mixing: Science and application, 1st edition, John Wiley & Sons, Inc, Canada, (2004).
57. Peker S. and Helvaci S., Solid-liquid two-phase flow, 1st edition, Elsevier, Netherland, (2008).
58. Rieger F., Determination of rheological parameters from measurements on a viscometer with coaxial cylinders, Acta Polytechnica, **46**, 42-51, (2006)
59. Rieger F., Novak V. Power consumption of agitators in highly viscous non-Newtonian fluids, Trans. Inst. Chem. Eng. 51, 105-111 (1973).
60. Rieger F., Novak V., Power consumption scale-up in agitating non-Newtonian fluids, Chem. Eng. Sci. **29**, 2229-2234, (1974).
61. Schramm G., A practical approach to rheology and rheometry 2nd edition, Gebrueder Haake GmbH, Germany (1998).
62. Senouci A., Smith A.C., An experimental study of food melt rheology, Rheol Acta, **27**, 546-554, (1988)
63. Skočilas J, R. Žitny R, Štancl R., Flow of bovine collagen in rectangular slit, AIP conference proceedings, **1843, (**2017)
64. Skočilas J, R. Žitny R, Štancl R, M. Dostal, J. Rheological Properties of Collagen Matter Predicted Using an Extrusion Rheometer, Texture stud. 47, 514-522 (2016).
65. Solomon J., Elson T.P., Nienow A. W., and Pace G. W., Cavern sizes in agitated fluid with a yield stress, Chem. Eng. Commun., 11, 143-164, (1981).
66. Son Y., Determination of shear viscosity and shear rate from pressure drop and flow rate relationship in a rectangular channel, Polymer, **48**, 632-637, (2006).
67. Sonbati A. E., Thermoplastic Elastomers, 1st edition, InTech, China, (2012).
68. Steffe J. F., Rheological methods in food engineering 2nd edition, Freeman Press, US, (1996).
69. Syrjala S., Aho J., Capillary rheometry of polymer melts – Simulation and experiment, Korea-Aust. Rheol. J, **24**, 241-247, (2012).
70. Šesták J., Žitný R. and Bukovský J. A comparison of methods for rapid calculation of frictional pressure drop and heat transfer coefficient for flow of non-Newtonian fluids in ducts with non-

circular cross-sections. Proceedings of the International Conference on Compact Heat Exchangers and Enhancement Technology for the Process Industries. (pp. 1-7). Banff, Canada, (1999, July).

71. Šesták J., Flow of Non-Newtonian Fluids in Open Circular Channels Can. J. Chem. Eng., 52 670-672. (1974)
72. Šesták, J., Žitný, R., Ondrušová, J., Filip, V., Axial Flow of Purely Viscous Fluids in Eccentric Annuli. Proceedings of 3rd Pacific Rim Conference on Rheology. Canadian Group of Rheology. (pp. 1-7). Montreal, Canada, (2001).
73. Šesták, J, Rieger F., Prenos Hybnosti, Tepla a Hmoty, Vydavatelstvi CVUT Praha (2005).
74. Thakur R.V., Vial, Ch., Djelveh G., Labbafi M, Mixing of complex fluids with flat-bladed impellers: effect of impeller geometry and highly shear-thinning behavior, Chem. Eng. Process, 43, 1211-1222, (2004).
75. Trivenia B., Vishwanadhama B., Madhavi T., Venkateshwar S., Mixing studies of non-Newtonian fluids in an anchor agitated vessel, Chem. Eng. Res. Des., **88**, 809-818, (2010).
76. Unadkat H., Rielly C. D., Nagy K., PIV study of the flow field generated by a sawtooth impeller, Chem. Eng. Sci, **66**, 5374-5387, (2011).
77. Utomo A. T (2009), Flow patterns and energy dissipation rates in batch rotor-stator mixers (Doctoral dissertation), The School of Engineering of The University of Birmingham, U.K.
78. Vial C., Stiriba Y., Trad Z., CFD Simulation of Flow and Mixing in In-line Rotor-Stator Mixers with Complex Fluids, Can J. Chem Eng. **93**, 391-403, (2015).
79. Vicente D., J, Rheology, InTech., Crotia, (2012)
80. White F., M., Fluid Mechanics, 4th Edition, McGrawHill, New York, 1999.
81. Wilkens R., Henry C., Gates L. E., How to scale-up mixing process in non-Newtonian fluids. Chem Eng. Prog., **5**, 44–52, (2003).
82. Zhang C. Gu J., Qin H., Xu Q. Li W., Jia X., Zhang J., CFD analysis of flow pattern and power consumption for viscous fluids in in-line highs hear mixers, Chem. Eng. Res. Des., **117**, 190-214, (2017).
83. Zhao X., Drop breakup in dilute Newtonian emulsions in simple shear flow: New drop breakup mechanisms, J. Rheol., **51**, 367-392, (2007)

List of Author's Publications

1. Ayas M. Skocilas J. and Jirout T., A practical method for predicting the friction factor of power-law fluids in a rectangular duct. Chem. Eng. Commun., **206**, 1310-1316, (2019), ISSN: 0098-6445.
2. Ayas M. Skocilas J. and Jirout T., Mixing of a viscoplastic fluid in an in-line mixer, in 8th Conference of Novel Trends in Rheology, Zlin-Czech Republic, 2019. AIP Conference Proceedings, **2107**,1-9, (2019), ISSN: 0094243X.
3. Skocilas J., Ayas M. Skocilasova B., Jirout T., Effect of rotation direction of helical-ribbon agitator on circulation of high viscous batch, in XVII International Scientific Conference: Dynamics of Rigid and Deformable Bodies, Usti nad Labem-Czech Republic, AIP conference proceedings, **2198**,1-5, (2019), ISSN: 0094243X.
4. Ayas M., Skocilas J., and Jirout T., Friction factor of shear thinning fluids in non-circular ducts – a simplified approach for rapid engineering calculation, Chem. Eng. Commun. 206, 1209-1217, 2021, ISSN: 0098-6445.
5. Ayas M., Skocilas J. and Jirout T., Analysis of Power Input of an In-Line Rotor-Stator Mixer for Viscoplastic Fluids, Processes, **8**, 1-15, (2020), ISSN: 2227-9717.
6. Ayas M., Skocilas J. and Jirout T., A method for the determination of shear viscosity of power-law fluids in a rectangular duct and concentric annulus, Asia-Pac. J. Chem. Eng. (Submitted), ISSN:1932-2143.

List of Figures

List of Tables

Appendix A- Constitutive Equations

1- Continuity Equation

The general expression of the continuity equation is

$$\frac{\partial \rho}{\partial t} + \nabla.(\rho \vec{u}) = 0$$

For steady-incompressible fluid flow

$$\nabla.\vec{u} = 0$$

I- Steady-incompressible fluid flow in cartesian coordinate

$$\frac{\partial u_x}{\partial x} + \frac{\partial u_y}{\partial y} + \frac{\partial u_z}{\partial z} = 0$$

II- Steady-incompressible fluid flow in cylindrical coordinates

$$\frac{1}{r}\frac{\partial}{\partial r}(ru_r) + \frac{1}{r}\frac{\partial(u_\theta)}{\partial \theta} + \frac{\partial(u_z)}{\partial z} = 0$$

III- Steady-incompressible fluid flow in spherical coordinates

$$\frac{1}{r}\frac{\partial}{\partial r}(r^2 u_r) + \frac{1}{r\sin\theta}\frac{\partial(u_\theta \sin\theta)}{\partial \theta} + \frac{1}{r\sin\theta}\frac{\partial(u_\varphi)}{\partial \varphi} = 0$$

2- Cauchy's Equations

The general expression

$$\rho\left(\frac{\partial \vec{u}}{\partial t} + \vec{u}.\nabla\vec{u}\right) = -\nabla p + \nabla.\vec{\vec{\tau}} + \rho\vec{g}$$

I- Cartesian coordinates (x, y, z directions)

$$\rho\left(\frac{\partial(u_x)}{\partial t} + u_x\frac{\partial(u_x)}{\partial x} + u_y\frac{\partial(u_x)}{\partial y} + u_z\frac{\partial(u_x)}{\partial z}\right) = -\frac{\partial p}{\partial x} + \frac{\partial(\tau_{xx})}{\partial x} + \frac{\partial(\tau_{yx})}{\partial y} + \frac{\partial(\tau_{zx})}{\partial z} + \rho g_x$$

$$\rho\left(\frac{\partial(u_y)}{\partial t} + u_x\frac{\partial(u_y)}{\partial x} + u_y\frac{\partial(u_y)}{\partial y} + u_z\frac{\partial(u_y)}{\partial z}\right) = -\frac{\partial p}{\partial y} + \frac{\partial(\tau_{yx})}{\partial x} + \frac{\partial(\tau_{yy})}{\partial y} + \frac{\partial(\tau_{yz})}{\partial z} + \rho g_y$$

$$\rho\left(\frac{\partial(u_z)}{\partial t}+u_x\frac{\partial(u_z)}{\partial x}+u_y\frac{\partial(u_z)}{\partial y}+u_z\frac{\partial(u_z)}{\partial z}\right)=-\frac{\partial p}{\partial z}+\frac{\partial(\tau_{zx})}{\partial x}+\frac{\partial(\tau_{zy})}{\partial y}+\frac{\partial(\tau_{zz})}{\partial z}+\rho g_z$$

II- Cylindrical coordinates (r, θ, z directions)

$$\rho\left(\frac{\partial(u_r)}{\partial t}+u_r\frac{\partial(u_r)}{\partial r}+\frac{u_\theta}{r}\frac{\partial(u_r)}{\partial\theta}+u_z\frac{\partial(u_r)}{\partial z}-\frac{{u_\theta}^2}{r}\right)=-\frac{\partial p}{\partial r}+\frac{1}{r}\frac{\partial(r\tau_{rr})}{\partial r}+\frac{1}{r}\frac{\partial(\tau_{\theta r})}{\partial\theta}+\frac{\partial(\tau_{zz})}{\partial z}-\frac{\tau_{\theta\theta}}{r}+\rho g_r$$

$$\rho\left(\frac{\partial(u_\theta)}{\partial t}+u_r\frac{\partial(u_\theta)}{\partial r}+\frac{u_\theta}{r}\frac{\partial(u_\theta)}{\partial\theta}+u_z\frac{\partial(u_\theta)}{\partial z}-\frac{u_\theta u_r}{r}\right)=-\frac{\partial p}{r\,\partial r}+\frac{1}{r^2}\frac{\partial(r^2\tau_{\theta r})}{\partial r}+\frac{1}{r}\frac{\partial(\tau_{\theta\theta})}{\partial\theta}+\frac{\partial(\tau_{zz})}{\partial z}-\frac{\tau_{\theta\theta}}{r}+\rho g_r$$

$$\rho\left(\frac{\partial(u_z)}{\partial t}+u_r\frac{\partial(u_z)}{\partial r}+\frac{u_\theta}{r}\frac{\partial(u_z)}{\partial\theta}+u_z\frac{\partial(u_z)}{\partial z}\right)=-\frac{\partial p}{\partial z}+\frac{1}{r}\frac{\partial(r\tau_{rz})}{\partial r}+\frac{1}{r}\frac{\partial(\tau_{\theta z})}{\partial\theta}+\frac{\partial(\tau_{zz})}{\partial z}+\rho g_z$$

III- Spherical coordinates (r, ∅, θ directions)

$$\rho\left(\frac{\partial(u_r)}{\partial t}+u_r\frac{\partial(u_r)}{\partial r}+\frac{u_\phi}{r}\frac{\partial(u_r)}{\partial\phi}+\frac{u_\theta}{r\sin\phi}\frac{\partial(u_r)}{\partial\theta}-\frac{{u_\phi}^2+{u_\theta}^2}{r}\right)=-\frac{\partial p}{\partial r}+\frac{1}{r^2}\frac{\partial(r^2\tau_{rr})}{\partial r}+\frac{1}{r\sin\theta}\frac{\partial\tau_{r\theta}}{\partial\theta}-\frac{\tau_{\phi\phi}+\tau_{r\theta}}{r}+\rho g_r$$

$$\rho\left(\frac{\partial(u_\phi)}{\partial t}+u_r\frac{\partial(u_\phi)}{\partial r}+\frac{u_\phi}{r}\frac{\partial(u_\phi)}{\partial\phi}+\frac{u_\theta}{r\sin\phi}\frac{\partial(u_\phi)}{\partial\theta}+\frac{u_r u_\phi}{r}-\frac{{u_\theta}^2\cot g\phi}{r}\right)$$
$$=-\frac{\partial p}{r\,\partial\phi}+\frac{1}{r^2}\frac{\partial(r^2\tau_{r\phi})}{\partial r}+\frac{1}{r\sin\phi}\frac{\partial\tau_{\phi\theta}}{\partial\theta}-\frac{\tau_{r\phi}}{r}-\frac{\cot g\phi\,\tau_{\phi\phi}}{r}+\rho g_\phi$$

$$\frac{\partial(u_\theta)}{\partial t}+u_r\frac{u_\theta}{r}+\frac{u_\phi}{r}\frac{\partial(u_\theta)}{\partial\phi}+\frac{u_\theta}{r\sin\phi}\frac{\partial(u_\theta)}{\partial\theta}+\frac{u_r u_\theta}{r}+\frac{u_\phi u_\theta\cot g\phi}{r}$$
$$=-\frac{\partial p}{r\sin\phi\,\partial\phi}+\frac{1}{r^2}\frac{\partial(r^2\tau_{r\theta})}{\partial r}+\frac{1}{r}\frac{\partial\tau_{\phi\theta}}{\partial\phi}+\frac{1}{r\sin\phi}\frac{\partial\tau_{\theta\theta}}{\partial\theta}+\frac{\tau_{r\theta}}{r}+\frac{2\cot g\phi\,\tau_{\phi\theta}}{r}+\rho g_\theta$$

C- Rate of deformation tensor

The general expression of the rate of deformation tensor

$$\Delta_{ij}=\frac{1}{2}\left(\frac{\partial u_i}{\partial x_j}+\frac{\partial u_j}{\partial x_i}\right)$$

I- Cartesian coordinates (x, y, z directions)

$$\Delta_{xx}=\frac{\partial u_x}{\partial x} \qquad \Delta_{yy}=\frac{\partial u_y}{\partial y} \qquad \Delta_{zz}=\frac{\partial u_z}{\partial z}$$

$$\Delta_{xy}=\Delta_{yx}=\frac{1}{2}\left(\frac{\partial u_x}{\partial y}+\frac{\partial u_y}{\partial x}\right) \qquad \Delta_{xz}=\Delta_{zx}=\frac{1}{2}\left(\frac{\partial u_x}{\partial z}+\frac{\partial u_z}{\partial x}\right) \qquad \Delta_{yz}=\Delta_{zy}=\frac{1}{2}\left(\frac{\partial u_z}{\partial y}+\frac{\partial u_y}{\partial z}\right)$$

II- Cylindrical coordinates (r, θ, z directions)

$$\Delta_{rr}=\frac{\partial u_r}{\partial r} \qquad \Delta_{\theta\theta}=\frac{1}{r}\frac{\partial u_\theta}{\partial \theta}+\frac{u_r}{r} \qquad \Delta_{zz}=\frac{\partial u_z}{\partial z}$$

$$\Delta_{rz}=\Delta_{zr}=\frac{1}{2}\left(\frac{\partial u_r}{\partial z}+\frac{\partial u_z}{\partial r}\right) \qquad \Delta_{\theta z}=\Delta_{z\theta}=\frac{1}{2}\left(\frac{\partial u_\theta}{\partial z}+\frac{1}{r}\frac{\partial u_z}{\partial \theta}\right)$$

$$\Delta_{r\theta}=\Delta_{\theta r}=\frac{1}{2}\left(r\frac{\partial}{\partial r}\left(\frac{u_\theta}{r}\right)+\frac{1}{r}\frac{\partial u_r}{\partial \theta}\right)$$

III- Spherical coordinates (r, ∅, θ directions)

$$\Delta_{rr}=\frac{\partial u_r}{\partial r} \qquad \Delta_{\theta\theta}=\frac{1}{r}\frac{\partial u_\theta}{\partial \theta}+\frac{u_r}{r} \qquad \Delta_{\varphi\varphi}=\frac{1}{r\sin\theta}\frac{\partial u_\emptyset}{\partial \emptyset}+\frac{u_r}{r}+\frac{u_\theta \cot\theta}{r}$$

$$\Delta_{r\theta}=\Delta_{\theta r}=\frac{1}{2}\left(r\frac{\partial}{\partial r}\left(\frac{u_\theta}{r}\right)+\frac{1}{r}\frac{\partial u_r}{\partial \theta}\right) \qquad \Delta_{\emptyset r}=\Delta_{r\emptyset}=\frac{1}{2}\left(\frac{1}{r\sin\theta}\frac{\partial u_r}{\partial \emptyset}+r\frac{\partial}{\partial r}\left(\frac{u_\varphi}{r}\right)\right.$$

$$\Delta_{\emptyset\theta}=\Delta_{\theta\emptyset}=\frac{1}{2}\left(\frac{\sin\theta}{r}\frac{\partial}{\partial \emptyset}\left(\frac{u_\emptyset}{\sin\theta}\right)+\frac{1}{r\sin\theta}\frac{\partial u_\theta}{\partial \emptyset}\right)$$

Appendix B- Grid Convergence Index

1- Eccentric annulus

```
N = [ 40000 120000 292000 ];
Phi = [ 0.0216, 0.0223, 0.024];

plot(N,Phi);

[N, i] = sort(N,'descend');
Phi = Phi(i);

D=3;
r21 = (N(1)/N(2))^(1/D)
r32 = (N(2)/N(3))^(1/D)
if ( r21 < 1.3 || r32 < 1.3 )
  disp('refinement factors r21 and r32 should be greater than 1.3');
end

eps32 = Phi(3)-Phi(2)
eps21 = Phi(2)-Phi(1)
R = eps21/eps32
s = sign(eps32/eps21)

fq = @(p) log((r21.^p-s)./(r32.^p-s));
fp = @(p) p - 1/log(r21)*abs(log(abs(eps32/eps21))+fq(p));
p = fsolve(fp,1)

Phi21ext = (r21^p*Phi(1)-Phi(2))/(r21^p-1)
GCI33 = 1.25*abs(Phi21ext-Phi(3))/Phi(3)*100

e32a = abs((Phi(2)-Phi(3))/Phi(2))*100
GCI32 = 1.25*e32a/(r32^p-1)

e21a = abs((Phi(1)-Phi(2))/Phi(1))*100
e21ext = abs((Phi21ext-Phi(1))/Phi21ext)*100
GCI21 = 1.25*e21a/(r21^p-1)
```

Results

P=4.755
GCI32=2.94
GCI21=0.7761

2- In-line mixer

```
N = [ 1100000 2600000 11000000 ];
Phi = [ 4.78 4.925 5 ];

[N, i] = sort(N,'descend');
Phi = Phi(i);

figure(1);
plot(N,Phi,'r*', N,Phi,'b');
grid on;

D = 3;

r21 = (N(1)/N(2))^(1/D)
r32 = (N(2)/N(3))^(1/D)
if ( r21 < 1.3 || r32 < 1.3 )
  disp('refinement factors r21 and r32 should be greater than 1.3');
end

eps32 = Phi(3)-Phi(2)
eps21 = Phi(2)-Phi(1)
R = eps21/eps32
s = sign(eps32/eps21)

fq = @(p) log((r21.^p-s)./(r32.^p-s));
fp = @(p) p - 1/log(r21)*abs(log(abs(eps32/eps21))+fq(p));

p = fsolve(fp,1)

Phi21ext = (r21^p*Phi(1)-Phi(2))/(r21^p-1)
e21a = abs((Phi(1)-Phi(2))/Phi(1))*100
GCI21 = 1.25*e21a/(r21^p-1)

e32a = abs((Phi(2)-Phi(3))/Phi(2))*100
GCI32 = 1.25*e32a/(r32^p-1)

GCI33 = 1.25*abs(Phi21ext-Phi(3))/Phi(3)*100
```

Appendix C- MATLAB codes for velocity and shear rate processing

```
clear all;
load velnode.txt
x=velnode(:,2);
y=velnode(:,3);
r=sqrt(x.^2+y.^2);
v=velnode(:,5);
rmax=0.097;
rmin=0.000;
dr=0.001;
n=(rmax-rmin)/dr;
rxn=length(r);
for i=1:n+1;
    rd=(i-1)*dr;
    rup=rd+0.003;
    sum=0;
    div=0;
    rm(i)=(rd+rup)/2;
    for j=1:rxn
        if r(j)<rup && r(j)>rd;
            sum = sum + v(j);
            div=div+1;
        end
    end
    vm(i)=sum/max(1,div);

end

 plot(rm,(vm));
```

Appendix-D Shear rate profiles

c_a=2 mm, 500 RPM, A1

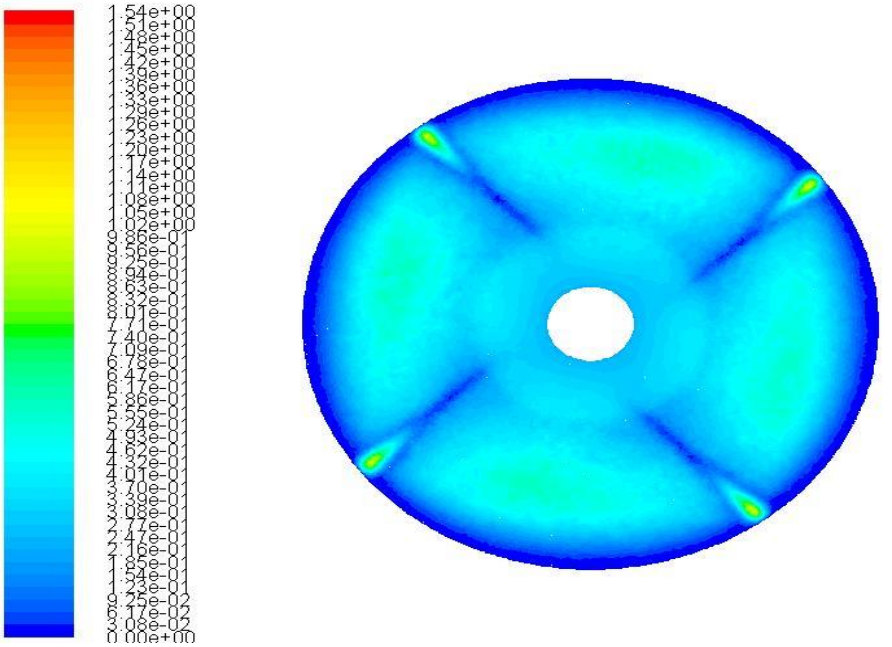

c_a=2 mm, 500 RPM A3

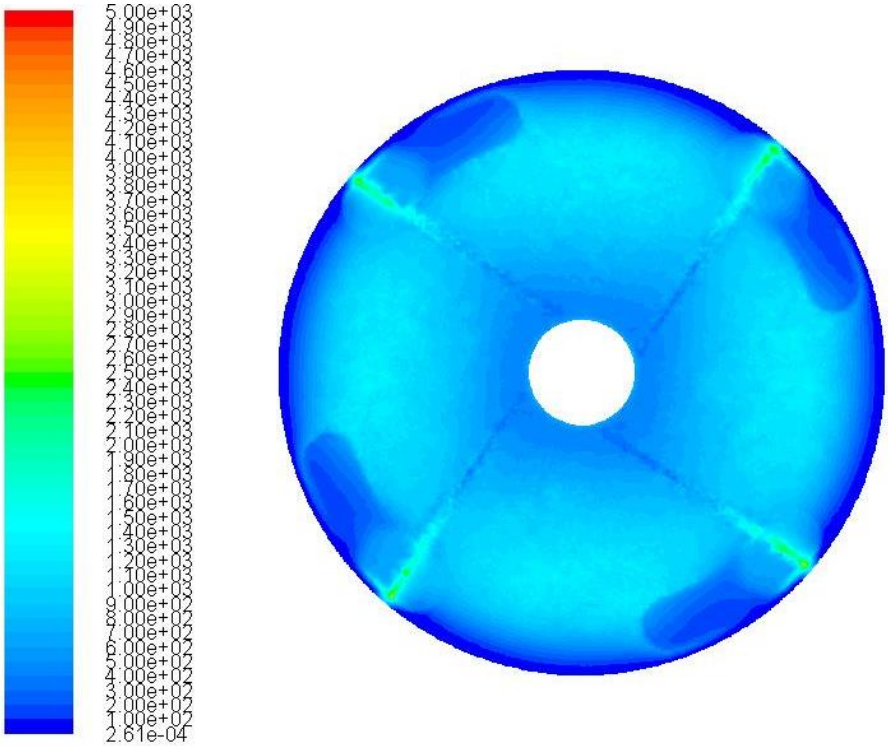

c_a=1 mm, 500 RPM, A1

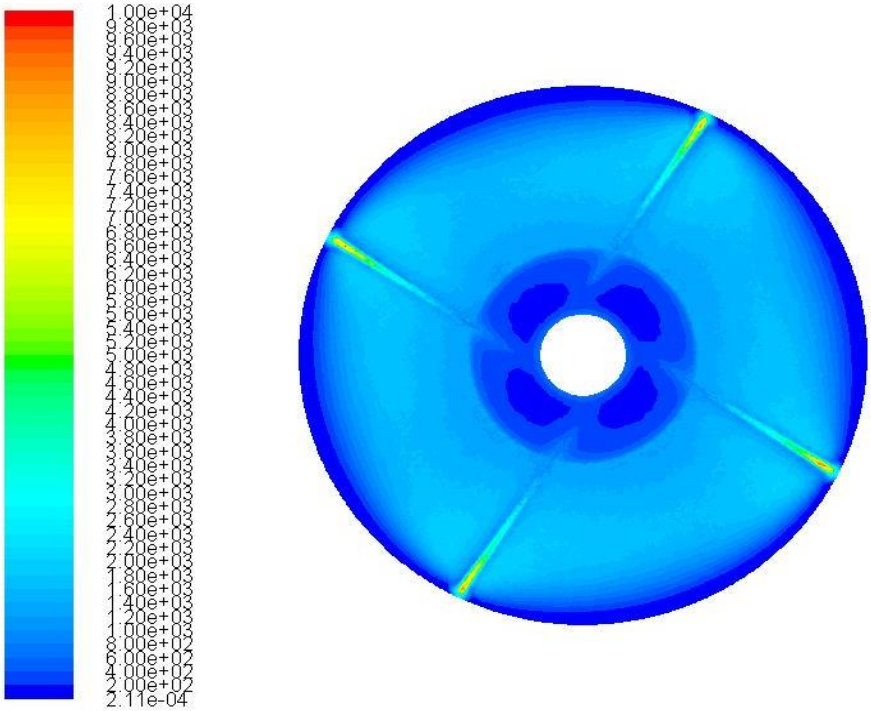

c_a=1 mm, 500 RPM, A3

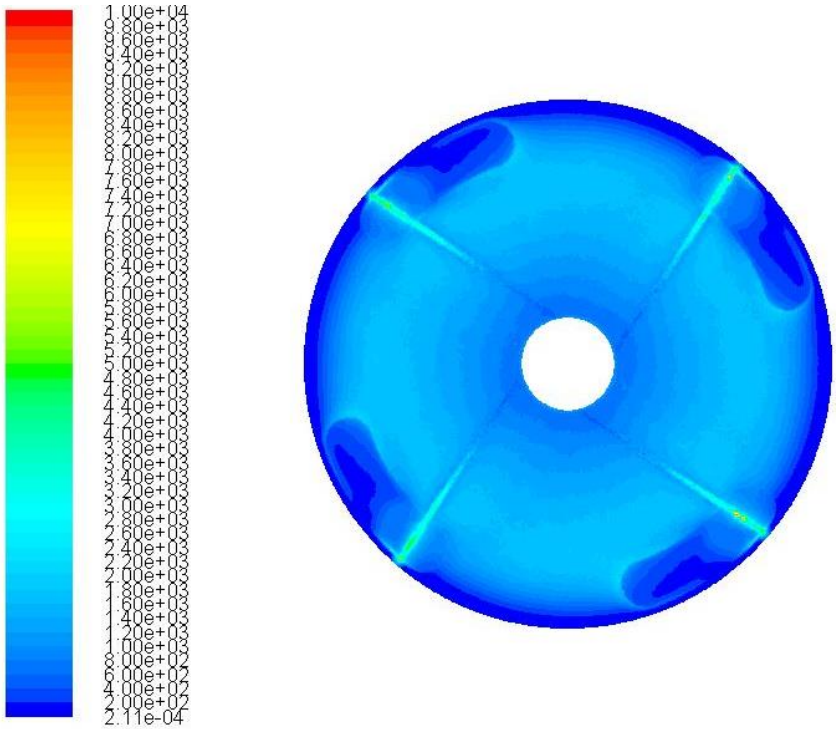

c_a=1 mm, 150 RPM, A1

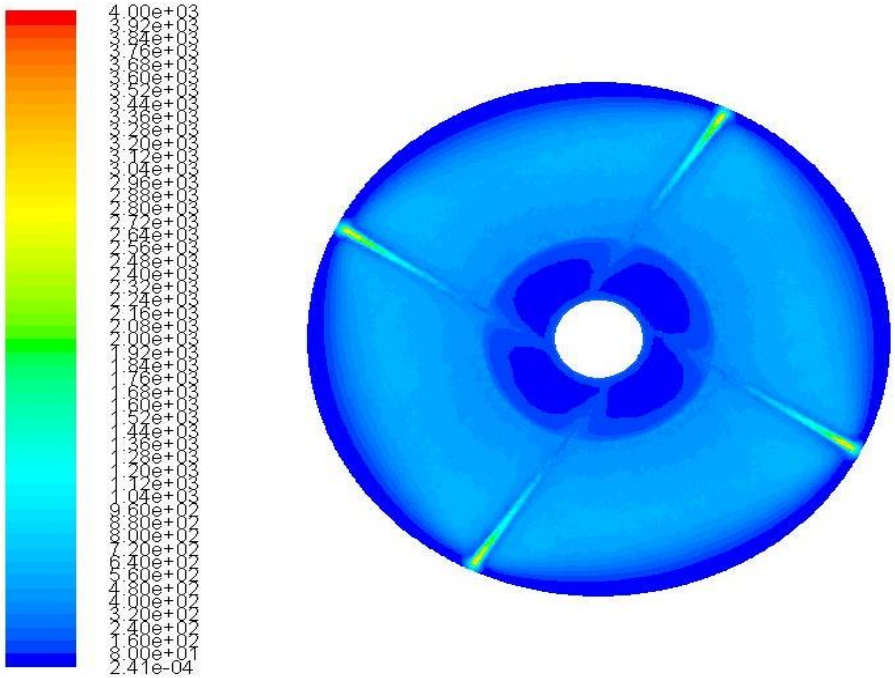

c_a=1 mm, 150 RPM, A3

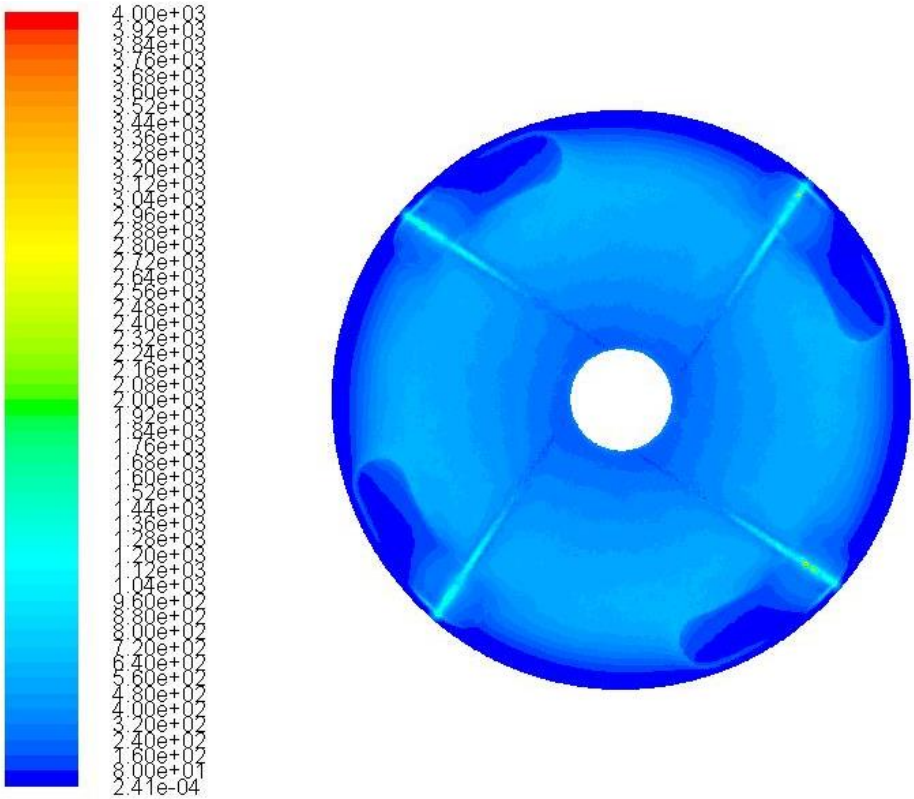

C-C

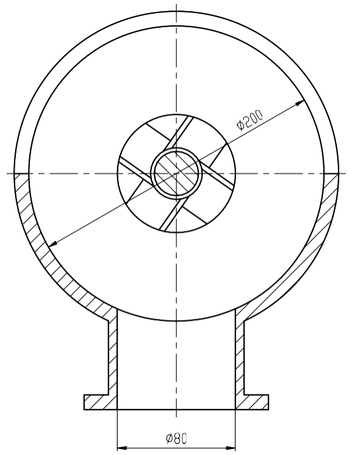

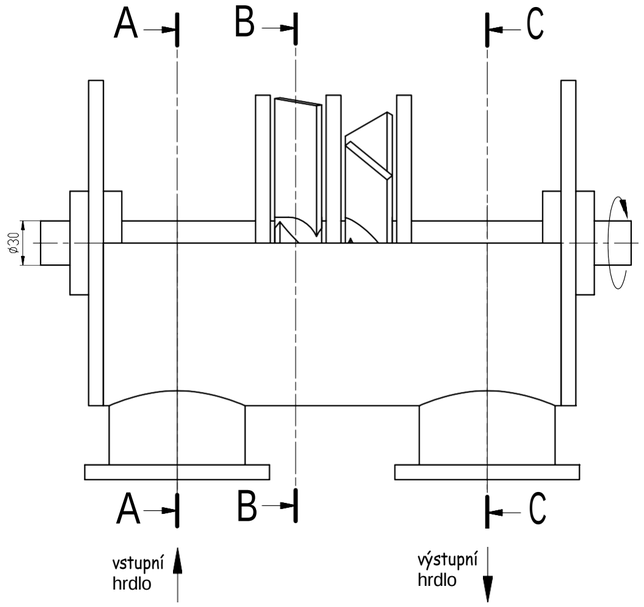

A-A

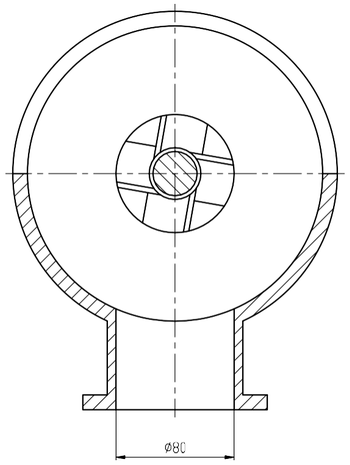

B-B

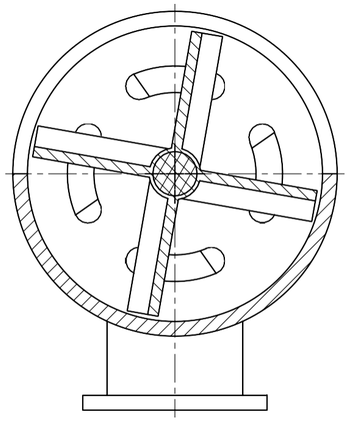

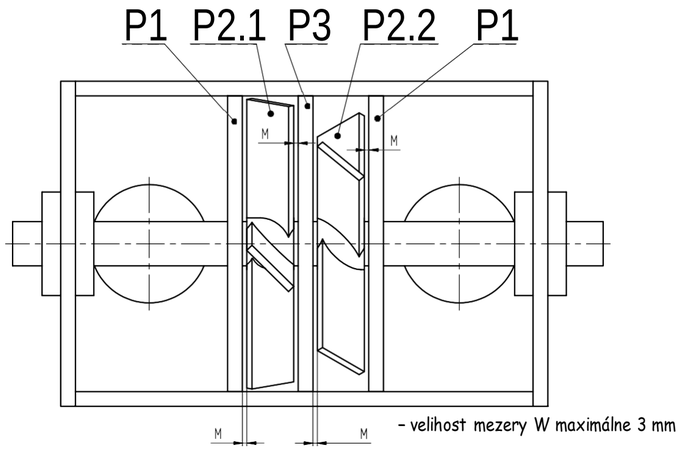

- velihost mezery W maximálne 3 mm

Detail P1

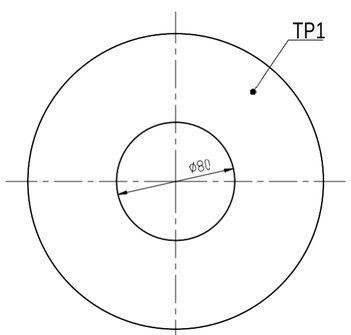

- vymenitelnost dishu
- rnzné tlouštky dishu TPU v závislosti na dosažení požadované velihosti mezery W (W < 3 mm(
- pii zmene geometrie dishu nutnost ZAEHOVÁNÍ ahtuálního PRNTOENÉHO prniezu (Ø00/Ø30(

Detail P2

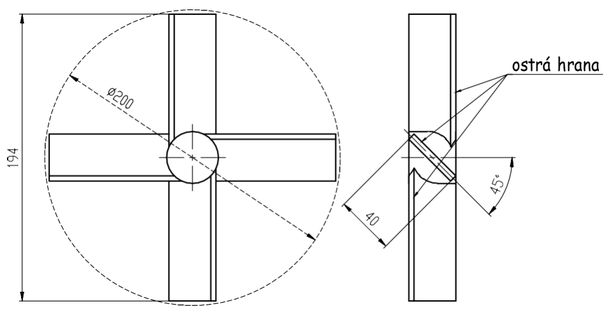

- minimálne možný prnmer náboje
- ZAEHOVAT ostré hrany MÍEHADEL ve smeru tohu materiálu
- HOTOUEE P2.U a P2.2 vzájemne POOTOEENY o LG°

Detail P3

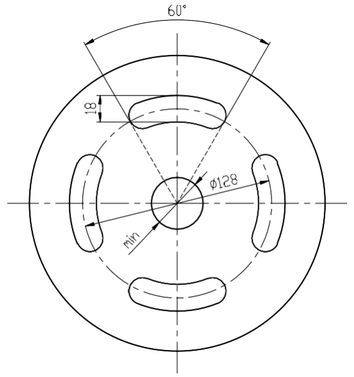

- vymenitelnost dishu
- PRNTOENÁ PLOEHA drážhami = PRNTOENÝ prniez Ø00/Ø30,

pii jahéholiv GEOMETRIEHÉ MODIFIHAEI drážeh nutnost jejího ZAEHOVÁNÍ

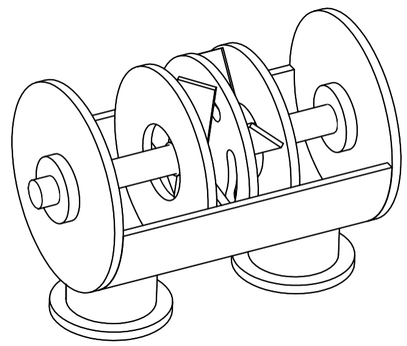

POŽADAVVY NA IE°PADLO
- minimální prntoh suroviny 70 hg/h, optimální dosáhnout prntohu provozního
- tlahová spád jednothy 0,G WPa (stanovena piibližným VÝPOETEM(

	Podpis	Datum		Podpis	Datum		MĚŘÍTKO
NAVRHL			STATIK			HMOTNOST kg	1:2
KRESLIL	Krotký, Morovec	09.09.2014	NORM. REF.			MIKROFILM	Č. SVITKU
SKUPINA6			PŘEZK.			SESTAVA	KUSOVNÍK
TECHNOL.			SCHVÁLIL			STARÝ V.	

ČESKÉ VYSOKÉ UČENÍ TECHNICKÉ V PRAZE

FAKULIA STROJNÍ

NÁZEV: MÍSIČ 1H1S

TYP:

ČÍSLO VÝKRESU: LK30-01.C001

LIST: A1